POLITECNICO DI MILANO

Sede di Milano Leonardo
Scuola di Ingegneria Industriale e dell'Informazione
Corso di Laurea Magistrale in Ingegneria Nucleare

High temperature investigation of nanostructured actinide oxides

Relatore: Prof. Lelio Luzzi

Co-relatore: Dott. Dario Manara

Tesi di Laurea di:

Fabiola Cappia   Matr. 765363

Anno Accademico: 2012/2013

"It's better to ask some of the questions
than to know all the answers."

J. Thurber

Contents

List of Figures

List of Tables

Acronyms

BSE	Back-Scattered Electrons
CCD	Charge Coupled Device
DC	Direct Current
DNA	DesoxyriboNucleic Acid
DNB	Departure from Nucleate Boiling
DSC	Differential Scanning Calorimetry
ED	Electron Diffraction
EDX	Energy Dispersive X-ray spectroscopy
fcc	Face Centred Cubic crystal
FFT	Fast Fourier Transform
FWHM	Full Width at Half Maximum
GWd/tM	Giga-Watt-day per ton of heavy metal
HAADF	High Angle Annular Dark Field
HBS	High Burn-up Structure
HRTEM	High Resolution Transmission Electron Microscopy
IAEA	International Atomic Energy Agency
ISO	International Organisation for Standardisation
ITU	Institute for Transuranium Elements
LMFBR	Liquid Metal Fast Breeder Reactor
LO	Longitudinal Optical mode
LSN	Liquid Skin Nucleation model
MD	Molecular Dynamics simulations
Ncs	Nanocrystals
Nc-ThO$_2$	Nanocrystalline ThO$_2$
Nc-UO$_2$	Nanocrystalline UO$_2$
NIST	National Institute of Standard and Technology
NSE	Normal Spectral Emittance
O/M	Ratio between oxygen and metal atomic concentration
OIML	Organisation Internationale de Métrologie Légale
PC	Personal Computer
PCM	Phonon Confinement Model
PTB	Physikalisch-Technische Bundesanstalt

RLS	Reflected Laser Signal
SE	Secondary Electrons
SEM	Scanning Electron Microscopy
STEM	Scanning Transmission Electron Microscopy
TEM	Transmission Electron Microscopy
TG	Thermo-Gravimetry
TO	Transversal Optical mode
TT	Thermal Treatment

Abstract

Other studies have shown that the zone of UO_2 nuclear fuel recrystallised under high irradiation in the nanometer-size range (high burn-up structure) has better fission gas retention and mechanical properties than the less irradiated fuel. This suggests that some synthetic actinide nanomaterials could be used as advanced nuclear fuels to reproduce these benefits. However, nanomaterials can show worse thermophysical properties crucial for the fuel safety, such as a lower melting temperature (T_m). The grain size dependence of T_m defines the performance limits of such potential advanced fuels. The present work is mainly focused on the investigation of possible melting point depression of nanocrystalline (nc) UO_2 and ThO_2, studying their behaviour above 1500 K for the first time.

The technique used is based on sub-second laser heating and fast pyrometry. The apparatus included a probe laser. The changes in its reflected signal induced by vibrations of the molten surface have been used to detect the melting onset. Other material characterization techniques have also been applied. In particular, Raman Spectroscopy permitted a first non-destructive analysis of the local grain size evolution with temperature for nc-ThO_2.

Nc-UO_2 with grains of (30 ± 20) nm underwent fast oxidation due to the high specific surface. The measured melting point depression (up to over 300 K below 3120 K, the T_m of micrometer sized UO_2) was thus due both to size effect and oxygen hyperstoichiometry. Chemically more stable ThO_2 was then studied in order to estimate the size effect only. Nc-ThO_2 with grains of 3-5 nm was firstly studied to quantify the maximum possible melting variation. Although it was not possible to determine the exact melting onset temperature, the presence of liquid was detected 400-600 K below the T_m of micrometer sized ThO_2 (3651 K). This experimental evidence is paramount in that it shows for the first time the occurrence of a large size effect on the melting point of this kind of refractory oxides.

Further experiments are ongoing to confirm these first original results.

Keywords: Laser heating technique, nanostructured UO_2 and ThO_2, melting point depression.

Sommario

Altri studi hanno dimostrato che la zona del combustibile nucleare UO_2 ricristallizzata con grani nanometrici sotto alto irraggiamento (*high burn-up structure*) ha migliori proprietà di ritenzione dei gas di fissione e meccaniche, rispetto al combustibile meno irraggiato. Composti sintetici di attinidi nanostrutturati potrebbero dunque essere impiegati come combustibili avanzati, riproducendo tali benefiche proprietà. Tuttavia, i nanomateriali possono manifestare peggiori proprietà termofisiche, come una inferiore temperatura di fusione. Essa è fondamentale per la sicurezza nei reattori, quindi la comprensione di una sua variazione in funzione della dimensione dei grani è cruciale per determinare pro e contro di tali potenziali combustibili. Questo lavoro è focalizzato sullo studio del possibile abbassamento della temperatura di fusione per UO_2 e ThO_2 nanocristallini (nc), studiati qui per la prima volta sopra i 1500 K usando un riscaldamento laser rapido e pirometria.

L'apparato include un laser sonda: le variazioni nel segnale riflesso indotte da vibrazioni della superficie liquida rivelano l'inizio della fusione. Sono state applicate anche altre tecniche di caratterizzazione. In particolare, la Spettroscopia Raman è stata usata come metodo non distruttivo per un'analisi locale dell'evoluzione termica della dimensione dei grani per nc-ThO_2.

Nc-UO_2 con grani di (30 ± 20) nm subisce una rapida ossidazione per l'elevata superficie specifica. L'abbassamento misurato (fino a 300 K sotto 3120 K, temperatura di fusione di UO_2 *bulk*) è dunque dovuto a effetti sia di dimensione sia di stechiometria. Per stimare il solo contributo dei primi, è stato studiato il ThO_2, chimicamente più stabile, analizzando nc-ThO_2 con grani di 3-5 nm, per quantificare il massimo abbassamento possibile. Benchè non sia stato possibile determinare l'inizio della fusione, la presenza di liquido è stata misurata a 400-600 K sotto la temperatura di fusione del ThO_2 *bulk* (3651 K). Questa è la prima evidenza sperimentale di un notevole effetto legato alla dimensione dei grani in questo tipo di ossidi refrattari.

Ulteriori esperimenti sono in corso per confermare questi primi originali risultati.

Parole chiave: Riscaldamento laser rapido, UO_2 e ThO_2 nanostrutturati, abbassamento della temperatura di fusione.

Estratto in italiano

Introduzione

Il presente lavoro è stato svolto in collaborazione tra Politecnico di Milano e Istituto degli Elementi Transuranici (ITU), Centro Comune di Ricerca della Commissione Europea sito in Karlsruhe (Germania), durante un periodo di tirocinio della durata di 10 mesi presso lo stesso Istituto degli Elementi Transuranici.

Questo progetto si colloca in una delle tematiche fondamentali del Settimo Programma Quadro per la Ricerca della Commissione Europea [1] riguardante la sicurezza dei reattori nucleari, e in particolare il comportamento di potenziali nuovi combustibili nucleari in condizioni estreme, nonché nella ricerca fondamentale e applicata sulle proprietà ad alte temperature degli attinidi e dei loro composti.

Lo studio di nuovi combustibili con migliori caratteristiche è di fondamentale importanza sia per favorire la sostenibilità della produzione di energia da fonti nucleari, sia per migliorare la sicurezza dei reattori, argomento ancor più al centro del dibattito internazionale dopo l'incidente di Fukushima.

L'interesse per combustibili nanostrutturati nasce dal fatto che recenti studi hanno dimostrato che la zona periferica del combustibile (inizialmente formata da grani di 10-20 μm), soggetta durante l'irraggiamento ad alto *burn-up* a una ricristallizzazione che porta alla formazione di grani di dimensione nanometrica, presenta migliori proprietà meccaniche e aumentata capacità di ritenzione dei gas di fissione [2, 3].

Tuttavia, è ben noto che per materiali nanostrutturati alcune proprietà termofisiche (quali la temperatura di fusione) peggiorino, mostrando una dipendenza dalla dimensione dei grani [4–6]. Ciò è dovuto all'aumento del rapporto superficie/volume: gli atomi superficiali hanno un minor numero di coordinazione e una minor energia di legame rispetto agli atomi nel volume del materiale, causando un aumento della instabilità della struttura [6].

Il presente studio è focalizzato sull'indagine di un possibile abbassamento della temperatura di fusione in ossidi di attinidi nanostrutturati. In particolare sono state studiate nanoparticelle di UO_2 e ThO_2.

La tecnica sperimentale impiegata in questa ricerca è il riscaldamento laser rapido con misurazione della temperatura attraverso pirometri con risoluzione del microsecondo. L'apparato comprende anche un laser a bassa potenza (1 W) il cui segnale viene riflesso dalla superficie del campione e rilevato dal pirometro. Il segnale riflesso (RLS) viene

usato per rivelare la formazione del liquido, in seguito alla quale le forze di capillarità fanno vibrare la superficie, causando variazioni nel segnale registrato. L'approccio è stato ampiamente usato per investigare le temperature di fusione di vari materiali nucleari e non [7–10] ed è qui applicato per la prima volta a materiali nucleari nanostrutturati. Finora il comportamento ad alta temperatura di materiali refrattari nanostrutturati non è stato studiato e in questo senso il presente lavoro è una prima indagine e caratterizzazione dei suddetti materiali.

Prima di passare alla descrizione dei materiali, delle tecniche sperimentali usate e dei risultati, viene riportata una breve digressione sulla termodinamica applicata a sistemi nanoscopici, come contesto teorico per la comprensione delle variazioni della temperatura di fusione nei nanomateriali.

Nanotermodinamica

Da un punto di vista puramente teorico, la termodinamica e la sua connessione alla fisica statistica risulta valida solo quando il numero di particelle considerate tende ad infinito. Ciò non è chiaramente valido nel caso di sistemi a dimensione finita, quali nanoparticelle, isolate o agglomerate [6].

Tuttavia, si può distinguere tra due tipi di sistemi termodinamici a dimensione finita: un singolo insieme nanoscopico, oppure un sistema contenente molti di questi insiemi di nanoparticelle. Nel primo caso, la termodinamica "classica" può perdere di validità e modelli specifici devono essere sviluppati per questo tipo di sistemi [6]. La trattazione di tali sistemi esula dallo scopo di questa tesi.

Nel secondo caso, invece, si possono ancora applicare le equazioni di base della termodinamica, tenendo conto della dimensione finita del sistema tramite opportune correzioni. Quando il sistema viene descritto attraverso il potenziale termodinamico G, ad esempio, termini energetici dovuti alla superficie o altri gradi di libertà (quali possibili interazioni con la matrice che circonda le nanoparticelle) devono essere aggiunti all'energia libera di Gibbs volumica $G_v(T)$, ottenendo un potenziale $G^*(T)$ generalizzato:

$$G^*(T) = G_v(T) + G_{superficie/interfaccia}(T) \tag{1}$$

dove $G_{superficie/interfaccia}(T)$ è l'energia libera superficiale o di interfaccia con la matrice.

Cosiderando la transizione solido-liquido, la temperatura di fusione è definita come la temperatura alla quale l'energia libera della fase solida ($G_s(T)$) è pari a quella della fase liqida ($G_l(T)$). Quando si considera un solido nanostrutturato, la sua energia libera $G^*(T)$ varia secondo (1), causando una variazione della temperatura di fusione[1]. A seconda del contributo del temine di superficie/interfaccia, hanno luogo un innalzamento

---

[1]Il liquido prodotto dalla fusione del solido nanostrutturato potrebbe avere proprietà diverse rispetto a quello prodotto dalla fusione del materiale *bulk*, dove il termine *bulk* indica, in questa trattazione, il materiale a grani non nanometrici. Tuttavia, nella presente trattazione si assume che il liquido prodotto dal solido nanostrutturato e dal solido *bulk* abbiano la stessa natura.

della temperatura di fusione o un suo abbassamento, come schematizzato in Fig. 1(a) e 1(b).

(a)   (b)
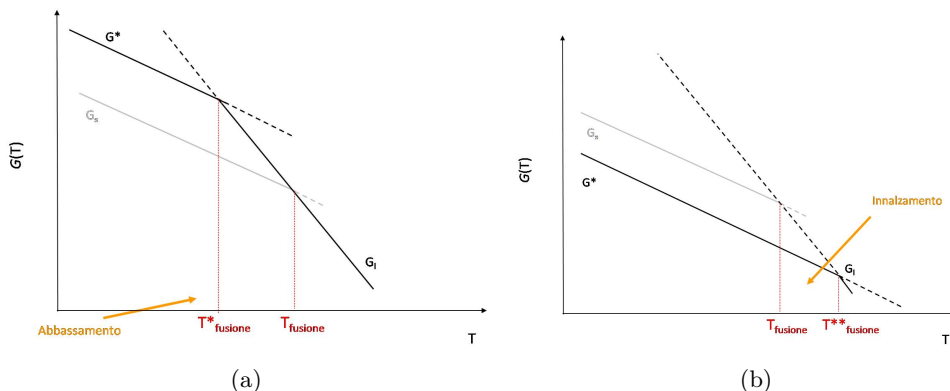
Figura 1: (a) Esempio di depressione della temperatura di fusione. (b) Esempio di aumento della temperatura di fusione. G_s**: energia libera della fase solida,** G_l**: energia libera della fase liquida,** G^***: energia libera del solido nanostrutturato.**

Nonostante la transizione solido-liquido nei nanomateriali sia un fenomeno ampiamente studiato e siano stati sviluppati molti modelli analitici fin dal 1800 [11], non esiste ancora una teoria comprensiva.

In generale, tutti i modelli determinano una relazione "universale" tra il cambiamento della temperatura di fusione (considerando particelle libere) e la dimensione dei grani,

$$\frac{T_m}{T_{m,\infty}} \propto 1 - \frac{\alpha}{D} \tag{2}$$

dove $\frac{T_m}{T_{m,\infty}}$ è il rapporto tra la temperatura di fusione delle nanoparticelle di diametro D e quella del materiale *bulk*, mentre α è una costante il cui valore e significato dipende dal modello analitico usato.

Materiali

La sintesi di composti nanostrutturati di attinidi è stata realizzata solo nell'ultimo decennio. In particolare, in ITU, nelle Unità "Nuclear Fuels" e "Nuclear Chemistry", NpO_2, UO_2 e ThO_2 nanocristallini sono stati sintetizzati seguendo due diversi approcci: una sintesi non-acquosa basata sulla tecnica denominata "heating-up" [12, 13] e una sintesi acquosa, basata sulla riduzione elettrochimica di $U(VI)$ a $U(IV)$ e la seguente precipitazione di particelle di diossido di uranio in condizioni riducenti a pH costante [14].

Nel caso dell'UO_2 possono essere prodotte quantità fino alla decina di grammi per sintesi. Dato che i campioni di nc-UO_2 si sono ossidati subito dopo il processo di sintesi [15], le particelle sono state trattate in ambiente riducente (Ar/H_2) a 900 K in modo da ridurre la non stechiometria. Ovviamente, il trattamento termico ha portato a una crescita dei grani, stimata in questo lavoro di (30 ± 20) nm. Successivamente, le

polveri sono state pressate a freddo, ottenendo sei pastiglie (Fig. 2) di peso compreso tra 300 mg e 425 mg.

Per il ThO_2, invece, le difficoltà del processo di sintesi sono molteplici e solo decine di mg possono essere ottenute per ogni sintesi. La polvere iniziale (Fig. 3(a)) è stata trattata termicamente per ridurre la quantità di materiale organico derivante dalla sintesi e poi pressata in una pressa idraulica ottenendo pastiglie di 3 mm di diametro e qualche frazione di mm di spessore (Fig. 3(b)) con peso variabile tra i 10 e i 23 mg. In questo caso la temperatura del trattamento termico è stata sufficientemente bassa da rendere la crescita dei grani minima, portando alla formazione di particelle approssimativamente sferiche di 3-5 nm. Ciò ha permesso un primo studio del potenziale abbassamento massimo della temperatura di fusione in questo tipo di materiale.

Figura 2: Pastiglie di UO_2 nanocristallino.

(a)   (b)
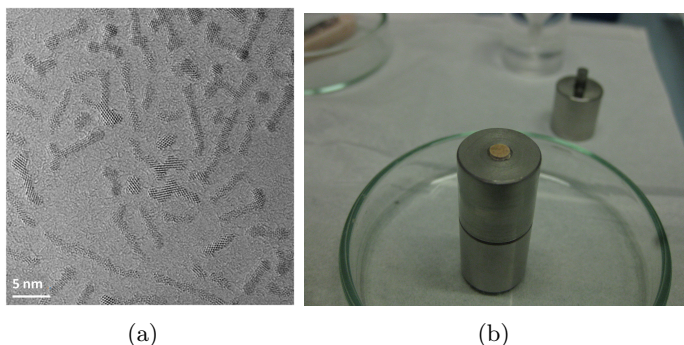
Figura 3: (a) Immagini HRTEM delle particelle cilindriche di ThO_2. (b) Esempio di pastiglia di ThO_2 nanocristallino.

Apparato sperimentale e di caratterizzazione dei materiali

Come detto nell'introduzione, la tecnica sperimentale consiste nel riscaldamento laser con misurazione della temperatura di radianza attraverso pirometri, la quale, corretta del valore dell'emittanza normale spettrale, fornisce la temperatura reale del campione. Il rapido riscaldamento e raggiungimento della fusione è fondamentale per limitare l'agglomerazione delle nanoparticelle e studiare quindi l'abbassamento della temperatura di fusione in funzione della dimensione dei grani.

Più nello specifico, per il riscaldamento dei campioni è stato adoperato un laser a stato solido Nd:YAG con lunghezza d'onda di 1064 nm e potenza massima di 4.5 kW. Per quanto riguarda la misurazione delle temperature di radianza, è stato calibrato e impiegato un pirometro a due lunghezze d'onda (655 nm e 488 nm). Per il calcolo dell'emittanza, invece, è stato usato uno spettro-pirometro con matrice di 256 fotodiodi con uno spettro di lunghezze d'onda da 480 a 1010 nm, precedentemente calibrato con un corpo nero riscaldato oltre 3000 K [16]. Elemento di fondamentale importanza è il laser a bassa potenza usato per determinare l'inizio della transizione solido-liquido, come anticipato nell'introduzione. Si tratta di un laser ad Ar^+ con lunghezza d'onda 488 nm e potenza massima 1 W, il cui segnale riflesso viene registrato dal secondo canale del pirometro.

Il campione viene posto in posizione verticale all'interno di una autoclave riempita in seguito con 2.5 bar di aria nel caso del ThO_2 per evitarne la riduzione e di Ar/H_2 nel caso dell'UO_2 per ridurne l'ossidazione. È stato possibile fissare i campioni di nc-UO_2 con viti di grafite, mentre per le pastiglie di nc-ThO_2 (assai più fragili) è stato costruito un supporto di ThO_2 "bulk" composto di semi dischi in cui sono stati praticati dei fori per adagiarvi il campione. In Fig. 4 è sintetizzato lo schema dell'apparato sperimentale appena descritto.
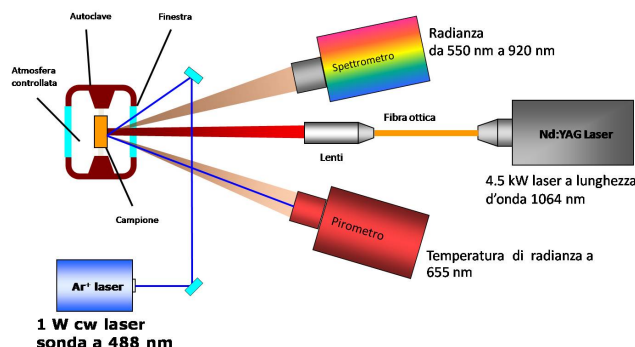
Figura 4: Schema della tecnica sperimentale.

Parte fondamentale dello studio è stata la caratterizzazione dei campioni nanostrutturati sia prima sia dopo la fusione. A tale scopo sono state impiegate diverse tecniche: Diffrazione dei Raggi X (XRD), Microscopia Elettronica a Scansione e Trasmissione (SEM e TEM), Termogravimetria (TG) e Spettroscopia Raman.

Risultati

Diossido di Uranio

Caratterizzazione prima degli esperimenti di fusione

Per prima cosa, sono state condotte le analisi con TEM e XRD. Le immagini TEM hanno rivelato che le particelle presentavano una dimensione media di 30 nm con una grande dispersione, stimata di ± 20 nm. In Fig. 5 è riportata una porzione del diffrattogramma

XRD: rispetto al materiale *bulk* stechiometrico i picchi risultano spostati e allargati per effetto della ridotta dimensione dei grani. Più effetti possono concorrere a determinare lo spostamento dei picchi, ovvero la presenza di una fase ossidata (U_4O_9 o una sua forma deficiente in ossigeno) i cui picchi sono convoluti con quelli della fase stechiometrica, oppure una contrazione del parametro reticolare legata alla dimensione delle particelle.
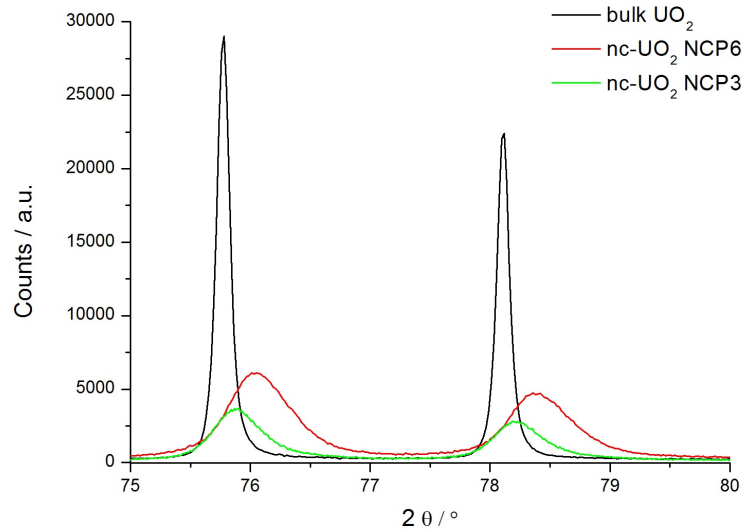
Figura 5: Porzione del diffrattrogramma XRD di due campioni nc-UO$_2$ (rosso e verde) a confronto con quello di UO$_2$ *bulk* (nero). Le differenze nei diffrattogrammi dei campioni nanostrutturati sono dovute a disomogeneità dello stato di ossidazione iniziale e della dimensione dei grani (cfr. 30 $\pm$ 20 nm).
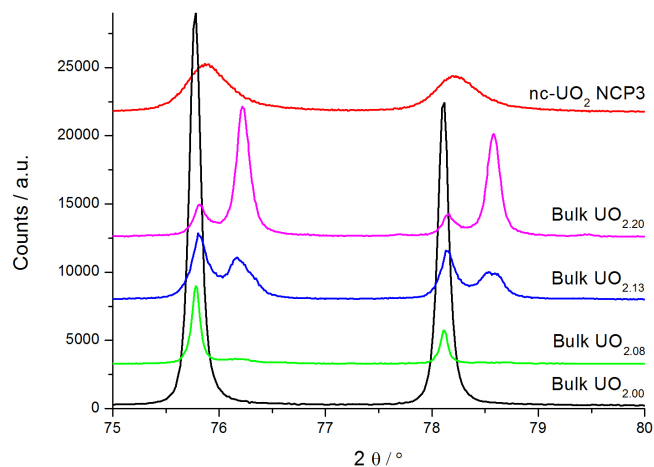
Figura 6: Porzione del diffrattogramma XRD di diversi campioni UO$_{2+x}$ *bulk* e nc-UO$_2$.

L'ipotesi più probabile è che i campioni fossero ossidati, come qualitativamente provato dagli spettri Raman, che hanno rivelato la presenza di picchi caratteristici di U$_4$O$_9$ e U$_3$O$_8$ (Fig. 7).
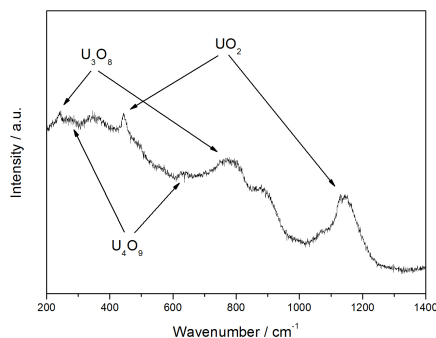
Figura 7: Esempio di spettro Raman di un campione di UO$_2$ nanostrutturato (NCP3). In figura sono indicati i picchi caratteristici dei tre ossidi riconosciuti nel campione.

Tuttavia i diffrattogrammi di nc-UO$_2$ sono chiaramente diversi da quelli di UO$_{2+x}$ *bulk*. In particolare, questo indica che la formazione di U$_4$O$_9$ è ridotta nei campioni nanostrutturati e che anche la dimensione delle particelle ha un effetto, sebbene minore. Una prima stima dello stato di ossidazione è stata fatta con misure di TG, le quali hanno fornito un valore medio $x = 0.15$, dove x indica lo stato di iperstechiometria UO$_{2+x}$. Tuttavia, le misure erano affette da grande incertezza e non completamente affidabili. Un'altra stima è stata fatta supponendo valida la formula riportata da Perio che collega il valore del parametro reticolare allo stato di iperstechiometria [17]: sono state svolte

analisi di raffinamento Rietveld dei diffrattogrammi per ottenere il valore del parametro reticolare da cui è stato ottenuto $x = 0.10 \pm 0.02$, considerato un valore più attendibile.

Determinazione del punto di fusione

In Tabella 1 sono riportati i valori rilevati per la temperatura di fusione e quelle di *solidus* e *liquidus* nei campioni analizzati. Tutti gli esperimenti sono stati svolti in Ar/H_2 per evitare un'ulteriore ossidazione dei campioni.

Tabella 1: Risultati per pastiglie di nc-UO_2. Il simbolo "/" indica che non è stato possibile determinare una chiara transizione di fase nel termogramma o il segnale RLS.

Sample	$T_{fusione}$ / K	δT / K	$T_{liquidus}$ / K	δT / K	$T_{solidus}$ / K	δT / K
NCP1	2750	37	3160	44	3024	42
	2813^a	38	3124	44	/	/
NCP2	2736	37	2924	40	2794	38
	2845^a	39	/	/	/	/
$NCP5^b$	/	/	3080	43	3000	42
$NCP6^c$	2820	38	3098	43	3039	42

[a] Secondo tiro sulla seconda superficie della pastiglia.

[b] Un trattamento termico preliminare in-situ è stato svolto con il laser (potenza 45 W, 10 s). L'agglomerazione delle particelle è certo.

[c] Un trattamento termico preliminare in-situ è stato svolto con il laser (potenza 45 W, 5 s). L'agglomerazione delle particelle è molto probabile.

In Fig. 8 è riportato un esempio di termogramma ottenuto dalla fusione di un campione nanostrutturato rispetto a quello ottenuto nelle stesse condizioni sperimentali per un campione di UO_2 commerciale, la cui temperatura di fusione è di (3120 ± 30) K [9]. Non sono state misurate variazioni nel valore dell'emittanza rispetto al materiale *bulk*, per cui anche per le pastiglie nanostrutturate è stato usato il valore di 0.83 [16].

La temperatura di fusione osservata per pastiglie la cui dimensione dei grani è di (30 ± 20) nm si colloca tra 2730 K e 2850 K.

Tali valori sono comparabili con i valori della temperatura di fusione per campioni *bulk* iperstechiometrici nell'intervallo stimato per il materiale nanostrutturato ($0.08 < x < 0.12$). Per campioni *bulk* di $UO_{2.08}$ e $UO_{2.12}$ essi sono di (2886 ± 25) K e (2699 ± 25) K rispettivamente [18].

Oltre allo svolgimento dell'attività sperimentale, è stato applicato il modello proposto da Pawlow per determinare l'abbassamento della temperatura di fusione nei nanomateriali [19] usando i valori sperimentali riportati in [20]. Tale modello stima un abbassamento della temperatura di fusione per particelle stechiometriche di 30 nm di soli 24 K rispetto al valore del materiale *bulk*. Tuttavia finora il modello si è dimostrato adatto a predire l'abbassamento della temperatura di fusione solo per metalli e non vi sono studi in cui sia stato applicato a materiali ceramici. Perciò il risultato è stato considerato solo indicativo.

In conclusione, è stato quindi dimostrato che le pastiglie nanostrutturate di UO_2 con dimensione dei grani di (30 ± 20) nm sono soggette a una rapida ossidazione, dovuta
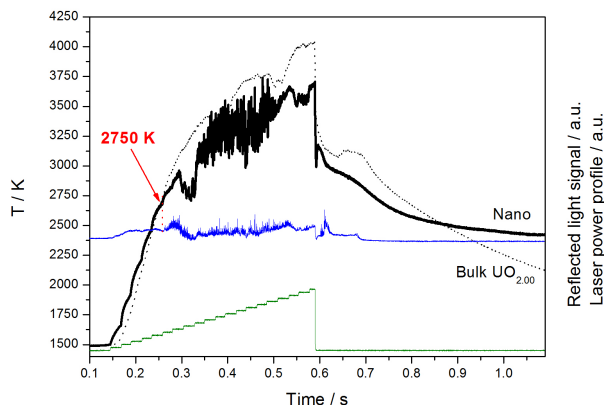
Figura 8: Esempio di termogramma di nc-UO$_2$ (NCP1).

all'aumentato rapporto superficie/volume e che l'abbassamento della temperatura di fusione misurato è dovuto in parte a effetti di dimensione dei grani, ma soprattutto a effetti di non-stechiometria.

Diossido di Torio

Caratterizzazione prima degli esperimenti di fusione

Inizialmente sono stati eseguiti alcuni esperimenti con le particelle non trattate termicamente, ma la massiva, violenta combustione del legante durante il riscaldamento ha reso impossibile la registrazione del termogramma. In seguito, quindi, tutti i campioni sono stati trattati termicamente in un forno all'interno di crogioli in allumina. La Tabella 2 riporta un riassunto dei campioni analizzati in questo lavoro.

Tabella 2: Campioni di nc-ThO$_2$ analizzati in questo lavoro.

Campione	Temperatura del trattamento termico / K
S05	600
S07	700
S08	700
S10	700

Studio del comportamento a fusione

Purtroppo, le polveri pressate a temperatura ambiente erano molto fragili e si sfaldavano facilmente. Gli sforzi termici e meccanici subiti durante il veloce riscaldamento hanno spesso distrutto i campioni totalmente o parzialmente durante la misura, rendendo difficile (o a volte impossibile) determinarne il punto di fusione. Solo in un caso è stato osservato

l'inizio della transizione a (2833 ± 38) K, come riportato in Fig. 9 e Fig. 10, ma non è stato possibile confermare il risultato. Invece, la presenza di liquido a temperature comprese tra 3000 K e 3200 K è stata osservata in diverse misure, confermando che le nanoparticelle di dimensione compresa tra i 3 nm e i 5 nm hanno un punto di fusione ben più basso di quello del *bulk*, pari a (3651 ± 17) K [10]. Il valore della NSE (*Normal Spectral Emittance*) misurato è pari a 0.87, in accordo con quanto determinato per il materiale *bulk* in [16].
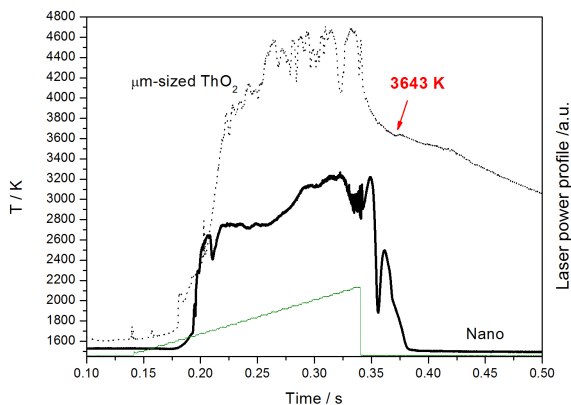
Figura 9: Esempio di termogramma di nc-ThO$_2$ (S05) a confronto con quello di un campione di ThO$_2$ di riferimento con grani micrometrici.
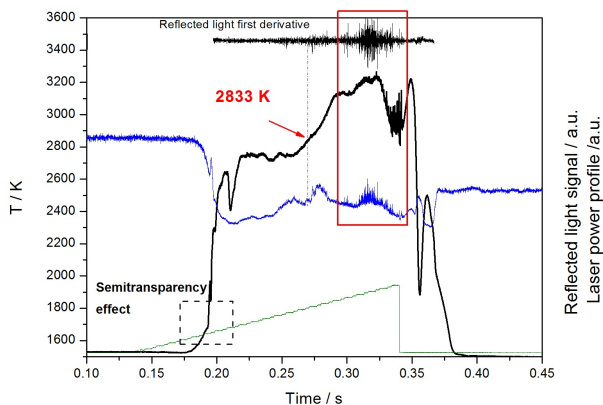
Figura 10: Esempio di termogramma di nc-ThO$_2$ (S05).

Applicazione della spettroscopia Raman per determinazione dell'evoluzione della dimensione dei grani dopo trattamenti termici e fusione

L'assenza di altri ossidi e la elevata sensibilità del ThO_2 allo scattering Raman hanno permesso di usare questa ultima tecnica per una misura semiquantitativa e locale delle dimensioni dei grani in campioni di toria nanostrutturati. Lo stesso tipo di analisi non è stato possibile in campioni di UO_2 nanostrutturati, a causa della rapida formazione di ossidi di uranio "parassiti" sulla superficie.

L'allargamento e lo spostamento dei picchi vibrazionali negli spettri Raman legati al confinamento dei fononi all'interno dei grani sono fenomeni ben noti sperimentalmente nei nanomateriali [21–24].
Sono stati misurati gli spettri Raman di campioni con diverse dimensioni dei grani[2] ed è stata calcolata la larghezza a metà altezza (FWHM) del caratteristico picco T_{2g} della toria (Fig. 11). Essa è stata messa in relazione lineare con l'inverso della dimensione media dei grani, determinata tramite TEM ed XRD (quando possibile). Da ciò è stata ottenuta una curva di "calibrazione" empirica (Fig. 12(a)) tramite la quale è stata successivamente calcolata la grandezza dei grani nel materiale dopo i trattamenti termici e gli esperimenti con il laser, come mostrato in Fig. 12(b). L'analisi mostra che sotto il fascio laser è presente un gradiente termico dalla zona periferica verso il centro. Solo nella zona centrale della pastiglia dove il materiale va incontro a fusione si ha una evidente crescita dei domini cristallini.

L'approccio, seppur con limitazioni ed incertezze, permette una prima, rapida mappatura della struttura cristallina locale dei campioni.
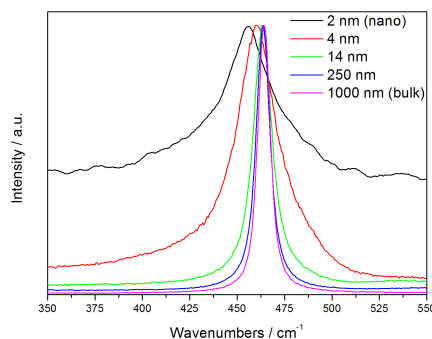
Figura 11: Evoluzione del picco T_{2g} in funzione della dimensione dei grani.

L'analisi qualitativa svolta tramite la spettroscopia Raman è stata confermata con analisi al TEM, le cui immagini hanno mostrato nel campione dopo la fusione la presenza di domini cristallini di alcune centinaia di nanometri (300-500 nm, Fig. 13(a)), ma anche di circa 20 nm (Fig. 13(b)), presumibilmente al bordo della zona fusa.

---

[2]La crescita dei domini cristallini è stata ottenuta trattando i campioni a diverse temperature in un forno sotto flusso di aria.

(a)   (b)
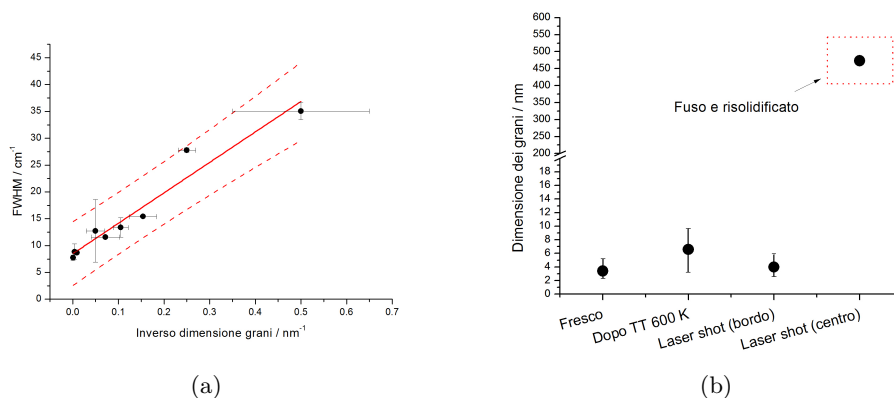
Figura 12: (a) **Curva di "calibrazione": FWHM in funzione dell'inverso della dimensione dei grani. Le curve tratteggiate rappresentano l'intervallo di confidenza al ±95%. Quando la dimensione dei grani→ ∞ le bande di incertezza perdono il loro significato fisico. (b) Esempio di applicazione della spettroscopia Raman per determinare l'evoluzione della grandezza dei grani in un campione di nc-ThO$_2$ (S05) dopo trattamento termico e fusione. Fresco = campione non trattato termicamente; Dopo TT 600 K = campione dopo trattamento termico a 600 K; Laser shot (bordo) = spettro misurato sul bordo della pastiglia dopo esperimento con il laser; Laser shot (centro) = spettro misurato al centro della pastiglia dopo esperimento con il laser. Per la dimensione dei grani fusi e risolidificati non si sono potute assegnare le bande di incertezza.**

(a)   (b)
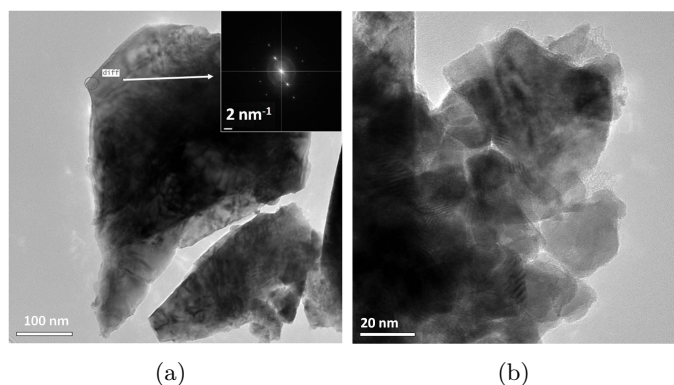
Figura 13: (a) **Immagine TEM del campione S05 dopo fusione. L'inserto corrisponde alla FFT registrata per la zona indicata nella figura. (b) Immagine HRTEM del campione S05 dopo fusione mostrante le agglomerazioni di dimensione media di 20 nm.**

In concluione, benché non sia stato possibile determinare con certezza la temperatura di fusione per i campioni analizzati (dimensione dei grani di 3-5 nm), l'analisi del segnale del laser a bassa potenza (RLS) ha permesso il riconoscimento della presenza di un

abbassamento della temperatura di fusione di almeno 400-600 K rispetto a quella del ThO_2 *bulk*.

Inoltre, è stata implementata una interessante tecnica empirica di analisi locale della grandezza dei grani attraverso lo studio dell'allargamento dei picchi vibrazionali osservato negli spettri Raman.

Conclusioni e prospettive

L'obiettivo principale di questo lavoro è stata l'indagine del comportamento a fusione di UO_2 e ThO_2 nanostrutturati. L'interesse in questi materiali è duplice: da una parte, lo studio delle loro proprietà fornisce nuovi elementi per approfondire la comprensione delle proprietà termofisiche e termodinamiche di ossidi di attinidi nanostrutturati e, per paragone, *bulk*. Dall'altro lato, essi potrebbero essere impiegati, in futuro, come combustibili nucleari avanzati, riproducendo in un materiale non irraggiato le vantaggiose proprietà della struttura ad alto *burn-up* (HBS).

La sintesi di ossidi di attinidi nanostrutturati è molto recente, perciò lo studio delle loro proprietà è agli inizi. Non sono stati svolti altri studi sul loro comportamento a fusione finora. Infatti, tutte le tecniche convenzionalmente usate per lo studio dell'abbassamento del punto di fusione in materiali nanostrutturati non sono applicabili per gli ossidi refrattari, a causa delle loro elevate temperature di fusione.

In questo lavoro è stata impiegata una tecnica di riscaldamento rapido tramite laser, accoppiata con pirometri e metodo RLS, il quale è stato applicato per la prima volta in questo campo di ricerca per lo studio di pastiglie nanostrutturate di urania e toria. Sono state affrontate molte difficoltà sperimentali, soprattutto in seguito alle condizioni estreme prodotte durante gli esperimenti ad alta temperatura. La reattività chimica degli ossidi di attinidi era accresciuta dall'alto valore di superficie specifica tipico dei nanomateriali. In ogni caso, le pastiglie nanostrutturate di UO_2 e ThO_2 sono state fuse con successo usando la citata tecnica, evitando eccessiva crescita dei grani prima della fusione.

Nelle seguenti parti sono riassunti i principali risultati ottenuti in questo lavoro e i possibili futuri sviluppi di questa ricerca.

Conclusioni

In Tabella 3 viene riportato un riassunto dei campioni analizzati nel presente lavoro con i rispettivi risultati.

Per quanto riguarda i campioni di nc-UO_2, la caratterizzazione iniziale ha mostrato che i campioni sono molto reattivi nei confronti dell'ossigeno, anche quando i grani hanno dimensione di diverse decine di nanometri. La temperatura di fusione misurata si colloca tra 2730 K e 2850 K contro i 3120 K del materiale *bulk*. Il risultato è attribuibile sia a effetti di dimensione dei grani, sia di O/M. Da quanto ottenuto nella presente ricerca sembra che significative variazioni rispetto al valore stechiometrico O/M = 2.00 sia il

Tabella 3: Riassunto dei principali risultati sperimentali.

UO$_2$ [(30± 20) nm]		
Campione	T$_{fusione}$ / K	Commenti
NCP1	2750 ± 37	
	2813 ± 38	
NCP2	2736 ± 37	
	2845 ± 39	
NCP5	/	
NCP6	2820 ± 38	
ThO$_2$ [3-5 nm]		
Sample	T$_{fusione}$ / K	Commenti
S05	2833 ± 38	Liquido a 3000-3200 K
S07	/	Liquido a 2880-3100 K
S08	/	vibrazioni RLS da 3150 K
S10	/	Nessun segnale RLS registrato

maggior responsabile nel determinare l'abbassamento della temperatura di fusione per questo tipo di materiale con grani tra i 20 e i 50 nm. L'aumentata reattività potrebbe causare delle limitazioni nell'uso di tale materiale come potenziale combustibile nucleare. Essa è dunque un aspetto cruciale da tenere in conto. Ad esempio, potrebbe essere consigliabile aumentare la dimensione media dei grani a un livello per cui una ossidazione eccessiva venga evitata. Ciò permetterebbe anche di ridurre un ulteriore abbassamento della temperatura di fusione dovuta a effetti di dimensione. Altrimenti, il potenziale di ossigeno di un ipotetico combustibile formato da UO$_2$ nanostrutturato dovrebbe essere mantenuto accuratamente sotto controllo durante l'utilizzo.

È stato svolto anche lo studio del comportamento a fusione di ThO$_2$ nanocristallino con grani molto piccoli (3-5 nm), ma maggiore stabilità chimica. Ciò ha permesso sia di evitare i problemi incontrati maneggiando l'UO$_2$ nanostruturato, sia di studiare il possibile massimo abbassamento nella tempeartura di fusione, come primo passo della ricerca. Purtroppo, i molti problemi sperimentali incontrati (poco materiale disponibile, fragilità dei campioni, ecc.) hanno impedito la determinazione dell'esatto valore della temperatura di fusione in questo materiale. In ogni caso la fase liquida è stata rilevata a temperature di circa 400-600 K inferiori rispetto alla temperatura di fusione del materiale *bulk* (stabilita a 3651 K), confermando che l'abbassamento del punto di fusione dovuto a effetti di dimensione dei grani può essere notevole anche negli ossidi di attinidi.

Prospettive

I risultati ottenuti finora aprono la strada ad ulteriori studi, il cui scopo finale è la determinazione di un relazione tra la temperatura di fusione e la dimensione dei grani per UO$_2$ e ThO$_2$ nanostrutturati.

Le indagini su UO$_2$ nanostrutturato possono essere continuate in due direzioni. Da una parte possono essere condotti nuovi esperimenti su campioni con la stessa dimensione dei grani di quelli usati in questo lavoro (30 nm in media), ma non ossidati oltre O/M = 2.00, per paragonare i risultati con quanto ottenuto finora. Dall'altra, l'indagine di campioni con dimensione dei grani minore sarebbe fondamentale per stabilire la relazione sopra menzionata. Ognuno di questi nuovi obiettivi potrebbe richiedere lo sviluppo di un apparato sperimentale completamente sotto atmosfera inerte per minimizzare il contatto con l'aria.

Per quanto riguarda il ThO$_2$ nanocristallino, invece, un primo passo potrebbe essere l'aumento della resa di sintesi. In questo modo più materiale potrebbe essere pressato ottenendo campioni più resistenti, in modo da completare i risultati qui ottenuti. Il secondo passo della ricerca è la produzione di materiale con dimensione media dei grani più grande. La possiblità di paragonare i risultati di ThO$_2$ e UO$_2$ con dimensione dei grani media di 30 nm porterebbe a una migliore comprensione dei risultati ottenuti finora per UO$_2$ nanocristallino.

In entrambi i casi, lo scopo ultimo di questo settore di ricerca può considerarsi la determinazione della dipedenza del punto di fusione dalle dimensione dei grani cristallini.

Riferimenti

[1] http://itu.jrc.ec.europa.eu/.

[2] J. Spino, H. Santa Cruz, R. Jovani-Abril, R. Birtcher, and C. Ferrero. *J. Nucl. Mat.*, 422:27, (2012).

[3] V.V. Rondinella and T. Wiss. *Materials Today*, 13:24, (2010).

[4] M.J. Takagi. *J. Phys. Soc. Jpn.*, 9:359, (1954).

[5] P. Buffat and J-P. Borel. *Phys. Rev. A*, 13:2287, (1976).

[6] E. Roduner. *Nanoscopic Materials: Size-dependent Phenomena.* RSC Publishing, (2006).

[7] R. Böhler, M. J. Welland, F. De Bruycker, K. Boboridis, A. Janssen, R. Eloirdi, R.J.M. Konings, and D. Manara. *J. Appl. Phys.*, 111:113501, (2012).

[8] F. De Bruycker, K. Boboridis, P. Pöml, R. Eloirdi, R.J.M. Konings, and D. Manara. *J. Nucl. Mater.*, 416:166, (2011).

[9] D. Manara, C. Ronchi, M. Sheindlin, M. Lewis, and M. Brykin. *J. Nucl. Mater.*, 342:148, (2005).

[10] C. Ronchi and J.P. Hiernaut. *J. Alloy Comp.*, 240:179, (1996).

[11] G. Guisbiers. *J. Nanosci. Lett.*, 2:1, (2012).

[12] D. Hudry, C. Apostolidis, O. Walter, T. Gouder, E. Courtois, C. Kübel, and D. Meyer. *Chem. Eur. J.*, 18:8283, (2012).

[13] D. Hudry, C. Apostolidis, O. Walter, T. Gouder, E. Courtois, C. Kübel, and D. Meyer. *Chem. Eur. J.*, 19:5297, (2013).

[14] R. Jovani-Abril. *Synthesis of nanoparticles: processing and properties of nanocrystalline-ceramics.* PhD thesis to be submitted to the Universidad de Santiago de Compostela.

[15] R. Jovani-Abril, R. Eloirdi, D. Bouexière, R. Malmbeck, and J. Spino. *J. Mater. Sci.*, 46:7247, (2011).

[16] L. Capriotti and A. Quaini. *High temperature behaviour of nuclear materials by laser heating and fast pyrometry.* Master's thesis, Politecnico di Milano, (2011).

[17] P. Perio. *Contribution to the Crystallography of the Uranium - Oxygen System.* PhD thesis, University of Paris CEA-363, (1955).

[18] D. Manara. *Melting transition measurements in uranium dioxide.* PhD thesis, University of Warwick, (2004). Technical Note JRC-ITU-TN-2004/05.

[19] P. Pawlow. *Z. Phys. Chem.*, 65:1, (1909).

[20] J.K. Fink. *J. Nucl. Mater.*, 279:1, (2000).

[21] R.J. Nemanich and S.A. Solin. *Phys. Rev. B*, 20:392, (1979).

[22] A. Li Bassi, D. Cattaneo, V. Russo, C.E. Bottani, E. Barborini, T. Mazza, P. Piseri, P. Milani, F.O. Ernst, K. Wegner, and S.E. Pratsinis. *J. Appl. Phys.*, 98:074305, (2005).

[23] Z.V. Popović, Z. Dohčević-Mitrović, M.J. Konstantinović, and M. Šćepanović. *J. Raman Spectrosc.*, 38:750, (2007).

[24] A.K. Arora, M. Rajalakshmi, T.R. Ravindran, and V. Sivasubramanian. *J. Raman Spectrosc.*, 38:604, (2007).

Introduction

Nanoparticles and Nanomaterials

According to ISO Technical Specifications, nano-objects, nanoparticles and nanomaterials have the following definitions [1, 2]:

- **Nano-object**: material with one, two or three external dimensions in the nanoscale (from 1 nm to 100 nm);

- **Nanoparticle**: nano-object with all three external dimensions in the nanoscale;

- **Nanomaterial**: material with any external dimension in the nanoscale or having internal or surface structure in the nanoscale.

In the last decades, nanomaterials have gained broad scientific and technological interest due to their unusual properties compared to µm-sized materials. Nanomaterials are intermediate in size between isolated atoms or molecules, and µm-sized materials (also called "bulk" materials). At this scale, matter shows exceptional properties.
In fact, below 100 nm properties such as melting point, thermal conductivity, colour, ionisation potential, hardness, catalytic activity and selectivity, or magnetic properties such as coercivity, permeability and saturation magnetisation start to change depending on the size. The changes also depend on the number of dimensions that are nanometric in size [3].
Two types of effects as a function of size can be distinguished:

1. *Surface effects*: related to the fraction of atoms at the surface, that are less stable because of the lower coordination number and unfilled bonds. In nanomaterials, the surface-to-volume ratio increases proportionally to the inverse of the particle size, leading to a continuous change in all properties which depend on this ratio. One important example is the change in melting and other phase transition temperatures.

2. *Quantum effects*: in metals and semiconductors the electronic wave functions of conduction electrons are delocalised over the entire particle. Electrons can therefore be described as "particles in a box", and the density of states and the energy levels of the particle depend crucially on the size of the box, so of the particle itself. However, when more atoms are added, the shells are filled up, and discontinuities occur when a new shell starts to be populated. Because of these discontinuities

there is no simple scaling. Properties like absorption and fluorescence wavelengths are therefore tuned between the atomic and bulk values, according to the variation of cluster size.

Surface effects

The surface of a sphere scales with the square of its radius r, but its volume scales with r^3. The total number of atoms N in such a sphere goes linearly with volume. The fraction of atoms at the surface is called *dispersion F*, and it is proportional to the surface-to-volume ratio, i.e. to the inverse radius or diameter, and thus also to $N^{-\frac{1}{3}}$. Basically the same relation holds for long cylinders of radius r and for thin plates of thickness d.

The size dependence of dispersion is illustrated in Fig. 14 for a cube of n atoms along an edge and a total of $N = n^3$ atoms. The number of atoms at the surface is $6n$ corrected for double counts at the 12 edges and for reinstalling at 8 corners. For large N the edge and corner corrections become negligible, leading to the $N^{-\frac{1}{3}}$ scaling [3]:

$$F = \frac{6n^2 - 12n + 8}{n^3} \approx \frac{6}{N^{\frac{1}{3}}} \tag{3}$$
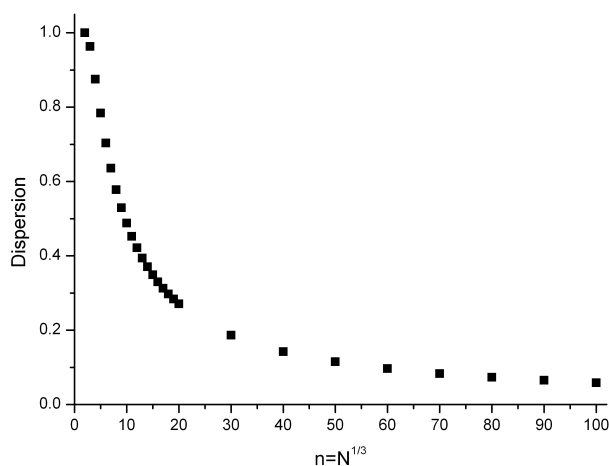
Figure 14: Dispersion relation [3].

For a macroscopic object ($N \approx N_{\text{Avogadro}}$), the surface atoms comprise a negligible proportion of the total number of atoms and will therefore play a negligible role in the bulky properties of the material. Nevertheless, it can be seen from Fig. 14 that, when the number of total particles reduces, the proportion of surface atoms is no longer negligible.

Atoms at the surface have fewer direct neighbours than atoms in the core. Therefore, particles with a large fraction of atoms at the surface have a low mean *coordination number*, which obey the same scaling law [3].

From Nanotechnology to Nano-Nuclear Technology

The application of scientific knowledge to control and utilize matter at the nanoscale, where properties and phenomena related to size or structure can emerge is the definition of nanotechnology [2]. On 29 December 1959, at the annual meeting of the American Physical Society, Richard Feynman addressed the audience with his legendary lecture under the title "*There is Plenty of Room at the Bottom: Invitation to Enter a New Field of Physics*" [4]:

> I would like to describe a field, in which little has been done, but in which an enormous amount can be done in principle. [...] Furthermore, a point that is most important is that it would have an enormous number of technical applications.
>
> What I want to talk about is the problem of manipulating and controlling things on a small scale.

With his talk, Feynman inspired the field of a new science including chemistry, physics, materials science and engineering.

Feynman's imagination found later the possibility to become true: starting from the 1980s' new techniques for exploring matter at nano-scale have been developed, such as the scanning tunneling microscope in 1981 [5]. From then on, scientists have put great effort in the study of nanomaterials and nowadays it is possible to manipulate such structures, opening up unpredictable possibilities for designing and manufacturing new tailored functional materials.

At the present time, nanomaterials are studied to be employed in many different fields: pharmacy and medicine, DNA technology, information storage devices manufacturing and electronics, just to mention some of them.
In particular, one of the most attractive and challenging field of employment is energy. In its report, the Basic Energy Sciences Advisory Committee addressed three strategic goals for which scientific breakthroughs are urgently needed [6]:

1. Making fuels from sunlight;

2. Generating electricity without carbon dioxide emissions;

3. Revolutionizing energy efficiency and use.

Meeting these goals goes at the edge of present capability in producing efficiently energy and points out the necessity of finding new materials that operate at higher levels of functionality and performance. A first approach under study to get rid of fossil fuels, to reduce the CO_2 emissions, is making energy from sunlight, water and biomass [6].

Another carbon-free energy source is nuclear power. Compared to present performances, it could be potentially much more efficient and safer, but much effort has to be put into practice to face issues like the permanent disposal of nuclear waste, the

proliferation of nuclear weapons technologies and materials, and the sustainability of the nuclear fuel cycle [7].

In all of these areas, the performance of materials and chemical processes under extreme conditions is a limiting factor. Nanomaterials and nanotechnologies are expected to be capable of playing significant roles for advancing nuclear science and have vast application potentials at all stages of advanced nuclear fuel cycles. Five fields of potential application have been pointed out [8]:

1. radiation sensors;

2. thermo-hydraulics;

3. separation techniques and waste management;

4. structural materials;

5. fuels.

The use of nanomaterials for sensors with improved sensitivity could minimize their size and weight while increasing performance and functionality [8].

Nano-fluids[3] have better thermal conductivity compared to standard fluids [9] and an enhancement of critical heat flux was proved [10]. Hence, their use could increase the margin of safety to avoid departure from nucleate boiling (DNB)[4], that means also the possibility to upraise power.

Several studies have been implemented about nanoporous materials design in order to develop a direct separation process for minor actinides [12]. Also synthesis of UO_2 and ThO_2 nanoparticles have been implemented to study structural and transport properties in geological repositories for the long-term safety of nuclear waste disposal [13].

Interest about nano actinide oxides, in particular for nanocrystalline UO_2, arose after the observation of ameliorate physical properties in the peripherical zone of fuel irradiated at high burn-up that has undergone a recrystallization in the nanometer-size range [14]. The originally large grains (10-20 μm) after prolonged irradiation re-organise to recover from damage into a new structure called High Burn-up Structure (HBS), with grains of approximately 150-300 nm [15, 16]. The grain subdivision and recrystallization processes take place at the critical local burn-up of 70 GWd/tM and at temperatures below 1073-1373 K [14, 16]. A critical review about the HBS is given in [16].
Various aspects of the newly formed structure have been investigated: improvements include a verified fracture toughness increase [17] and a potentially increased plasticity [18]. Not less important is the fact that the increased number of grain boundaries plays an important role as sinks for recombination of defects, suggesting that the structure can be more resilient to radiation damage [19].

---

[3]A nano-fluid is a fluid base, i.e. water, containing nanometer-sized particles (metals, metal oxides, carbides, carbon or polymers) which form colloidal suspensions.
[4]For further details about DNB see [11].

In addition, also the formation of new closed pores in the matrix is present, whose size is around 1 μm. They entrap most of the fission gases and volatile elements (Xe, Kr, Cs, I for example) [20], leading to a better fission gas retention capability [21, 22].

All these advantages suggest the possibility to synthesise and use in the future nanocrystalline actinide oxides as potential advanced fuels [14].

On the other hand, several open questions are still present about the stability of such materials at high temperatures and possible deterioration of thermophysical properties [14].

In particular, two properties are of fundamental importance:

1. the thermal conductivity;

2. the melting temperature.

They occur in the definition of thermal limits of the fuel rods, since the maximum temperature of fuel (T_{max}) must be, under all circumstances, lower than melting temperature. The criterion is set to avoid the migration of molten fuel towards cladding, with possible formation of eutectic mixture with cladding and following loss of structural integrity of the cladding [11].

Moreover, the thermal conductivity (k) and the maximum temperature (T_{max}) are linked to the linear power produced by the fuel rod (q') through the conductivity integral [23]:

$$\int_{T_0}^{T_{max}} k(T)\,dT = \frac{q'}{4\pi} \qquad (4)$$

where T_0 is the outer fuel temperature. As can be seen from eq. (4), both $k(T)$ and T_{max} represent the ultimate limit to define the maximum power of a fuel rod [24]. Fuel performance is thus strongly dependent on both properties, which are among the most important parameters of merit for fuel safety [25].

Both thermal conductivity and melting temperature are affected when the dimension of the grains goes below nanometric scale. Ronchi et al. [26], studying the impact of HBS on the thermal transport properties in the lattice, concluded that the new structure actually provides a net beneficial effect on intrinsic conductivity. On the other side, melting point depression is a well-known phenomenon for free nanoparticles [27, 28].

This work focuses on the investigation of possible melting point depression for nanostructured UO_2 and ThO_2. The technique employed is fast laser heating coupled with pyrometry [29]. Moreover, characterization of the materials both before and after melting has been done using Transmission and Scanning Electron Microscopy (TEM, SEM), X-ray Diffraction (XRD), Thermogravimetry (TG) and Raman spectroscopy.

The thesis is organised as follows. In Chapter 1, thermodynamics applied to nanomaterials is introduced, with a general overview of the models available in literature to explain melting point depression in free nanoparticles. In Chapter 2, an overview of properties for

bulk UO_2 and ThO_2 is given. Then, in the second part, the synthesis of nanostructured UO_2 and ThO_2 is shortly explained, followed by the sample preparation done in this work. In Chapter 3, the experimental set-up and the techniques used for the characterization of the samples are described. In Chapter 4, experimental results are presented, followed by discussion, while final conclusions are given in Chapter 5.

References

[1] ISO Technical Committee. ISO/TS 27687:2008. Nanotechnologies-Therminology and definitions for nano-objects - Nanoparticle, nanofibre and nanoplate. Technical report, ISO, 2008.

[2] ISO Technical Committee. ISO/TS 80004-1:2010. Nanotechnologies-Vocabulary-Part 1: Core terms. Technical report, ISO, 2010.

[3] E. Roduner. *Nanoscopic Materials: Size-dependent Phenomena.* RSC Publishing, (2006).

[4] R.P. Feynman. Engineering Science. http://www.zyvex.com/nanotech/feynman.html, (1960).

[5] G. Binnig, H. Rohrer, Ch. Gerber, and E. Weibel. *Phys. Rev. Lett.*, 49:57, (1982).

[6] Basic Energy Sciences Advisory Committee. New science for a secure and sustainable energy future. Technical report, U.S. Department of Energy, December (2008).

[7] Office of Basic Energy Sciences. Basic research needs for advanced nuclear energy systems: Report of the basic energy sciences workshop on basic research needs for advanced nuclear energy systems. Technical report, U.S. Department of Energy, October (2006).

[8] TMS and U.S. Department of Energy. *NanoNuclear 2012*, 6-8 June 2012.

[9] Buongiorno et al. *J. Appl. Phys.*, 106:094312, (2009).

[10] H.S. Ahn and M.K. Kim. *J. Heat Transfer*, 134:024001, (2011).

[11] C. Lombardi. *Impianti nucleari.* Polipress, (2009).

[12] Y.Z. Wei, A.Y. Zhang, M. Kumagai, M. Watanabe, and N. Hayashi. *J. Nucl. Sci. Technol.*, 41:315, (2004).

[13] O.N. Batuk, D.V. Szabó, M.A. Denecke, T. Vitova, and S.N. Kalmykov. *Radiochim. Acta*, 101:233, (2013).

[14] J. Spino, H. Santa Cruz, R. Jovani-Abril, R. Birtcher, and C. Ferrero. *J. Nucl. Mat.*, 422:27, (2012).

[15] Hj. Matzke and J. Spino. *J. Nucl. Mat.*, 248:170, (1997).

[16] V.V. Rondinella and T. Wiss. *Materials Today*, 13:24, (2010).

[17] J. Spino, J. Cobos-Sabate, and F. Rousseau. *J. Nucl. Mat.*, 322:204, (2003).

[18] J. Spino, H. Santa Cruz, R. Birtcher, C. Ferrero, R. Pierritz, and A. Fernández. Workshop on radiation stability of complex microstructures. Santa Fe (USA), September 02-04 (2008).

[19] N. Nita, R. Schaeublin, M. Victoria, and R.Z. Valiev. *Philos. Mag.*, 85:723, (2005).

[20] J. Spino, K. Vennix, and M. Coquerelle. *J. Nucl. Mat.*, 231:179, (1996).

[21] J. Spino, D. Papaioannou, and J.-P. Glatz. *J. Nucl. Mat.*, 328:67, (2004).

[22] J.-P. Hiernaut, T. Wiss, J.-Y. Colle, H. Thiele, C.T. Walker, W. Goll, and R.J.M. Konings. *J. Nucl. Mat.*, 377:313, (2008).

[23] N.E. Todreas and M.S. Kazimi. *Nuclear Systems I*. Taylor Francis, (1993).

[24] D.R. Olander. *Fundamental Aspects of Nuclear Reactor Fuel Elements*. Technical Information Center, Office of Public Affairs Energy Research and Development Administration, (1976).

[25] C. Ronchi. *High Temperature*, 45:552, (2007).

[26] C. Ronchi et al. *J. Nucl. Mater.*, 327:586, (2004).

[27] M.J. Takagi. *J. Phys. Soc. Jpn.*, 9:359, (1954).

[28] P. Buffat and J-P. Borel. *Phys. Rev. A*, 13:2287, (1976).

[29] D. Manara, M. Sheindlin, W. Heinz, and C. Ronchi. *Rev. Sci. Instrum.*, 79:113, (2008).

Chapter 1

Nanothermodynamics

This chapter gives a general overview of theoretical aspects of thermodynamics applied to nanomaterials, with particular attention to solid-liquid transition. In the second part, models found in literature to predict melting point depression are briefly summarized.

Many theoretical problems arise when dealing with thermodynamics of finite size systems. The issue of application of the thermodynamics on nanoscale has been largely debated in the last few decades. In fact "classical" thermodynamics and its connection to statistical physics are strictly valid only in the thermodynamic limit, i.e. when the number of particles involved tends to infinite. This assumption is clearly no more valid when speaking about small systems such as either isolated or agglomerated nanoparticles [1].

When talking about finite size thermodynamics we should distinguish between two types of systems: a single nanoscopic ensemble, and a system that contains a large number of nanoscopic ensembles.

In the first case, a break-down of thermodynamics can occur [1]. In macroscopic thermodynamics, since the number of particles goes to infinity, all but the most probable distribution over possible states can be neglected. This is no longer true for small value of N, where also thermal fluctuations become increasingly important [1,2]. Furthermore, phase transitions are collective phenomena, related to the statistical average over the ensembles. As a consequence, with a statistically non-significant number of particles the concept of phase transition loses its meaning. Small clusters behave more like molecules than bulk matter, hence they can exist in phase-like forms that do not exist for bulk matter. Such forms may coexist over bands of temperature and pressure [1]. For these systems an independent theory has to be developed, which goes beyond the scope of this thesis.

Instead, in the case of a large number of nanoscopic systems, the material behaviour can still be explained by basic thermodynamic equations of macroscopic systems adding some corrections which take into account the finite-size of the system.

A phase transition occurs when a phase becomes unstable in the given thermodynamic conditions, described with intensive variables (p, T, h, u, s). In particular, when the system is described with the state variables (p, T), the Gibbs free energy G (or thermodynamic

potential) is commonly used. A stable phase corresponds thus to the minimum of thermodynamic potential G [3].

It was mentioned before that nanoparticles are characterized by the fact that the ratio between the number of surface and volume atoms is not small, so that the effect induced by the surface on the cohesive properties of the material cannot be neglected. Thus, when we describe the thermodynamic state of a system in terms of thermodynamic potentials, we should add contributions coming from surface or interface (e.g.: interaction with hosting matrix or substrate).

As a consequence, the stable states of the system are no longer governed by the sole volumic Gibbs free energy $G_v(T)$, but a generalised Gibbs free energy must be used to take into account contributions from the particle volume, surfaces/interfaces, edges and corners. However, the last two terms are negligible at sizes above about 10000 atoms [4].

The generalised Gibbs free energy $G^*(T)$ per mole of material can be written as [5],

$$G^*(T) = G_v(T) + G_{surface/interface}(T) \tag{1.1}$$

where $G_{surface/interface}(T)$ is either the surface free energy of the particle or the interfacial free energy between the particle and the substrate/host matrix.

Considering the solid-liquid transition, the melting temperature is defined as the temperature at which the Gibbs free energy of the solid phase $(G_s(T))$ is equal to the Gibbs free energy of the liquid phase $(G_l(T))$ [3]. When a nanostructured solid is considered, the total free energy of the solid phase changes as expressed in (1.1), causing a change in the equilibrium temperature with the liquid phase[1]. In fact, the new equilibrium temperature is defined by the new condition $G^*(T) = G_l(T)$.

According to the relative contribution of the second term either melting point depression (see Fig. 1.1) or superheating[2] (see Fig. 1.2) is reached.

Changes can be observed by varying the size of the grains (affecting the relative weight in (1.1) of the volumic and surface term). Beyond a certain size, the crystal can become unstable, favoring either a transition to another crystalline structure or an amorphous, hence disordered structure. This means that the crystallite size imposes the crystalline or amorphous state in the same way as the temperature or the pressure [2].

In the same way, a modification of the surface state keeping the dimensions constant can affect phase diagrams. For example, this can be done by adding chemicals or embedding nanograins within a matrix. In the latter cases, evaluation of new interface energies and contact angle with substrate/matrix are necessary [5].

---

[1]The liquid produced from nc-solids might have different properties with respect to the one produced by bulk material. However, in the present treatment, the assumption is made that the liquid produced from nc and bulk solid have the same nature.

[2]i.e., an increase in melting temperature compared to the one of bulk material.
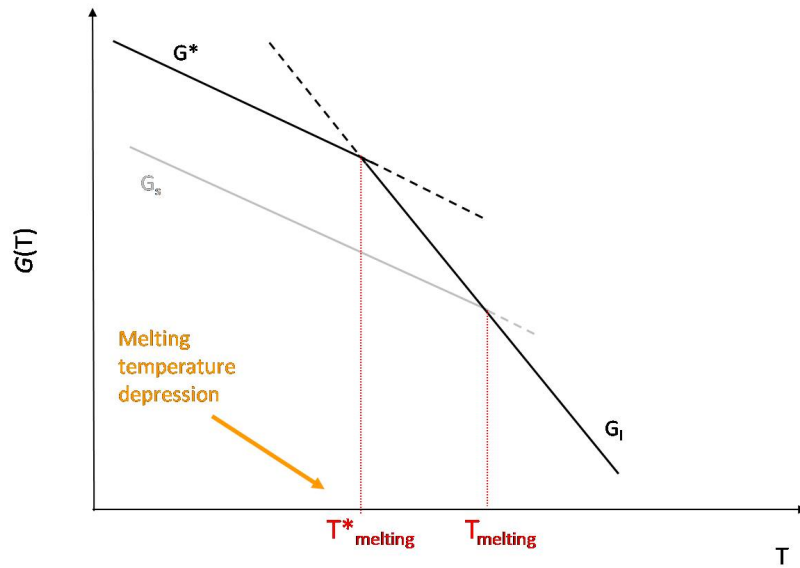
Figure 1.1: **An example of melting point depression.** G_s: **Gibbs free energy of the solid phase,** G_l: **Gibbs free energy of the liquid phase,** G^*: **Gibbs free energy of the nanostructured solid phase. The nanostructured solid has less negative energy compared to the bulk solid because of the surface/interface term. This makes the equilibrium temperature lower compared with the one between the bulk solid and the liquid.**
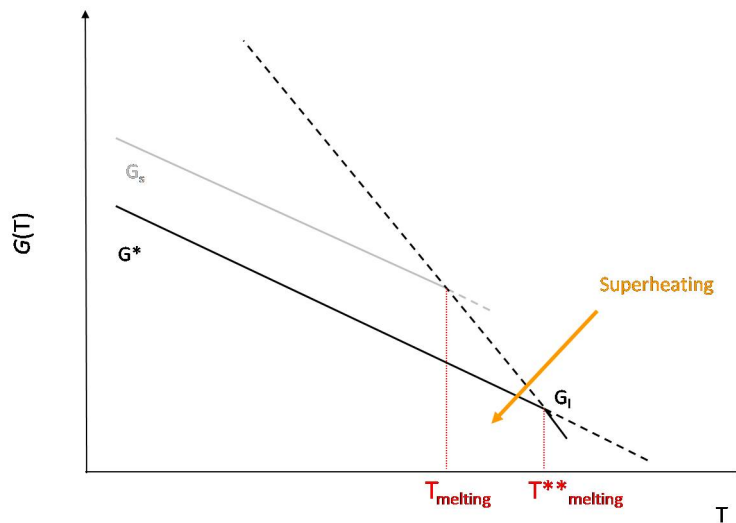
Figure 1.2: **An example of superheating.** G_s: **Gibbs free energy of the solid phase,** G_l: **Gibbs free energy of the liquid phase,** G^*: **Gibbs free energy of the nanostructured solid phase. The nanostructured solid has more negative energy compared to the bulk solid because of the surface/interface term. This makes the equilibrium temperature higher compared with the one between the bulk solid and the liquid.**

11

Among phase transitions, melting is one of the most fundamental because it is related to processing and applications of materials. Therefore, besides its scientific interest, investigations on it have interdisciplinary importance.

Melting behaviour of materials is thus intensively studied from bulk to nanometer-sized clusters. Nevertheless, a general comprehensive theory of the phenomenon is still not available, but many analytical models have been developed since 1800. They can be summarized into two different groups: one taking into account only the initial solid phase, the other dealing with both solid and liquid phase and their interactions over the process of melting.

Among one-phase models, various mechanisms to explain the occurrence of solid structure instability have been suggested: Lindemann [6] considers vibrational behaviour as the cause of melting. He assumes that phase transition occurs when the amplitude of atomic thermal vibrations reaches a critical fraction of the equilibrium inter-atomic distance, leading to lattice instability.

Based on Lindemann's criterion, Shi developed a model for size depending thermal vibrations and melting in terms of the ratio between the amplitude of thermal vibrations for surface atoms and that for inner ones [7]. The model showed good agreement with experimental results obtained for both supported and embedded metallic and semiconductor nanocrystals.

Other authors propose defect-induced theories: Wautelet points out vacancies as source of melting point depression ("surface phonon instability") [8,9]. The melting point depression is found to be proportional to vacancy concentration and to the surface-to-volume ratio of atoms in the particles. Since a size reduction favours vacancy formation, vacancy concentration increases when size reduces making the melting temperature size-dependent. An improvement of surface phonon instability model was later proposed by Guisbiers [10].

Mott was the first to suggest that melting can be induced by dislocations [11] and his theory has been later developed by Burakovsky and Preston [12,13]. Granato et al. focused on interstitials which are known to decrease the shear modulus at the melting point, obtaining results similar to Lindemann's criterion [14].

All these models do not take into consideration thermodynamic properties of the forming liquid phase. A complementary point of view can emerge from the other group of models which consider the liquid phase as well.

Historically, Thomson was the first to propose a model for size-dependent melting temperature. He considers a spherical solid particle of diameter D in equilibrium with bulk material ($D \to \infty$) and vapour. Thomson's equation was then derived by Gibbs using Gibbs free energy and now it is known as Gibbs-Thomson equation:

$$\frac{T_m}{T_{m,\infty}} = 1 - \frac{4V_l \gamma_{sl}}{H_{m,\infty} D} \tag{1.2}$$

Melting point depression was also predicted by Pawlow in 1909 [15]. In this case, the spherical solid particle (initial state) is in equilibrium with a spherical liquid particle (final state), leading to the following equation:

$$\frac{T_m}{T_{m,\infty}} = 1 - \frac{4\,V_s}{H_{m,\infty}\,D} \left[\gamma_{vs} - \gamma_{lv} \left(\frac{\rho_s}{\rho_l} \right)^{\frac{2}{3}} \right] \qquad (1.3)$$

In eqs. (1.2) and (1.3), the used symbols are: $\frac{T_m}{T_{m,\infty}}$ the ratio of nanoparticles and bulk material melting temperatures, V_l is the molar volume of the liquid, V_s the molar volume of the solid, $H_{m,\infty}$ the value of melting enthalpy of the bulk material, γ_{sl} is the solid-liquid interface tension or energy, γ_{sv} and γ_{lv} the solid-vapour and liquid-vapour interface tension or energy, respectively, D the nanoparticles diameter, ρ_s and ρ_l solid and liquid densities.

As was pointed out by Rie [16], Pawlow's hypothesis of a solid sphere in contact with the vapour during melting can not be considered correct. In fact, during melting, the solid phase is in contact with the liquid phase which starts to form on the surface, not with the vapour.

Wronski used this issue as starting point to develop another theoretical model, nowadays called "liquid-skin model". He assumed that the outer layers of a crystal melt first. This idea had already been pursued by Reiss and Wilson [17], but assuming that the liquid shell is indefinitely thin. Instead, Wronski assumes a finite thickness. The resulting equation is:

$$\frac{T_m}{T_{m,\infty}} = 1 - \frac{4\,V_s}{H_{m,\infty}\,D\,\rho_s} \left[\frac{\gamma_{sl}}{1 - \frac{2\delta}{D}} + \gamma_{lv} \left(1 - \frac{\rho_s}{\rho_l} \right) \right] \qquad (1.4)$$

where all symbols have the same meaning as in eqs. (1.2) and (1.3), and δ is the thickness of liquid shell surrounding the solid core.

Buffat and Borel derived eq. (1.3) expanding chemical potential in power series around equilibrium bulk melting point (T_0, P_0) [18]. In eq. (1.3), bulk values are used for all thermodynamic properties present[3]. Surface energies are set as free parameters to fit experimental data to obtain them with good agreement with theoretical values. They also implemented calculations for equation (1.4). Their experimental data also agreed satisfactorily with the predictions of the second phenomenological model, with δ and the interfacial tension as free parameters [18].

In general, all models predict a universal relation between melting temperature and particle size:

$$\frac{T_m}{T_{m,\infty}} \propto 1 - \frac{\alpha}{D} \qquad (1.5)$$

where D and $\frac{T_m}{T_{m,\infty}}$ have the same meaning as in eq. (1.2) and (1.3). The symbol α is a general constant depending on the model used.

---

[3]It was proved that, for instance, the melting enthalpy of nanoparticles can be smaller compared to the value of melting enthalpy of bulk material and size-dependent [19]. Furthermore, also densities and surface energies are likely to be size-dependent. Nevertheless, the use of bulk material properties that are often well known gives a satisfactory prediction of the trend of melting point depression with size [18].

The general trend predicted by eq. (1.5) has often shown good agreement with experimental values obtained for several metals [18, 20, 21]. Instead, no experimental studies about high-melting nanosized oxide materials have been carried out until now, thus it is not sure if these models can be applied in the case of nanostructured actinide oxides as guideline for melting point depression estimation.

Another way to approach the problem is through computer simulations, using more advanced methods of calculation. Recently, molecular dynamics simulations [22] and advanced phase-field theory of melting coupled to mechanics [23] have been employed, but they can be considered beyond the purpose of the current work.

References

[1] E. Roduner. *Nanoscopic Materials: Size-dependent Phenomena.* RSC Publishing, (2006).

[2] C. Brechignac, P. Houdy, and M. Lahmani. *Nanomaterials and Nanochemistry.* Éditions Belin Paris, french edition, (2006).

[3] A.R. Ubbelohde. *The molten state of matter.* Wiley, (1978).

[4] A.S. Barnard and P. Zapol. *J. Chem. Phys.*, 121:4276, (2004).

[5] W. Luo, W. Hu, K. Su, and K. Li. *J. Appl. Phys.*, 112:014302, (2012).

[6] F.A. Lindeman. *Z. Phys.*, 11:609, (1910).

[7] F.G. Shi. *J. Mater. Res.*, 9:1307, (1994).

[8] M. Wautelet. *Phys. Lett. A*, 108:99, (1985).

[9] M. Wautelet. *J. Phys. D: Appl. Phys.*, 24:343, (1991).

[10] G. Guisbiers. *J. Phys. Chem. C*, 115:2616, (2011).

[11] N.F. Mott. *Proc. Roy. Soc. London A*, 215:1, (1952).

[12] L. Burakovsky and D.L. Preston. *Solid State Commun.*, 115:341, (2000).

[13] L. Burakovsky, D.L. Preston, and R.R. Silbar. *Phys. Rev. B*, 61:15011, (2000).

[14] A.V. Granato, D.M. Joncich, and V.A. Khonik. *Appl. Phys. Lett.*, 97:171911, (2010).

[15] P. Pawlow. *Z. Phys. Chem.*, 65:1, (1909).

[16] E. Rie. *Z. Phys. Chem.*, 104:354, (1923).

[17] H. Reiss and I.B. Wilson. *J. Colloid. Sci.*, 3:551, (1948).

[18] P. Buffat and J-P. Borel. *Phys. Rev. A*, 13:2287, (1976).

[19] S.L. Lai, J.Y. Guo, V. Petrova, G. Ramanath, and L.H. Allen. *Phys. Rev. Lett.*, 77:99, (1996).

[20] H.W. Sheng, G. Ren, L.M. Peng, Z.Q. Hu, and K. Lu. *Phil. Mag. Lett.*, 73:179, (1996).

[21] H Jiang, K. Moon, H. Dong, F Hua, and C.P. Wong. *Chem. Phys. Lett.*, 429:492, (2006).

[22] A.S. Boyarchenkov, S.I. Potashnikov, K.A. Nekrasov, and A.Ya. Kupryazhkin. *J. Nucl. Mat.*, 427:311, (2012).

[23] K. Samani and V. Levitas. *Nature Comm.*, 2:99, (2011).

Chapter 2

Materials

In this work, two different actinide oxides are investigated: UO_2 and ThO_2.

Besides a short view of past and present uses of these two materials in bulk form, this chapter gives a general overview of thermodynamic and thermophysical properties of interest to understand their behaviour in a nanostructured form.

In the second part, after a general overview of nanoparticles synthesis processes, the synthesis approaches to obtain nanosized UO_2 and ThO_2 analysed in this study are briefly described.

2.1 Properties of UO_2 and ThO_2

2.1.1 Uranium dioxide

Uranium dioxide (UO_2) was first used as nuclear fuel in 1955 for the Shippingport pressurized-water reactor [1]. Despite its relatively low fissile density and poor thermal conductivity, uranium dioxide was chosen because of its very satisfactory dimensional and radiation stability, chemical compatibility with cladding metals and coolant in light water reactor service and its relative ease of manufacture [2]. It is nowadays the most widely used nuclear fuel. For this reason, UO_2 is one of the most studied compounds. A review of UO_2 properties can be found in [3].

Concerning the U-O phase diagram, six solid uranium oxides are known at room temperature and atmospheric pressure, having the ideal compositions: UO_2, U_4O_9, U_3O_7, U_2O_5, U_3O_8, and UO_3. Each of them is characterised by a variable range of existence as a function of the O/U ratio.
The U-O phase diagram has been recently reviewed by Guéneau et al. [4] using a CALPHAD approach.
The calculated phase diagram is shown in Fig. 2.1(a), and in Fig. 2.1(b) a magnification from 60% to 70% molar oxygen content is given.

Urania ($UO_{2\pm x}$) crystallises in the fluorite structure as shown in Fig. 2.2, space group Fm3m (O_5^h). It has dark grey/black colour.

At high temperature, this crystal form can be found over a remarkably broad range
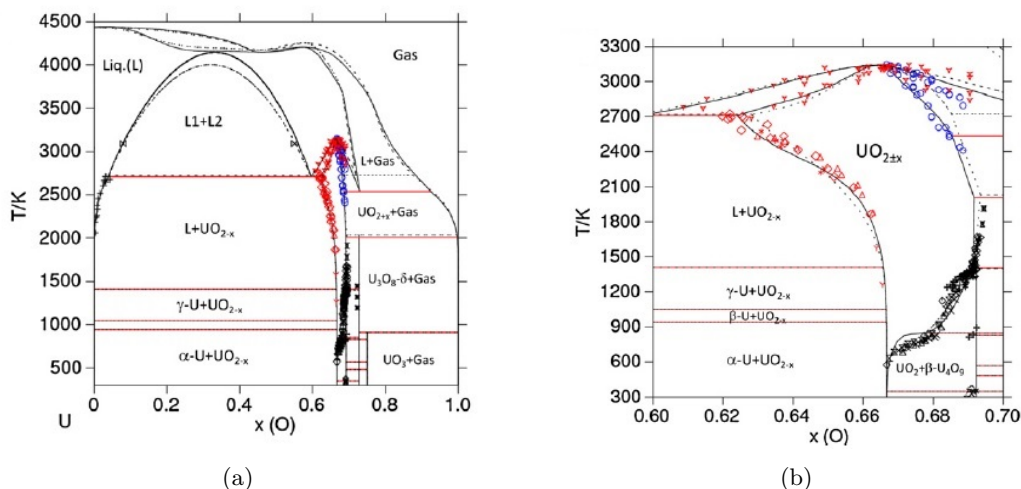
Figure 2.1: (a) Optimised calculated U-O phase diagram; (b) Detailed section from 60 to 70 at.% O. The dotted lines correspond to the calculated phase diagram from [5]. The experimental data come from the critical reviews by Labroche et al. [6] in the UO$_2$-U$_3$O$_8$ composition range and from Baichi et al. [7] in the U-UO$_2$ region and from the experimental work by Manara et al. [8] for the blue points.
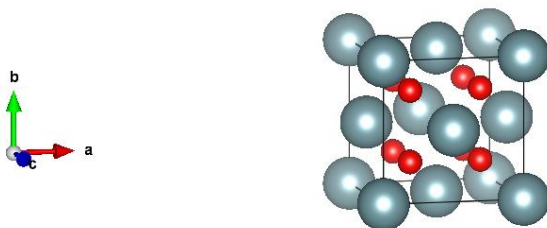
Figure 2.2: Example of fluorite structure.

of nonstoichiometric compositions. For instance, the species UO$_{2+x}$ can exist in the form of a solid solution for approximately $-0.4 < x < +0.3$ at temperatures higher than 2000 K. This occurs by accommodation of oxygen vacancies or interstitial atoms. This feature is made possible by the easy shift of the U valence states $+3$, $+4$, $+5$ and $+6$.

The dioxide melts congruently at (3120 ± 30) K [8–15]. The melting temperature decreases with departure from the stoichiometry, as can be seen from the phase diagram. This feature is particularly problematic when studying size-dependent melting point variations: both O/M variations and the size effect would in fact result in a lower melting point, therefore it is difficult to understand the contribution coming from the size effect only.

2.1.2 Thorium dioxide

Besides nuclear applications, thoria was used for various heat-intensive industrial applications because of its refractory behaviour and its high melting point, the highest among binary oxides. It was employed as a stabilizer in tungsten electrodes for welding and in gas mantles of lanterns [16]. It was also used as the main component of heat-resistant ceramics, such as crucibles for laboratories. Nowadays, for this kind of applications, it has been gradually replaced by non-radioactive and less toxic compounds. Furthermore, it is a catalyst in many chemical reactions, such as petroleum cracking and preparation of sulfuric acid [17].

In the nuclear field, one of the reasons for using thorium in nuclear reactors is the fact that ^{232}Th is a fertile isotope: by neutron capture it can be converted into ^{233}U, a fissile isotope of uranium that does not exist in nature. When a thermal neutron is absorbed by this isotope, thermal breeding in a nuclear reactor is possible [18]. Moreover, a thorium based fuel cycle shows interesting features. Because no ^{239}Pu is produced within the ^{232}Th-^{233}U fuel cycle, this latter can be considered to be an anti-proliferation fuel [19]. In addition, thorium-based fuel displays better thermophysical properties compared to UO$_2$. Among these, as said before, it has higher melting point, a more stable oxidation state and higher thermal conductivity. However, recycling process is more difficult due to the presence of ^{232}U as contaminant. This isotope decays to 1.9-year half life ^{228}Th, which produces strong gamma and alpha emitters in its decay chain [20].

In the past, ThO$_2$ was used as blanket mantel in LMFBR [21] with good results. It was also tested as a U-free matrix fuel in the IFA-652 experiment [22] with the aim of burning Pu-stockpiles without production of new plutonium, showing a good resistance to irradiation as well.

It has the same fluorite structure as urania, but contrary to urania, sintered thoria is white and if melted under oxygen atmosphere it remains colourless, whereas under reducing conditions it becomes dark [23]. Stoichiometric ThO$_2$ has empty *5f* orbitals. The absence of low-energy electrons in the valence band is the cause of the high transparency and the low spectral emissivity in the visible range at room temperature. When the material is heated, emissivity increases steeply [24].
The Th-O phase diagram is reported in Fig. 2.3 [25].
The maximum valence state of thorium is +4, thus compositions with O/Th > 2 do not exist in the condensed phase. As shown in the diagram, ThO$_2$ and the hypostoichiometric ThO$_{2-x}$ solid solution is only stable in a narrow composition range at temperatures higher than 1700 K approximately. Benz's experimental data are well fitted in the optimized phase diagram reported by Kinoshita et al. [26]. A value of $(3573 \pm 100)\,\mathrm{K}$ for the melting temperature of stoichiometric thorium dioxide was reported in literature [27]. More recently, Ronchi and Hiernaut reported the value of $(3651 \pm 17)\,\mathrm{K}$ using laser heating [24]. They investigated also the melting temperature of hypostoichiometric thoria with O/M ratio of 1.98, finding a liquidus temperature of $(3628 \pm 9)\,\mathrm{K}$ indicating a small but significant effect of the stoichiometry deviation.

The better oxidation stability of thoria compared to urania makes this material a good candidate for studying size-dependent melting point depression avoiding some of

the issues encountered with UO_2.
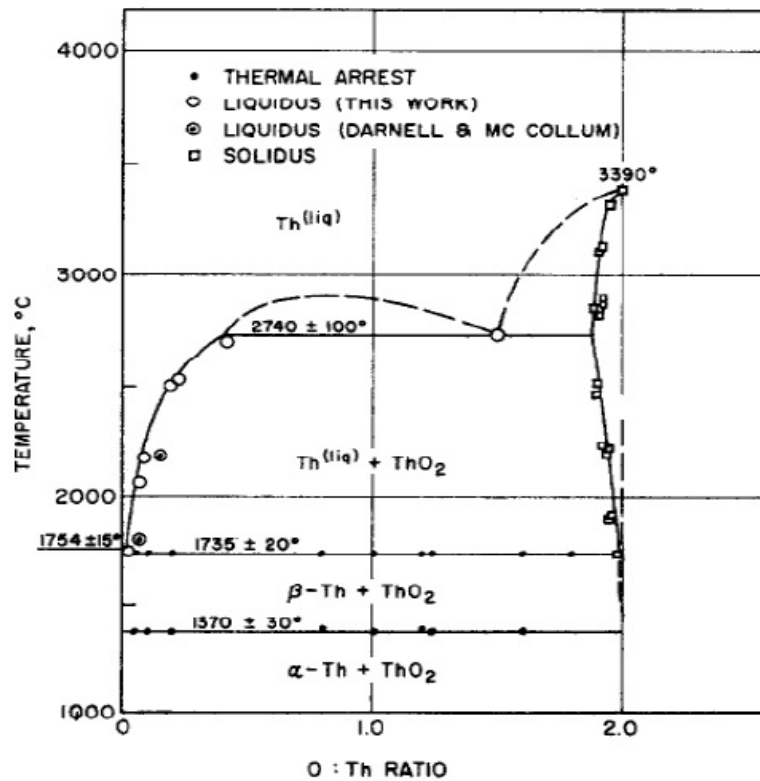
Figure 2.3: Th-O phase diagram [25].

2.2 Synthesis of nanoparticles

Many techniques have been developed and applied for the synthesis of nanoparticles, including both top-down and bottom-up approaches. The former approaches include milling or attrition and repeated quenching [28]. The main drawback of these methods is the relatively broad size distribution of the particles, that leads to inhomogeneous properties. Another type of this kind of techniques is lithography [29].

Bottom-up approaches are far more popular in the synthesis of nanoparticles and many methods have been developed. In the bottom-up approach, nanocomponents are made from precursors in the liquid, solid, or gas phase. Generally speaking, various synthesis techniques can be grouped into two categories: aqueous and non-aqueous processes [30]. Both routes have been applied for actinide nanoparticles synthesis.

In the following section, the classical theory of bottom-up approach is presented. The theory does not explain completely the complex chemical reactions ongoing during the entire process, but it gives a general overview of synthesis main steps as basic

understanding of nanoparticles formation. In particular, the theory is applied very often to explain synthesis through a non-aqueous way [31].

2.2.1 Bottom-up approach: classical theory

In both cases (aqueous and non-aqueous), synthesis process can be ideally summarized in three main steps, following the so-called Lamer diagram (Fig. 2.4) [31]:

  I. Generation of supersaturation;

 II. Nucleation;

III. Growth.
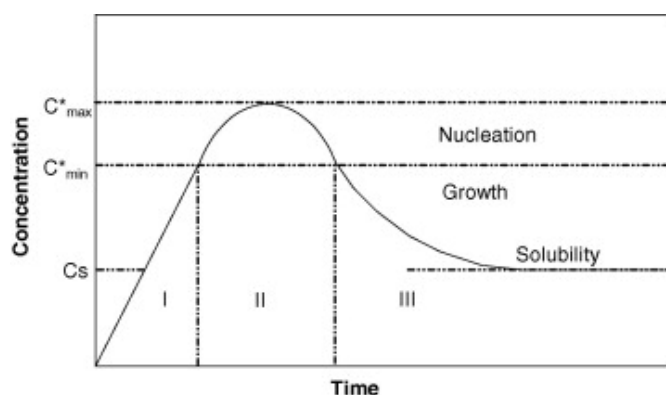
Figure 2.4: Lamer diagram to model nanoparticle synthesis [31].

Nucleation

There are two kinds of nucleation: homogeneous and heterogeneous. Homogeneous nucleation via germs or embryos of a new phase occurs from a homogeneous metastable state, i.e. when the concentration of a solute in a solvent exceeds its equilibrium solubility or temperature decreases below the phase transformation point. Such a solution possesses a high Gibbs free energy which would be reduced by segregating solute. This reduction of energy is the driving force for both nucleation and subsequent growth. Instead, if the crystallization is induced with non-crystalline foreign seeds, the process is called heterogeneous nucleation [32].

The homogeneous reaction has a very high energy barrier and an extremely high supersaturation level is required to start the process. Nevertheless, once started, the process is self-regulating and terminates by itself when the supersaturation level goes below the threshold. This short duration is called "burst nucleation" [32].

It can be assumed that at the beginning a homogeneous single-phase solution exists with a fixed concentration of solute, whose chemical properties are not specified, but

that can be generally modeled through the concept of monomer M, the smallest unit of a crystal [31].

The classical nucleation theory predicts that the total free energy cost, ΔG_{tot}, of forming a solid spherical nucleus of radius r in a liquid consists of a bulk volume and a surface contribution [33]:

$$\Delta G_{tot} = 4\pi r^2 \gamma + \frac{4}{3}\pi r^3 \Delta G_v \tag{2.1}$$

where γ is the surface energy per unit area and ΔG_v is the Gibbs free energy per unit volume of a crystal, which is dependent on the level of supersaturation S:

$$\Delta G_v = -\frac{RT \ln S}{V_m} \tag{2.2}$$

S is defined as $\frac{[M]}{[M]_0}$, where $[M]_0$ is the equilibrium monomer concentration, $[M]$ is the monomer concentration in the solution, R is the Boltzmann constant, T is the temperature, V_m is the molar volume of the monomer in crystal. If $S > 1$, the volume term enhances the formation of a new phase, but the creation of a surface requires an extra free energy term. Therefore, the function shows a maximum, below which the formation of the new phase is energetically unfavorable. This maximum corresponds to a critical radius r_c, the minimum size that nuclei can have in order to resist dissolution. It is straightforward to obtain its expression from the relation $\frac{\Delta G_{tot}}{dr} = 0$, at $r = r_c$:

$$r_c = \frac{2\gamma V_m}{RT \ln S} \tag{2.3}$$
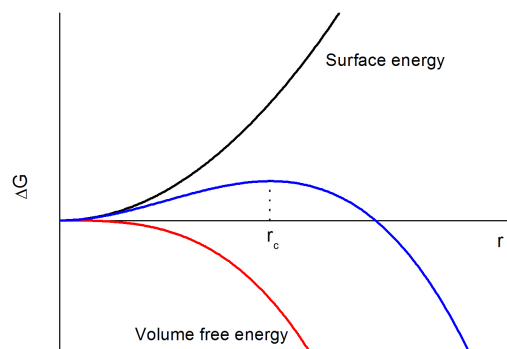
Figure 2.5: Change of the free energy due to the formation of a spherical crystal [31].

The reaction rate for the formation of N nuclei can be modeled using Arrhenius equation [31], where the energy formation is ΔG_{tot}, obtaining:

$$\frac{\mathrm{dN}}{\mathrm{dt}} = A\,exp\left[\frac{16\pi V_m^2 \gamma^3}{3k_b^3 N_A^2 T^3 \left(\ln S\right)^2}\right] \tag{2.4}$$

where A, k_b, N_A and T are the exponential constant, the Boltzmann constant, Avogadro's number, and temperature, respectively. Parameters such as γ and V_m are strictly defined only for a bulk solid, but they can be used also for small clusters, fitting quite well experimental data [34].

In eq. (2.4), there are three controllable parameters:

1. the level of supersaturation,

2. temperature,

3. surface free energy.

Experimentally, many properties of the initial solution can be varied to change the nucleation rate. For instance, in the non-aqueous solution, the nature and composition of the organic system is fundamental for nucleation [35], whereas for the aqueous process the acidity of the solvent can be crucial [30].

Growth

After the formation of nuclei, growth takes place. Diffusive transport of the monomers from the solution onto the crystal surface is the first step, followed by surface reaction.

For a growing spherical particle of radius r as in Fig. 2.6, the total flux of solute passing through a spherical surface with radius x obeys Fick's law [36]:

$$J = 4\pi x^2 D \frac{\mathrm{d}\,[\mathrm{M}]}{\mathrm{dx}} \tag{2.5}$$

where D is the diffusion coefficient, $[M]$ is the monomer concentration in the solution.
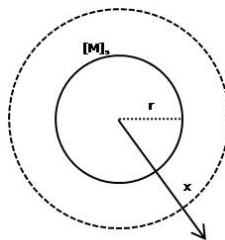
Figure 2.6: The scheme of diffusion model of a spherical particle [36].

On the other hand, for mass balance, J is also equal to the monomer consumption rate by the surface reaction of the particle, thus the flux is also proportional to the reaction constant k:

$$J = 4\pi r^2 k \left([M]_s - [M]_r\right) \tag{2.6}$$

where $[M]_s$ and $[M]_r$ are the monomer concentration at the crystal surface and the concentration of particles of radius r, respectively.

A useful parameter that can be defined is the dimensionless variable:

$$H = \frac{D}{kr}$$

.

It represents the relative contribution of diffusion process against surface reaction.

If $H >> 1$ (thermodynamic equilibrium approach), the monomers transported precipitate immediately onto the surface, the growth rate is inversely proportional to particle radius [31], resulting in a faster growth of smaller particles than the larger ones. The result is a "size focusing" and a narrow size distribution. If $H << 1$ (kinetic approach), the growth rate is the same regardless of the size of the particles, leading to a weaker tendency to approach a monodisperse distribution of the particle size, i.e. to have particle with the same shape and size narrowly distributed around a single value.

Nevertheless, the crystallization process is reversible and part of the crystal changes to solute via dissolution. When the solute concentration is low and therefore the crystallization driving force weak, the dissolution reaction is faster for the more instable small particles, while the larger ones keep growing by receiving monomers from the dissolving particles. This process is called Ostwald ripening [31].

2.2.2 Synthesis of actinide oxide nanocrystals

Nanostructured actinide compounds have been synthesised only in the last decade. In particular, at ITU, UO_2, ThO_2 and NpO_2 nanocrystals have been synthesized following two different approaches: a non-aqueous synthesis through the heating-up method, and an aqueous one, based on the electrochemical reduction of $U(VI)$ into $U(IV)$ and the precipitation of UO_2 in reducing and anoxic conditions at a constant pH. The synthesis was realised in the Nuclear Fuels Unit and in the Nuclear Chemistry Unit.

Non-aqueous synthesis: heating-up method

This group of synthetic methods consists in the preparation of the reaction mixture at low temperature. The solution in then heated up to the reaction temperature, at which crystals formation takes place [30].

The full mechanism governing the process is still not clear, and opposite results can be obtained according to the kind of compound produced. According to some experimental investigations, the synthetic process via heat-up method is composed of two sequential steps: the first step is the thermal decomposition of a precursor, and the second is the nucleation and growth of the nanostructures [37]. Between these two steps, intermediate species exist transiently. They can be generated gradually from either the thermal decomposition of the starting complex or from more complex chemical reactions. It is assumed that these intermediate species act as monomers for the formation of oxide nanoparticles.

In the particular case of actinide-based nanoparticles, many differences were found in the synthesis processes of UO_2 and ThO_2 nanoparticles [35].

For UO_2 synthesis was possible in different organic media[1], whereas for ThO_2 only one type of organic system allowed ThO_2 nanoparticles formation [35]. The resulting mixtures were then heated up to 553 K. After being cooled to room temperature, the NCs were precipitated with ethanol followed by centrifugation and re-despersion in toluene [38]. Examples of the described particles are reported in Figs. 2.7 and 2.8.

Several actinide precursors were used for the synthesis: UO_2 nanoparticles obtained were always nanodots with mean diameter either of $(4.5/4.6 \pm 0.6)$ nm or (10.7 ± 0.6) nm. Instead, ThO_2 nanoparticle shape and dimension were dependent on the kind of precursor used. Either nanorods (short axis: (1.08 ± 0.08) nm, long axis from 2 nm to 8 nm) or nanodots (mean diameter: (4.7 ± 1.3) nm) or branched nanocrystals (overall size of 5 nm) can be obtained [35, 38].
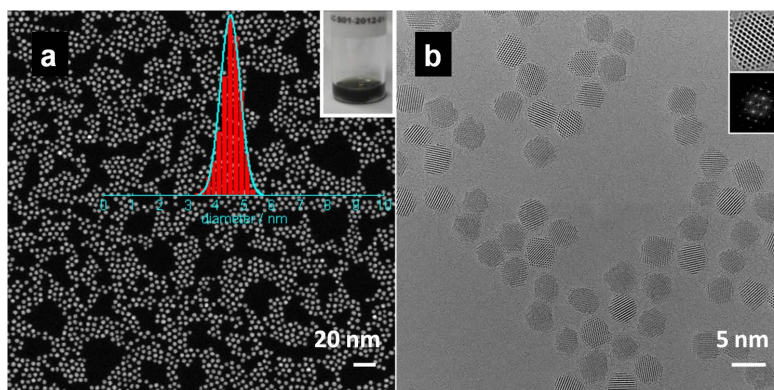
Figure 2.7: (a) HAADF-STEM image and the corresponding size histogram. (b) TEM image of UO_2 nanocrystals obtained through non-aqueous synthesis. Insets in (b) show HRTEM image and the corresponding FFT [35].

---

[1]The first one was composed of degassed mixture of dibenzyl ether (BnOBn) with different concentrations of stabilizing agents, like oleic acid (OA), that acts as capping agent to prevent agglomeration and oleylamine (OAm). In the second one, OAm was replaced by trioctylamine $\left(N\left(Oct\right)_3\right)$ and trioctylphosphine oxide $\left(OP\left(Oct\right)_3\right)$ [35].
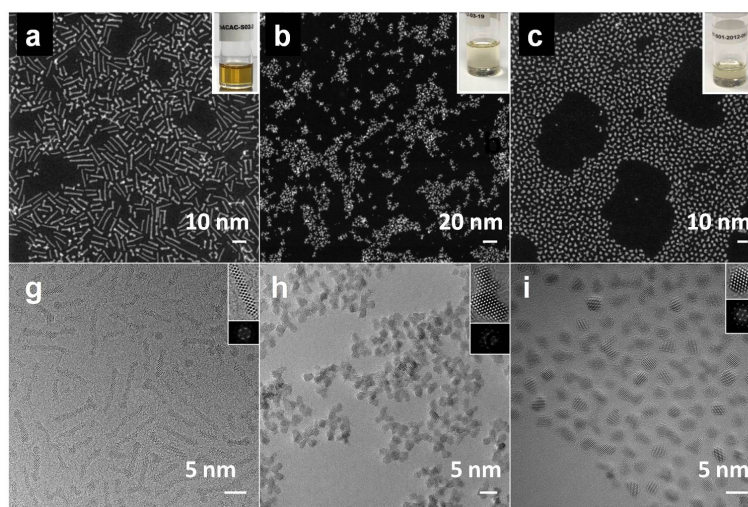
Figure 2.8: (a)-(c) HAADF-STEM images and (d)-(f) TEM images of ThO$_2$ nanocrystals obtained through non-aqueous synthesis. Insets in (d)-(f) show HRTEM image and its corresponding FFT [35].

Synthesis through precipitation in aqueous solution

This method was implemented at ITU adapting a precipitation method reported by Rousseau et al. to prepare nanometric powder of UO$_2$ [39]. Compared to the procedures employed by Rousseau, the ITU approach leads to a yield increase, obtaining up to 10 grams per batch.

All the procedures were made in a glove-box under inert atmosphere (Ar, N$_2$) as a protection for the handling of toxic materials. A six-necked reactor was used where pH-electrode, reference electrode, counter electrode, working electrode, Ar-flow inlet tube, NaOH dosing tube and out-gas neck were placed. The apparatus is shown in Fig. 2.9. The starting solution was composed of UO$_2$(NO$_3$)$_2$. After the reduction of uranium from U(VI) to U(IV), it was precipitated by adding NaOH. During the electrochemical reduction, the pH was kept below 1 using HCl to avoid hydrolysis of the U^{+4} cation.

After reduction of the solution, that had dark-green colour but had no turbidity, precipitation was induced under an N$_2$ atmosphere with an oxygen content less than 0.5%. As soon as the UO$_2$ nanocrystals started to precipitate, the solution became turbid and black. Centrifugation of the blackened solution was then performed to collect the precipitates. Sonication and repeated washing with deionised water was performed to wash out ionic species Na$^+$ and Cl$^-$ [40].

The morphology and structure of the obtained nc-UO$_2$ were characterized by means of Transmission Electron Microscope (TEM) and confirmed by XRD [41].
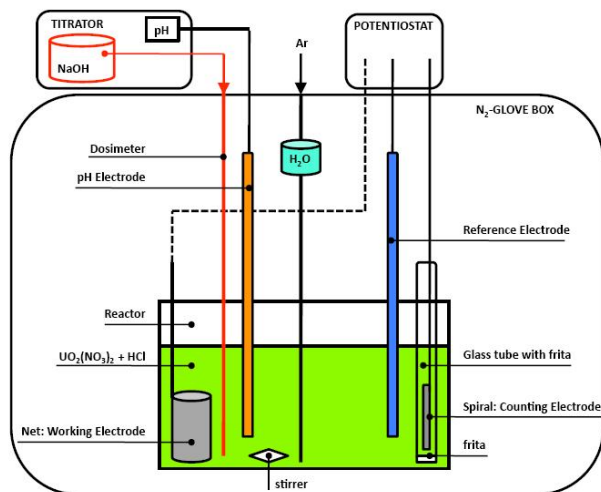
Figure 2.9: General set-up for aqueous synthesis of UO$_2$ nanocrystals.

2.3   Sample preparation for laser heating

2.3.1   UO$_2$

In the present study, only UO$_2$ produced through aqueous approach was used. Since XRD diffractograms showed that samples were already oxidised beyond O/M = 2 just after the synthesis [41], it was necessary to perform a heat treatment in reducing atmosphere (Ar/H$_2$) at 900 K for a few hours before pressing the powder to form pellets: 6 cold-pressed pellets (see Fig. 2.10) were obtained starting from this material, and were then used to perform the melting point analysis. The pellets had a weight between 300 mg and 425 mg. The heat treatment caused grain growth, as measured in this work (see subsection 4.1.1 in Chapter 4).

Melting point depression study on UO$_2$ nanoparticles produced through the non-aqueous approach is ongoing.

Figure 2.10: UO$_2$ nanocrystalline pellets.

2.3.2   ThO$_2$

Some experiments were performed without success on the particles "as-produced" (see subsection 4.2.3 in Chapter 4). As a consequence, preliminary heat-treatments either at 600 K or at 700 K under air were performed to reduce the amount of ligand, but trying to avoid excessive grain growth. The sample named S05 was heat-treated at 600 K, instead S07, S08 and S10 were heat-treated at 700 K. The powder was then pressed using a hydraulic press, obtaining 4 pellets of 3 mm of diameter and a few mm of thickness, depending on the amount of material available. The mass of the pellets was between 10 mg and 23 mg. An example is given in Fig. 2.11.
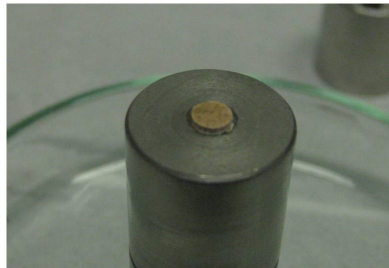
Figure 2.11: Pressed pellet of nanocrystalline ThO$_2$ powder after heat treatment in air at 600 K.

References

[1] N.E. Todreas and M.S. Kazimi. *Nuclear Systems I.* Taylor Francis, (1993).

[2] D.R. Olander. *Fundamental Aspects of Nuclear Reactor Fuel Elements.* Technical Information Center, Office of Public Affairs Energy Research and Development Administration, (1976).

[3] J.K. Fink. *J. Nucl. Mater.*, 279:1, (2000).

[4] C. Guéneau, N. Dupin, B. Sundman, C. Martial, J.-C. Dumas, S. Gossé, S. Chatain, F. De Bruycker, D. Manara, and R.J.M. Konings. *J. Nucl. Mater.*, 419:145, (2011).

[5] C. Guéneau, M. Baichi, D. Labroche, C. Chatillon, and B. Sundman. *J. Nucl. Mater.*, 304:161, (2005).

[6] D. Labroche, O. Dugne, and C. Chatillon. *J. Nucl. Mater.*, 312:21, (2003).

[7] M. Baichi, C. Chatillon, G. Ducros, and K. Froment. *J. Nucl. Mater.*, 349:17, (2006).

[8] D. Manara, C. Ronchi, M. Sheindlin, M. Lewis, and M. Brykin. *J. Nucl. Mater.*, 342:148, (2005).

[9] J.L. Bates. *J. Am. Ceram. Soc.*, 49:395, (1966).

[10] J.A. Christensen. Stoichiometry effects in oxide nuclear fuels. Technical report, Battelle Northwest (USA) Laboratory Report 536, 1967.

[11] W.L. Lyon and W.E. Baily. *J. Nucl. Mater.*, 22:332, (1967).

[12] M.J. Bannister. *J. Nucl. Mater.*, 24:340, (1967).

[13] R.E. Latta and R.E. Fryxell. *J. Nucl. Mater.*, 35:195, (1970).

[14] T.Tachibana, T. Ohmori, S. Yamananouchi, and T. Itaki. *J. Nucl. Sci. Technol.*, 22-2:155, (1985).

[15] S. Yamananouchi, T.Tachibana, K. Tsukui, and M. Oguma. *J. Nucl. Sci. Technol.*, 25-6:528, (1988).

[16] Transport of consumer goods containing small quantities of radioactive materials. final report. contract number: 4.1020/d/99-006 (dg tren), (2001).

[17] P. Patnaik. *Handbook of Inorganic Chemical Compounds.* McGraw-Hill, (2003).

[18] J.R. Lamarsh. *Introduction to Nuclear Reactor Theory.* Addison-Wesley Publishing Company, (1966).

[19] C. Lombardi, L. Luzzi, E. Padovani, and F. Vettraino. *Prog. In Nucl. Energy*, 50:944, (2008).

[20] J. Belle and R.M. Berman. Thorium oxide: properties and nuclear applications. Technical report, Naval Reactors Office. United States Department of Energy, (1984).

[21] IAEA-TECDOC-1450. Thorium fuel cycle â potential benefits and challenges, (2005).

[22] C. Hellwig, M. Streit, P. Blair, T. Tverberg, F.C. Klaasen, R.P.C. Schram, F. Vettraino, and T. Yamashita. *J. Nucl. Mater.*, 352:291, (2006).

[23] L. Capriotti and A. Quaini. High temperature behaviour of nuclear materials by laser heating and fast pyrometry. Master's thesis, Politecnico di Milano, (2011).

[24] C. Ronchi and J.P. Hiernaut. *J. Alloy Comp.*, 240:179, (1996).

[25] R. Benz. *J. Nucl. Mater.*, 29:43, (1969).

[26] H. Kinoshita, D. Setoyama, Y. Saito, M. Hirota, K. Kurosakiand M. Uno, and S. Yamanaka. *J. Chem. Therm.*, 35:719, (2003).

[27] W.A. Lambertson, M.H. Mueller, and F.H. Gunzel Jr. *J. Am. Ceram. Soc.*, 36:397, (1953).

[28] G. Guozhang. *Nanostructures & nanomaterials : synthesis, properties & applications.* London : Imperial College Press, second edition edition, (2011).

[29] C.L. Haynes and R.P. Van Duyne. *J. Phys. Chem. B*, 105:5599, (2001).

[30] M. Niederberger and N. Pinna. *Metal oxide nanoparticles in organic solvents.* Springer, first edition, (2009).

[31] S. Gu Kwon and T. Hyeon. *Small*, 7:2685, (2011).

[32] C. Burda, P.E. Wagner, R. Narayanan, and M. A. El-Sayed. *Chemical Reviews*, 105:1025, (2005).

[33] D.R. Askeland. *The Science and Engineering of Materials.* Chapman & Hall, third s.i. edition edition, (1996).

[34] R. Strey, X. Chen, and Y. Viisanen. *J. Phys. Chem*, 98:7748, (1994).

[35] D. Hudry, C. Apostolidis, O. Walter, T. Gouder, E. Courtois, C. Kübel, and D. Meyer. *Chem. Eur. J.*, 19:5297, (2013).

[36] A.S. Myerson. *Handbook of Industrial Crystallization.* Butterworth-Heinemann, second edition, (2002).

[37] J. Park, K. An, Y. Hwang, J.G. Park, H.J. Noh, J.Y. Kim, J.H. Park, N.M. Hwang, and T. Hyeon. *Nature Materials*, 3:891, (2004).

[38] D. Hudry, C. Apostolidis, O. Walter, T. Gouder, E. Courtois, C. Kübel, and D. Meyer. *Chem. Eur. J.*, 18:8283, (2012).

[39] G. Rousseau, M. Fattahi, B. Grambow, L. Desgranges, F. Boucher, G. Ouvrard, N. Millot, and J.C. Nièpce. *J. Solid State Chem.*, 182:2591, (2009).

[40] R. Jovani-Abril. *Synthesis of nanoparticles: processing and properties of nanocrystalline-ceramics.* PhD thesis to be submitted to the Universidad de Santiago de Compostela.

[41] R. Jovani-Abril, R. Eloirdi, D. Bouexière, R. Malmbeck, and J. Spino. *J. Mater. Sci.*, 46:7247, (2011).

Chapter 3

Experimental set-up and material characterization

In this Chapter, a general overview of experimental techniques used for the study of the melting point depression of nanoparticles is given. Then, the experimental set-up used for melting experiments and the techniques employed in this work for the characterization of the samples are introduced.

Up to the 1980s, experimental investigations of the size effect on melting was performed in a large variety of elements and compounds with relatively low melting temperature. First evidence of melting point depression was given by Takagi in 1954 using electron diffraction (ED) [1]: the melting causes disordering of the structure that is detected through changes in the diffraction pattern. The ED method has then been frequently applied to study this phenomenon after Takagi [2–4]. In particular, Buffat and Borel found that melting temperature of Au is 300 K for 20 Å nanoparticles compared to the melting temperature of bulk Au, which is 1336 K [5]. Also *in-situ* electron microscopy has been extensively used [6], even in the dark field mode [7].
More recently, even *in-situ* high temperature XRD diffraction [8,9] has been used. New techniques have been implemented, such as nanocalorimetry with fast differential scanning calorimetry (DSC). Lai et al. were the first to apply such an effective method to study the melting behaviour of Sn nanoparticles [10]. Further details about this new technique and its application to thermodynamics of nanoparticles can be found in Appendix B.
Schierning et al. have carried out TEM investigation and differential thermal analysis (DTA) on SiO_2 showing surprising melting point depression [11].

3.1 Laser heating

All the described methods are not suitable for measuring the melting point of refractory ceramic materials, whose solid-liquid transition occurs at more than 2500 K. The present work constitutes a first attempt to observe the melting behaviour of such materials.

The experimental approach adopted here is fast laser heating, an innovative technique implemented at ITU [12].

The set-up is composed of a Nd:YAG laser (1064 nm wavelength and maximum power of 4.5 kW) for heating up the specimen in the sub-second (ms) time regime. It is coupled with multi-wavelength pyrometry, that is the most suitable technique to record the surface temperature of the heated specimen because of the high temperatures and high heating/cooling rates involved, often exceeding 3000 K and 100000 K/s, respectively. The possibility to heat the sample very quickly is crucial to minimise particle agglomeration before melting. Fig. 3.1 shows an overview of the general set-up.
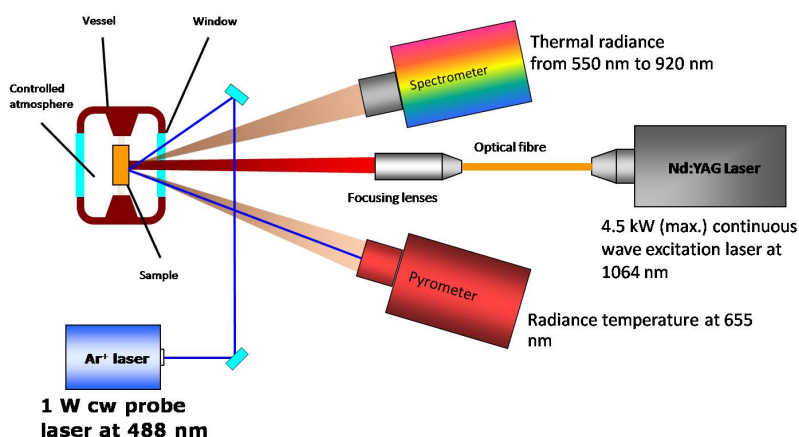
Figure 3.1: Laser heating technique, experimental set-up.

The thermal analysis is based on a thermal arrest method, in which the temperature of the phase transition is detected by recording the change in the cooling/heating rate of the sample due to the release/absorption respectively of the latent heat of transition at a given sample composition. More background on the method employed is reported in Appendix A.

It has already been employed for the investigation of freezing point of nuclear fuels (UO_2, PuO_2, ThO_2, mixed oxides of uranium-plutonium and uranium-thorium) [13–15], other actinide oxide (NpO_2) [16], uranium carbides (UC, UC_2) [17], zirconium carbides (Zr-C) [18].

Nevertheless, the approach used so far cannot be employed for nanoparticles. The detection of freezing point, in fact, does not provide any information about possible melting point depression: referring to Fig. 1.1, when the process of solidification starts, the formation of bulk solid happens, as it is the most stable phase. The freezing point would thus be the transition temperature between "bulk" phases (solid and liquid).

To detect how much the melting bahaviour is affected by the particle size, phase change must be recorded during the heating stage. However, as is often the case in rapid laser-heating experiments, melting is hardly observable during heating directly from the thermogram [19].

If we consider energy balance on the sample of mass m and specific heat at constant

pressure c_p, we have:

$$mc_p\frac{dT_\lambda}{dt} = Q_{laser} - Q_{losses} - Q_{phase} \tag{3.1}$$

In eq. (3.1), Q_{laser} is the power coming from the laser, Q_{losses} is a term that summarizes all the losses and heat exchange with environment, and Q_{phase} is the power involved in melting transition (melting enthalpy).

Assuming that losses can be considered constant and quite small (i.e., relatively slow heat diffusion from the heated surface into the bulk of the sample, small heat transfer with surrounding gas), power coming from the laser is orders of magnitude greater than the power involved in the phase transition, since only a thin surface layer is quickly driven through the melting transition, with only little associated latent heat of fusion. As a consequence, the contribution coming from the latter is overcome by the first [20].

Furthermore, the slope of the ascending part of the thermogram is much affected by changes in some optical properties such as emissivity [21].

The problem is tackled by using a visual approach through the use of a supplementary device, a low-power (1 W) probe Ar^+ blue laser. This laser beam impinges on the sample surface and the reflected beam (RLS) is recorded in the second channel of the pyrometer used to record radiance temperature of the sample. When the liquid starts to form, the surface vibrates under capillarity forces and causes reflectivity changes and interference (further details are given in next subsection). The onset of laser signal vibrations can thus be used to determine melting onset [12].

In Fig. 3.2, a typical example of application of the described technique is presented. The thermogram (black line) is the temperature vs. time curve of a μm-sized stoichiometric uranium dioxide sample laser heated; the green line represents the laser power profile, whereas the blue one is the reflected signal of the probe blue laser and the red one its first derivative. Some stages in the reflected signal (blue) can be identified [22]:

(1) the reflected light signal is stable, because no melting is reached;

(2) onset of small vibrations when the sample sample surface reaches the melting temperature: a thin liquid layer starts to move under capillarity forces;

(3) light scattering increases correspondingly to the increase of amount of liquid formed;

(4) laser power is switched off: a fast drop both in the temperature and in the laser signal follows.

(5) upon solidification, vibrations fade due to the advancing solid front. Correspondingly, the freezing plateau after undercooling of the liquid phase appears.

(6) after complete solidification, the signal sets on a new constant value determined by changed reflectivity of the surface.

The second stage is the one that sets the melting temperature, thus the most important in this research. It was not always possible to identify these stages during nanoparticle

melting, due to many experimental difficulties which will be further explained in Chapter 4, but in many experiments the same features were observed.
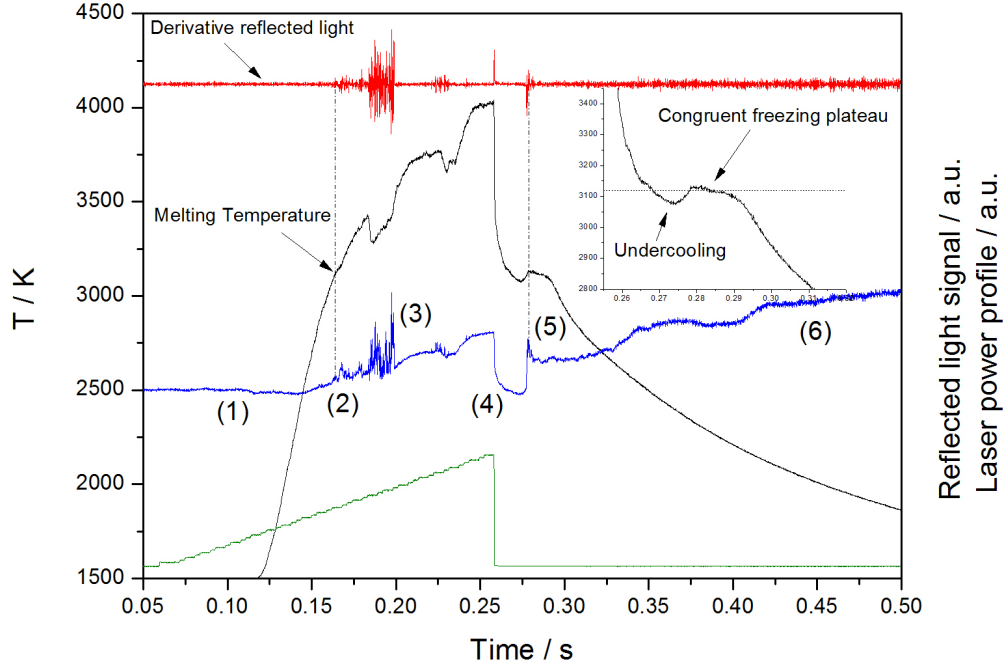
Figure 3.2: Melting point measurement on stoichiometric uranium dioxide. Vertical lines across the reflected light signal (blue) set melting and freezing temperatures, respectively.

A first issue of the experimental work was the finding of good power profiles. Unlike commercial nuclear fuels, the nc-samples were not sintered, so they were less resistant to thermal shocks caused during fast melting experiments. On the other hand, subsecond melting was necessary to avoid excessive particle agglomeration before melting. Several tests were performed using different heating rates and laser power combinations. For nc-UO_2 a couple of preliminary experiments using a ramp of 500 ms with maximum power of 1035 W were done. Then, a ramp of 200 ms with the same maximum power was used, to decrease probability of pre-melting grain growth.

To determine a good power profile for melting nc-ThO_2 pressed powder, dummy µm-sized ThO_2 powder was pressed with the same press used for nanostructured samples (see subsection 2.3.2) and tests were made on it. The power profiles used were a combination of ramp and pulse of two types:

1. 200 ms ramp + 100 ms pulse. Maximum power of 990 W;

2. 300 ms ramp + 50 ms pulse. Maximum power of 1035 W.

3.1.1   Laser speckle

Laser speckles are the result of multiple interference of wavelets when a nonhomogeneous object[1] is illuminated by a coherent laser beam. The scattered light is seen to consist of a random collection of alternately bright and dark spots (speckles) [23], as in Fig. 3.3.
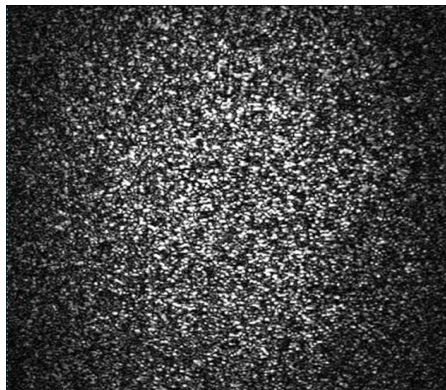
Figure 3.3: Speckle pattern.

If we consider free-space propagation, the resulting optical wave at an observation point distant from scattering surface consists of many wavelets, each arising from a different microscopic element of the surface. Due to roughness, the distances travelled by each component can differ by many wavelengths. The phase shift leads to constructive/destructive interference, resulting in a granular pattern. When the reflected beam passes through an optical system, also diffraction effects contribute, but the result is similar.

The specklegram can be correlated to the structure of the surface. Thus, in principle, any variation (for instance a displacement in the surface or vibrations or the formation of a new phase) in the illuminated surface can be inferred observing time-variation in the speckle pattern, in the limit of sensitivity (for further details, see [24]).

In our case, the pyrometer focuses on a small point (with a radius of ≈ 0.5 mm) of the surface illuminated by the blue laser. No speckle pattern from the entire scattered beam is recorded, but only interference pattern of wavelets restricted to the pyrometer focusing spot. The appearance and disappearance of liquid or defects on that surface spot will therefore change the recorded interference pattern (see stage (2) in Fig. 3.2). Such effect can be used to detect the onset of melting.

Unfortunately, especially when the amount of liquid formed was very little, the small change in the reflected beam was under the detection limit. Moreover, wavelets coming from adjacent points can occasionally reach the pyrometer, adding additional "noise" to the measurement. Nonetheless, in most cases the approach was successful.

---

[1]Surfaces of most materials are extremely rough on the scale of an optical wavelenght.

3.1.2 Specimen holder

The route to obtain the two kinds of material under study was different (see subsection 2.2.2) and only urania nanocrystals could be obtained in sufficient amount to form tough pellets. Nanocrystalline UO_2 pellets were mounted inside a graphite holder with four screws, and put in the autoclave under controlled atmosphere (Fig. 3.4(a)).

For ThO_2 nanoparticles, the same approach could not be used. In fact, samples were available only in powder form, which was then pressed in an hydraulic press. Pellets obtained were too small and fragile to be fixed with the screws directly. Thus, pellets were put in holes drilled in disks of different materials which were then mounted in the autoclave. At the beginning, an allumina disk was used. Although it has a lower melting point (2323 K) compared to thoria, the material is transparent to the Nd:YAG laser wavelength, thus it does not absorb energy coming from the laser easily. Several tests were made on the support using the same power profiles employed for experiments, but no melting was seen. However, after the sample had been mounted in the support and melted, post-melting Raman spectroscopy showed the formation of an Al_2O_3-ThO_2 solid solution. The presence of an eutectic could not be excluded, so the material was considered not suitable for reliable investigation of nc-ThO_2 melting point.

Another material tested was boron nitride, which showed a freezing temperature at 2230 K. Since reaction and formation of eutectics with thoria nanoparticles at high temperatures could not be excluded also in this case, in the end the final choice was semi-disks of bulk ThO_2. Bulk ThO_2 was expected to have higher melting point (or at least equal to) than nanoparticles, therefore there was very little risk of melting the holder. This minimised also the possibility of chemical reactions with the sample. In fact, ThO_2 supports were not melted in the current laser shots. On the other hand, the sample holder was quite fragile and often was cracked or broken following the laser irradiation.

In this research, optics producing both a 3 mm-diameter laser spot and 5 mm-diameter laser spot on the specimen were used, the laser power density ($W\,cm^{-2}$) being a critical parameter.

3.1.3 Autoclave

The pressure device used in this work (up to 2.5 bar) is shown in Fig. 3.4(b). The specimen and the holder are put inside a cylindrical vessel, which has two windows, one made of sapphire and the other of fused silica. The autoclave is connected with a vacuum/gas system. Experiments were performed under different kind of gases: for ThO_2 air was used, instead for UO_2 Ar/H_2 was used to control oxidation of the sample.

Every time, a few cycles of vacuum and refilling with gas were made, in order to purge the system. The vessel was then filled with 2.5 bar of gas, to limit out-of-equilibrium massive evaporation during melting [12].

<div align="center">(a)   (b)</div>
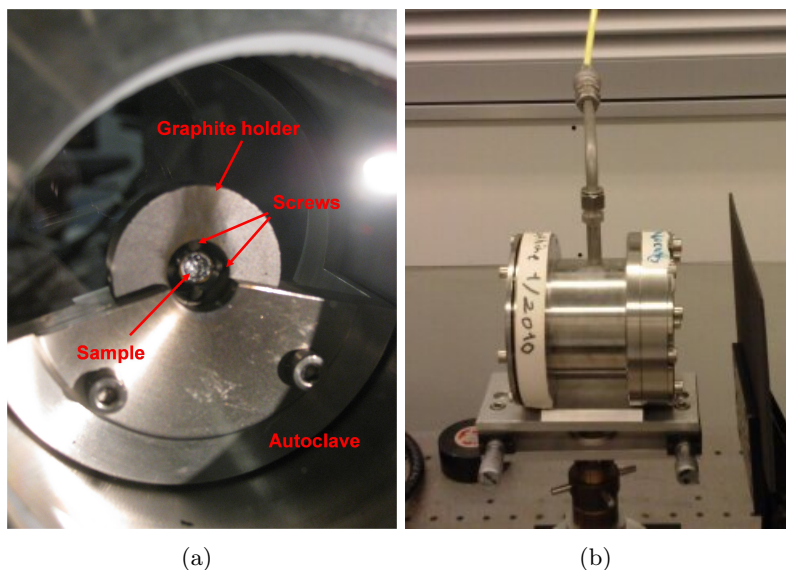
Figure 3.4: (a) Sample holder. (b) Autoclave.

3.2 Fast two-channel pyrometer

Before starting the description of the characteristics of the pyrometer used, a brief digression about Planck's radiance and definition of emissivity must be done.

3.2.1 Background on thermal radiation

Planck's radiation law sets the relationship between the spectral radiance emitted by a blackbody and its temperature:

$$L_{\lambda,b}(\lambda, T) = \frac{c_1}{n^2 \lambda^5} \left[exp\left(\frac{c_2}{n\lambda T} \right) - 1 \right]^{-1} \tag{3.2}$$

In eq. (3.2), $L_{\lambda,b}$ is the spectral radiance at the wavelength λ, T is the blackbody absolute temperature, n is the refraction index of the medium[2]. The two constants are $c_1 = 2\,h\,c_0{}^2$ and $c_2 = h\,c_0\,k_B{}^{-1}$ where c_0 is the speed of light in vacuum, h is Planck's constant, k_B is Boltzmann constant.

In case $n\,\lambda\,T << c_2$, it is possible to obtain Wien's approximation:

$$L_{\lambda,b}(\lambda, T) = \frac{c_1}{n^2 \lambda^5} \left[exp\left(\frac{c_2}{n\lambda T} \right) - 1 \right]^{-1} \approx \frac{c_1}{n^2 \lambda^5} \left[exp\left(\frac{c_2}{n\lambda T} \right) \right]^{-1} \tag{3.3}$$

This expression is accurate for short wavelengths and for low temperatures and is better than 1 % if $n\,\lambda\,T \leq 3100$ µmK, as can be calculated from eq. (3.2) and eq. (3.3).

---

[2]n is mostly close to 1 in the current experimental conditions.

Another important concept is the one of emissivity. The ratio of radiation emitted by the real surface to the radiation emitted by an ideal blackbody is defined as emissivity.

Considering a real surface (rs) and a blackbody (b) at the same temperature, they have different spectral radiance because the former has an emittance[3] less than one and they are related by:

$$L_{\lambda,rs}(\lambda,\theta,\phi,T) = \epsilon(\lambda,\theta,\phi,T)L_{\lambda,b}(\lambda,T) \tag{3.4}$$

Therefore, the concept of spectral radiance temperature T_λ is introduced. It is the temperature of a blackbody emitting the same spectral radiance at a given wavelength as the real surface:

$$L_{\lambda,rs}(\lambda,T_\lambda) = \frac{c_1}{n^2\lambda^5}\left[exp\left(\frac{c_2}{n\lambda T_\lambda}\right) - 1\right]^{-1} \tag{3.5}$$

In the spectral region where Wien's approximation is valid, comparing the latter definition with eq. (3.4) and Planck's equation it is easy to obtain an expression that links the real temperature and the spectral radiance temperature:

$$\frac{1}{T} = \frac{1}{T_\lambda} + \frac{n\lambda}{c_2}\ln\epsilon(\lambda,\theta,\phi,T) \tag{3.6}$$

Equation (3.6) was used to determine emittance (see section 3.4).

3.2.2 The pyrometer principle of operation

A simplified functional block diagram of the fast pyrometer is shown in Fig. 3.5.
The objective (2) collects thermal radiation from the 0.5 mm radius spot of the target (1) (at a nominal working distance of 400 mm) and focuses it on the mirror (4) with a pinhole which acts as the field stop of the system. After that, the light passes through the fiber optics splitting system and then, after passing the filter (5), is focused on Si photodiodes. The photodiodes are mounted in a metallic case, which is maintained at a fixed temperature thanks to a high precision miniature thermostat with a microprocessor controller. A folding mirror (8) is used to reflect the specimen's image, which is formed at the pinhole mirror (4), into an eyepiece (3) in order to align the pyrometer on the specimen area of interest. Furthermore, the pyrometer was equipped with a notch filter to stop parasite reflections from the heating laser (see section 3.3).

---

[3]The term "emissivity" determines the characteristics of a material and it is an intrinsic property, while emittance refers to the characteristics of a target object surface. Hence, emissivity is the only one variable which helps in finding out emittance of a specific surface. There are some other factors also that determine emittance. They are:

- Shape and form of the object,
- Material oxidation,
- Surface conditions (i.e., surface polishing).

In spite of having a slight technical division between emittance and emissivity, these two terms are frequently used interchangeably.
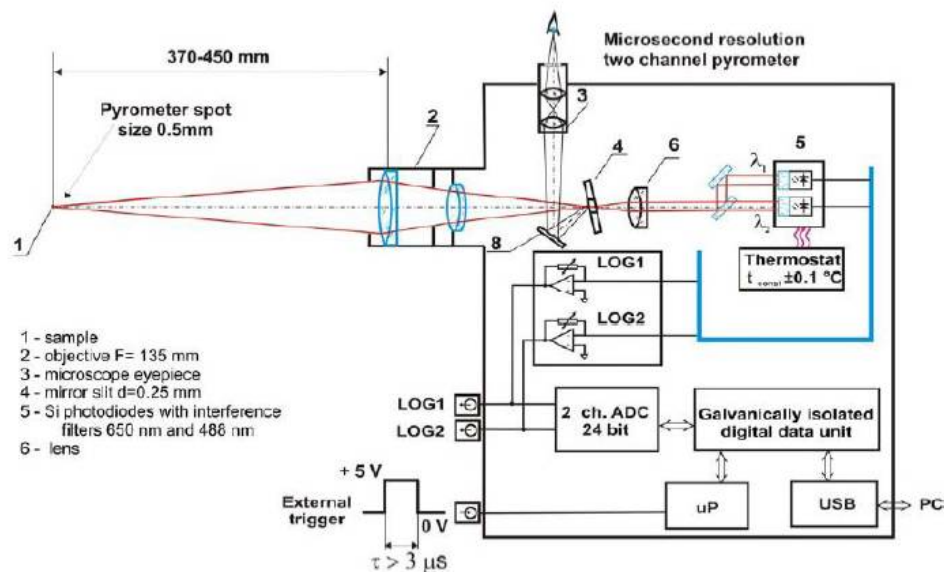
Figure 3.5: Simplified functional block diagram of the pyrometer.

The main technical data are summarized in Table 3.1.

Table 3.1: Technical data of the two-channel pyrometer.

Operational temperature range	1750-6000
Settling time of 1 % of log outputs, μs	10
Number of brightness temperature channel	2
Distance to the target, mm	370-450
Working wavelengths, λ, μm 1st channel 2nd channel	0.655 0.488
Bandwidth, $\Delta\lambda$, μm 1st channel 2nd channel	0.027 0.007
Spot size at working distance 400 mm, mm	0.5
Power consumption, W	15

The current signals from the photodiodes are converted in voltage signals by the log-arithmic amplifiers (LOG1, LOG2). Then, a Nicolet Pro® 44C digital oscilloscope receives these voltage output signals. The output signal from the 655 nm-channel may be expressed, in the range of linear response of the pyrometer, as follows:

$$V_{out}(T) = k_{log} \log \left[\frac{i_{ref}}{i_p(T)} \right] \tag{3.7}$$

39

where $k_{log} = 0.375$ V is the scaling constant of the logarithmic amplifier and i_{ref} is an internal reference current of the amplifier integrated circuit. The output is sent to a PC and recorded using LabView® software.

3.2.3 The pyrometer calibration

The pyrometer's 655 nm-channel calibration was made following the same protocol already employed during previous calibrations [21].

Two tungsten ribbon lamps were used. A Polaron® 22/G argon filled lamp was used in the temperature range 1800-2500 K, whereas a Polaron® 22/V lamp was used for the temperature range 1100-1800 K. An accurate calibration was done for both the lamps to obtain a radiance temperature curve at 655 nm vs. input current by the PTB (Physikalisch-Technische Bundesanstalt) in Berlin in 2010. The pyrometer and the lamps were set up on an optical table. The experimental setup is shown in Fig. 3.6.
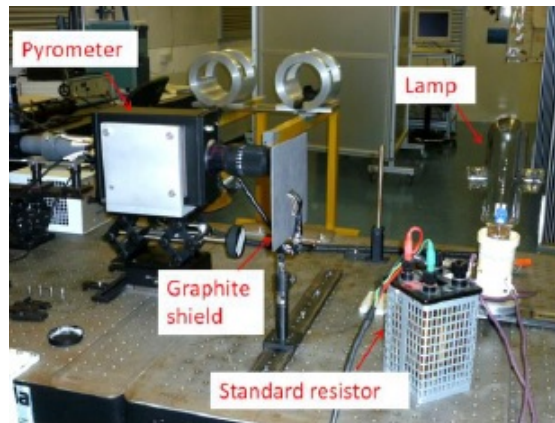
Figure 3.6: Pyrometer calibration: experimental set-up.

The calibration was carried out according to the International Organization of Legal Metrology (OIML) recommendation [25].
As first step, the lamps were set vertically. Then the centre of the W-filament was aligned with the lens of the pyrometer every time the temperature was set to a new value, because of the filament thermal expansion. A sighting pin inside the lamp indicates the centre of the filament and the correct position for the calibration. Finally, a check on the aplomb between the optical axis of the pyrometer and the ribbon was made. The black-spot image of the pyrometer field stop is visible from the telescope on the specimen surface (see (3) and (4) in Fig 3.5). It should be as sharp as possible in order to ensure the focusing of the lenses. In order to produce a stable input current in the lamps, an electric circuit was used. It was composed of:

- DC source;

- Voltmeter;

- Standard resistor $R = 1$ mΩ, in series with the lamp.

Through the measurements of the voltage drop across the standard resistor it was possible to measure the current flowing in the lamps. From this current it was possible to obtain the lamps' radiance temperature through the calibration curves from PTB [26].

When the alignment phase was concluded, the lamp was heated. To ensure proper working of the lamps and measurements reproducibility, the lamps were heated slowly, especially during the first steps. At lower temperature the current was raised with a maximum rate of 5 A/min. After reaching the desired current value, some time was needed to stabilize it. In this way, were minimized the uncertainties coming from fluctuation due to unstable current and no constant temperature reaching. Steps of current rising are summarised in Table 3.2.

Table 3.2: Current steps characteristics.

step	Current / A	T / K	Stabil. time / min
1	16.631	1800	50
2	16.633	1800.3	40
3	19.787	2000.8	20
4	23.291	2201.9	20
5	25.113	2300	20
6	25.157	2302.3	20
7	27.096	2402.8	20
8	29.109	2503.2	20

At every current step, two measurements were taken: an "off"-measurement when the pyrometer cannot see the lamp's light due to a graphite shield interposed between the lamp and the pyrometer, and an "on"-measurement without the graphite shield. The off-measurement was done to determine whether the pyrometer response was temperature-independent, and the relationship between lamp temperature and the oscilloscope voltage output signals.

The complete procedure (i.e., slow raise in current, stabilizing time, alignment, on and off measurement) must be followed after each current step for both the lamps.

A linear relationship can be derived, between the lamp's radiance temperature and the pyrometer output signal, combining eq. (3.7) with Wien's expression for the blackbody spectral radiance:

$$V_{out}(T) = A + \frac{B}{T_\lambda} \qquad (3.8)$$

This equation can be taken to obtain coefficients A and B using a linear fit on the data. Once constant B is known, it is possible to obtain the effective wavelength (λ_{eff}) of the pyrometer using the following relation:

$$B = (\log e)\, k_{log} \frac{c_2}{\lambda_{eff}} \qquad (3.9)$$
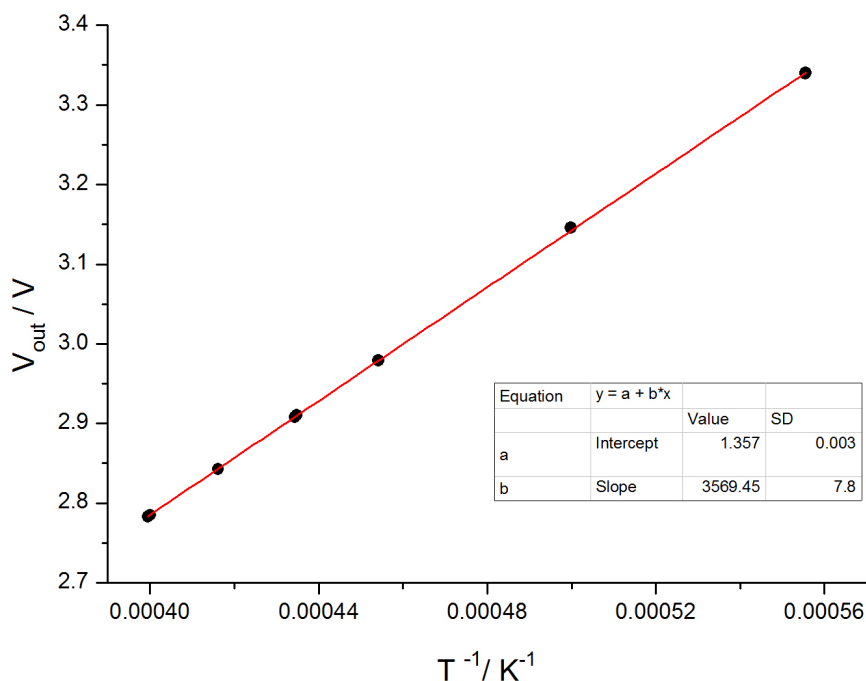
Figure 3.7: Calibration of 655 nm-pyrometer. "on" measurements.

From which the effective wavelength (λ_{eff}) is calculated:

$$\lambda_{eff} = 0.4343 \, k_{log} \frac{c_2}{B} \tag{3.10}$$

where $c_2 = 14388 \, \mu\text{m K}$. The calculated effective wavelength is 656 nm.

To give an estimation of the error introduced by the change in the measuring wavelength, the emissivity can be considered constant (grey body assumption[4]). Therefore the sole contribution to temperature error coming from wavelength is:

$$\delta T = \left| \frac{\partial T}{\partial \lambda} \delta \lambda \right| \tag{3.11}$$

From eq. (3.6) we can obtain the relative error as:

$$\frac{\delta T}{T} = \frac{n}{c_2} \ln \epsilon \, T \, \delta \lambda \tag{3.12}$$

If we assume a value for the emissivity $\epsilon = 0.8$, which is conservatively reasonable for the materials under study, the calculated error at $T = 1800$ K and $T = 2500$ K are 0.0028% and 0.0038%, respectively.

---

[4]A grey body is a body that emits radiation in constant proportion to the corresponding black-body radiation, i.e. has a constant emissivity.

In conclusion, if we consider for example the value of other source of error as in [22], the contribution of this factor is negligible.

3.3   Notch filter

The measurement of the melting point requires the use of a notch filter to prevent the pyrometer from detecting laser radiance during the heating stage of the measurement.

Notch filters, also commonly referred to as band-stop or band-rejection filters, are designed to transmit most wavelengths with little intensity loss while attenuating light within a specific wavelength range (the stop band) to a very low level.

The filter consists of several layers of glass held together with epoxy and the mounting anodized aluminum ring.

The figure of merit is the optical density or absorbance, defined as the logarithmic ratio of the radiation falling upon the filter, to the radiation transmitted through the filter as in eq. (3.13):

$$A_\lambda = \log \frac{I_0}{I_{trans}} \tag{3.13}$$

The pyrometer used was equipped with a Holographic Notch Plus Filter from Kaiser Optical Systems®.

The main technical data are reported in Table 3.3.

Table 3.3: Technical data of the notch filter.

Attenuation factor	10^{-6}
Spectral bandwidth, cm^{-1}	< 700
Spectral edgewidth, cm^{-1}	< 300
Stop wavelength, nm	1064

3.4   Multichannel pyrometer

In the present work, a 256-channel pyrometer was employed to obtain spectral emittance of the target at the wavelength measured by the two-channel pyrometer.

This multichannel pyrometer consists of an integrated array of 256 Si photodiodes recording the signal in the spectral range between 488 and 1011 nm. The photodiode array is directly mounted as a card in a personal computer (PC). The data card memory can hold 256 full spectra. Therefore, after each measurement, a data file with 256 spectra is transferred and saved on the PC. What it is recorded is a 256×256 array where the i-th row represents the i-th spectra acquired at time i times the integration time. The latter is the time needed to record a full 256 spectrum and it is adjustable depending on the quality and stability of the signal.

In order to convert the measured signal into a quantity that is directly proportional to the thermally emitted spectral radiance, the transfer function of the device is needed:

$$K(\lambda) = \frac{\tau(\lambda)}{Counts(\lambda, T_b)} \frac{1}{\lambda^5 \left[exp\left(\frac{c_2}{\lambda T_b} \right) - 1 \right]} \quad (3.14)$$

In eq. (3.14), $\tau(\lambda)$ is the window transmittance at wavelength λ, T_b is blackbody temperature and $Counts(\lambda, T_b)$ is the measured signal intensity expressed in counts. $K(\lambda)$ was determined through calibration against a standard lamp and a blackbody source, described in a previous work [21].

3.4.1 Emissivity measurements by radiance spectral analysis

In order to convert the radiance temperature into true temperature, a numerical approach has been used, based on a rearrangement of eq. (3.6):

$$\frac{1}{T_\lambda} = \frac{1}{T} - \frac{n\lambda}{c_2} \ln \epsilon \quad (3.15)$$

It is then possible to plot the experimentally measured inverse of radiance temperature as a function of the wavelength [22]. Within the greybody behaviour, the resulting graph is a straight line. When it is extrapolated to zero wavelength, it intersects the inverse true temperature. From the value of the slope, the emissivity can be obtained, as shown in Fig. 3.8. The advantage of this second approach is that eventual deviations from greybody behaviour are more easily detectable from the curve shape.

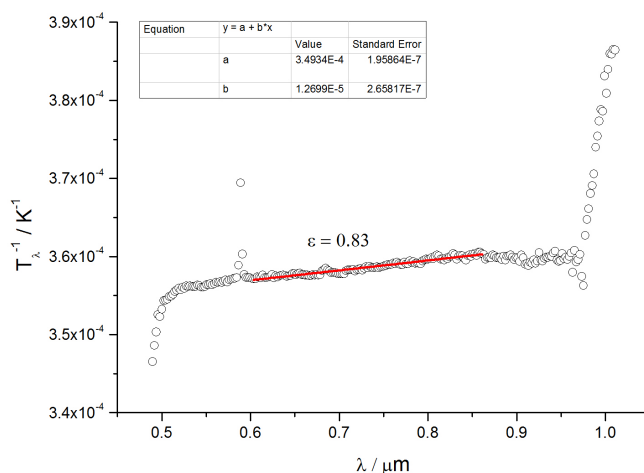
Figure 3.8: Example of NSE calculation at melting of nc-UO$_2$.

3.5 Temperature measurement uncertainty

Uncertainty of the measurements was calculated according to the error propagation law [22], taking into account the following terms:

$$\delta T = \left(\delta T_{calibration}{}^2 + \delta T_{\epsilon}{}^2 + \delta T_{RLS}{}^2 \right)^{1/2} \tag{3.16}$$

where $\delta T_{calibration}$ is the uncertainty associated to pyrometer calibration, δT_{ϵ} the one from the emissivity, and δT_{RLS} the uncertainty associated with the onset of vibrations in the RLS signal. As discussed in 3.2.3, the error due to the pyrometer's λ_{eff} is negligible.

The uncertainty of the calibration gives a contribution of 0.5% on the value of the temperature as determined in [22], whereas the contribution due to the emissivity depends on the emissivity value itself and on the temperature at which it is calculated. The relationship between $\delta\epsilon$ and δT can be obtained differentiating eq. (3.15):

$$\frac{\delta T}{T} = \frac{n\lambda\,T}{c_2}\frac{\delta\epsilon}{\epsilon} \tag{3.17}$$

where all the symbols have the same meaning as in (3.15). Using a value of $\epsilon = 0.83$ (typical of UO_2), considering an error on the emissivity of 5%, the error on the temperature is 0.54% at 2000 K and 0.81% at 3000 K. For ThO_2 the maximum error induced at the melting temperature of the bulk material is 0.91%.

It is more difficult to quantify exactly the error coming from the RLS. First of all, it depends on the experimental conditions, which determine the quality of the signal, secondly it depends on the error that the human eye makes in setting the onset of the vibrations from the recorded signal. The second can be estimated when the melting temperature is well known, as in the case of the thermogram in Fig. 3.2. The error induced is 0.01 %, much smaller compared to the other terms. However, to take into account also the first source of error is advisable to give a general contribution to the temperature uncertainty of 0.1%, to be conservative.

In case of evaluation of the solidus/liquidus temperatures on the cooling stage of a thermogram, the last term in eq. (3.16) is not added.

3.6   Material characterization

Detailed characterization of samples both before and after laser heating has been an essential part of this work. In particular, it was crucial to analyse the material grain structure and its evolution with temperature.

Many different investigation techniques were used for the purpose:

- Transmission Electron Microscopy (TEM);

- Scanning Electron Microscopy (SEM);

- X-Ray Diffraction (XRD);

- Raman Spectroscopy;

- Thermogravimetry (TG).

3.6.1   Transmission Electron Microscopy (TEM)

Characterization of nanoscale materials - their structure, composition, and chemical state - is essential for the evaluation of their physical and chemical properties. One of the most powerful methods for obtaining such information is the use of Transmission Electron Microscopy (TEM).

In this technique, an electron beam, coming from an electron gun (usually a tungsten filament or lanthanum hexaboride) and accelerated in ultra-high-vacuum through a strong potential (hundreds of kV), interacts with a thin specimen supported on a carbon-copper grid.

The use of an electron gun allows to overcome the limited image resolving power of optical microscopes, which is imposed by the wavelength of visible light (380-710 nm). In fact, two factors limit instrument resolution: one is the wavelength of the probe used (for instance photons or electrons); the other is due to imperfections of the optical system. In case the second one can be ignored, the smaller the wavelength the better the resolution.

According to the de Broglie relation, the electron wavelength λ_e is:

$$\lambda_e = \frac{h}{m_e v_e} \tag{3.18}$$

where h is Planck's constant, m_e is the electron mass, v_e is electron speed. The de Broglie wavelength of electrons can be arbitrarily reduced by increasing their momentum (i.e., their accelerating potential). This improves by order of magnitude the electron microscope resolving power, compared with other techniques. In fact, for a perfect optical system, the limit of resolving power is the diffraction limit. The minimum linear distance r that two objects need to have to be resolved according to the Rayleigh's criterion is:

$$r = \frac{0.61\,\lambda}{n\,\sin\theta} \tag{3.19}$$

where λ is the wavelength of the probe, $n\sin\theta$ is the numerical aperture of the microscope.

The wavelength of an electron in a TEM may be only a few picometers, but, unfortunately, the magnetic lenses used do not approach diffraction-limited performance and thus standard electron microscopes have not been able to exploit all the potential coming from the electron gun. At the state of the art, the best commercial electron microscopes can reach resolutions of better than 0.02 nm.

A TEM is composed of five main components: an electron optical column, a vacuum system, electromagnetic lenses' systems (lens supplies for focusing, deflecting and magnifying the beam), a specimen stage, the control software coupled to data recording systems. A TEM scheme is given in Fig. 3.9.

The field emission source is essential for performing high coherence lattice imaging, while the objective lenses are the heart of the machine and determine the practical limit of image resolution, as mentioned before.

When an electron impinges on the specimen, many interactions take place that provide information both about structure and chemical composition: scattering that in crystalline

samples causes diffraction contrast in the image, low secondary electron and characteristic X-ray emission, cathodoluminescence.

Diffraction patterns can be recorded to have more information about the sample structure.

In the current analysis, two different machines were used: 1) FEI Tecnai G2 STEM operating at 200 kV with a resolving power up to 5 nm equipped with a EDAX EDS-System and a Gatan Tridiem imaging filter and, occasionally, 2) Titan whose high-resolved images could reach 0.5 Å. The magnification system consists of intermediate lenses and projection lenses, and it gives a magnification up to a few millions. In both cases, the data recording system uses a charge coupled device (CCD) camera.

The instrument is very versatile and can be employed in many different configurations, according to the scope of the analysis:

- **TEM**: the beam passes through the sample and, by choosing the position of the aperture, either the unscattered electrons (bright field-TEM) or the diffracted beam (dark field-TEM) is recorded through lenses to form the image;

- **HRTEM**: is an imaging mode of the microscope in bright field configuration. Only transmitted electrons and small-angle diffracted electrons are included within the objective aperture. An image post-treatment to correct aberration is performed. It allows a contrast visualization of atomic columns, determining crystal structures and structural defect. However, this method gives only a local analysis, hence it is usually complemented with XRD analysis. The latter provides a global information about the crystallinity of the sample and mean crystallite size can be inferred (see subsection 3.6.2);

- **STEM**: it combines the principles of TEM and SEM (see subsection 3.6.3). Like SEM, by adopting the STEM technique, a fine, highly focused beam of electrons is scanned over the specimen adjusting scan coils, and the transmitted beam is directly recorded on the other side of the sample. Its primary advantage over conventional SEM imaging is the improvement of spatial resolution, which results from eliminating the electron scattering that occurs in bulk specimens as the beam electrons penetrate into the sample. In this configuration, other analyses can be coupled (for instance, when the signal is collected through a high-angle, annular dark field Z-contrast images can also be done).

All mentioned configurations were employed in the present analysis except for dark field-TEM. Diffraction pattern analyses were also performed to show structural evolution of ThO_2 nanocrystals annealed at different temperatures (see Chapter 4).

3.6.2 X-Ray Diffraction (XRD)

X-Ray Diffraction is a technique based on coherent elastic scattering of an electromagnetic beam by atoms in a crystal lattice. The wavelength of X-rays is typically on the order of
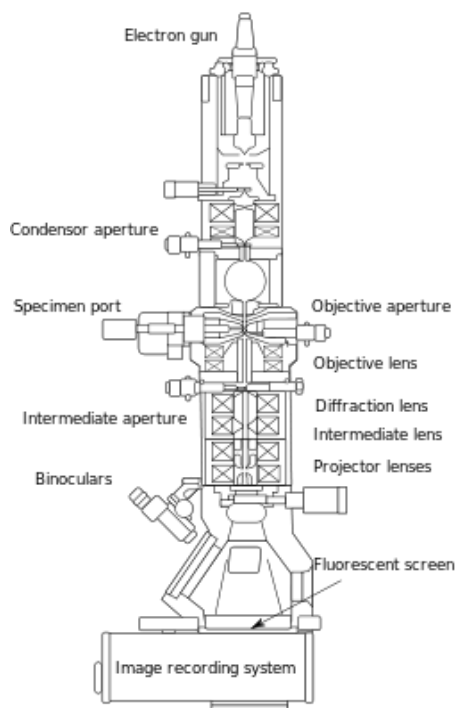
Figure 3.9: TEM scheme.

1 Å, comparable with interatomic distances in crystals, therefore this techique is suitable to obtain structural information about crystalline structures.

An electron in an alternating electromagnetic field oscillates with the same frequency as the field. When an X-ray beam hits an atom, the electrons around the atom start to oscillate with the same frequency as the incoming beam. In almost all directions, the result is destructive interference, that is, the combining waves are out of phase and there is no resultant energy leaving the solid sample. However, the atoms in a crystal are arranged in a regular pattern, and in a very few directions constructive interference can occur. The waves will be in phase and there will be well defined X-ray beams leaving the sample at various directions. Hence, a diffracted beam may be described as a beam composed of a large number of scattered rays mutually reinforcing one another [27].

Constructive interference is obtained when incident beams satisfy Bragg's law condition. As it is sketched in Fig. 3.10, only if beam phases differ for a whole number of wavelength, that is, if the path difference between the ray that gets reflected along AC' and the ray that gets transmitted, then reflected, along AB and BC satisfies the following equation:

$$(AB + BC) - AC' = n\lambda \qquad (3.20)$$

waves can renforce each other.

After some mathematical manipulation, eq. (3.20) can be written in its usual form:
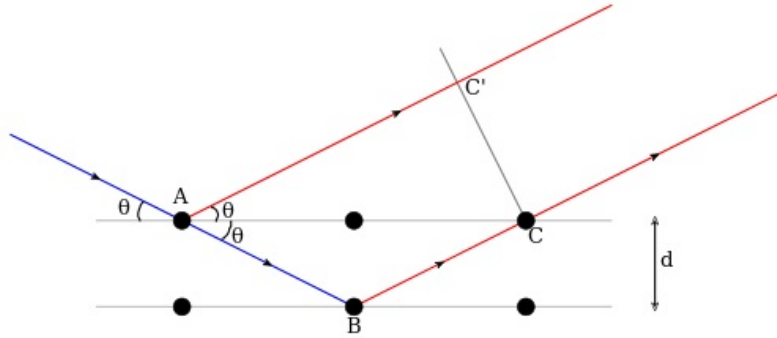
Figure 3.10: The condition for constructive interference.

$$2d \sin \theta = n\lambda \tag{3.21}$$

It is clear that the pattern of scattered X-rays (the diffraction pattern, also called diffractogram) is thus mathematically related to the structural arrangement of atoms causing the scattering.

A diffractogram is also used to estimate the mean crystallite size, according to Scherrer equation [28], which states that the peak width (B) is inversely proportional to grain dimension (D):

$$B(2\theta) = \frac{K\lambda}{D \cos \theta} \tag{3.22}$$

where K is the Scherrer's constant depending on the method used to determine peak width, the shape of the crystal, and the size distribution. It usually varies from 0.62 to 2.08.

Rietveld refinement was also implemented using open source software FullProf and Jana2006 to obtain the lattice parameter a [27].

Generally, the peaks due to smaller particles are found at slightly higher values of θ, reflecting lattice contraction [29]. This was for example the case of three metals: Au, Cu and Pt [30].

However, the interpretation of lattice contraction due to size effect is not straightforward for UO_2 nanoparticles. It is in fact known from the literature that a hyperstoichiometric oxidation state for UO_{2+x} particles leads to analogues result. The following formula, valid within the existence of a fcc solid solution, gives the expected value of lattice parameter in case of UO_{2+x}

$$a(nm) = a_0 + c\,x \tag{3.23}$$

For eq. (3.23), Perio estimated $a_0 = 0.5469$ and $c = -0.012$ [31], whereas values of 0.54705 and -0.0094, respectively, are reported in [32].

It is an open question if eq. (3.23) can be used for nanoparticles.

The machine used in this work was a Brucker D8 X-ray diffractometer mounted in a Bragg-Brentano configuration with a curved Ge monochromator and a ceramic copper tube (40 kV, 40 mA) equipped with a LinxEye position sensitive detector. The data were collected by step scanning in the angle range $10° \leq 2\theta \leq 120°$. The sample preparation for XRD analysis consisted in dispersing the powder on the surface of a silicon wafer with drops of isopropanol.

3.6.3   Scanning Electron Microscopy (SEM)

Like TEM, Scanning Electron Microscopy is based on the interaction of electrons with matter, but in this case the electron beam does not cross the specimen, but is scattered by the sample surface, providing a surface analysis only. The beam is focused onto a small spot (1 nm) and is scanned in a rectangular raster pattern on the sample surface. If the sample is not conductive, a coating with graphite is applied on it before starting the measurements.

Since it is not necessary for probe electrons to cross the sample, accelerating voltages are much lower compared to those used in TEM, typically in the range 50 V-30 kV. In our analysis a Phillips XL 40 SEM operated at 25 kV and equipped with a SAMx EDS SD-Detector has been used. A general overview of the machine is given in Fig. 3.11.
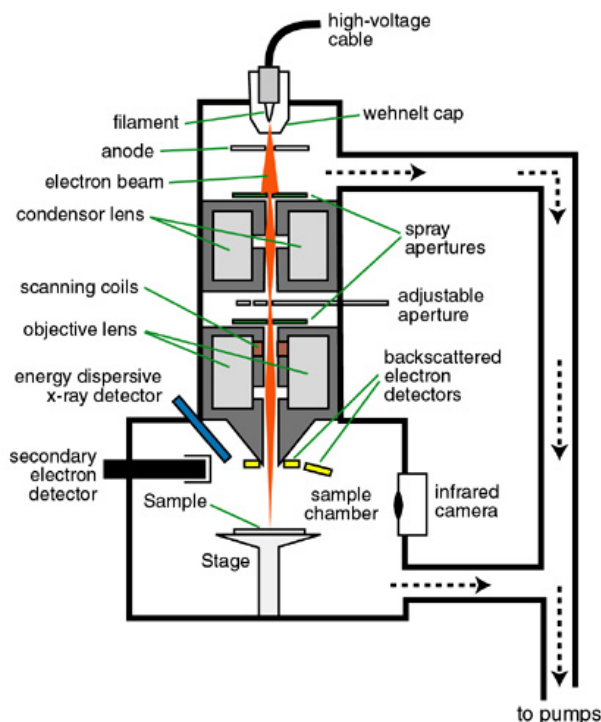

Figure 3.11: Schematic SEM.

The signal coming from back-scattered electrons (BSE) is collected using an annular

coaxial detector, which is a semiconductor or a photomultiplier. BSE images provide qualitative information on the distribution of the elements present on the surface. If an electron is back-scattered by a heavy element, it keeps most of its initial energy, so that the resulting image is brighter than that obtained when scattering occurs against a relatively light element. Thus, through a BSE image it is possible to distinguish zone richer (or poorer) of heavy elements.

The sample also emits secondary electrons (SE) as a result of inelastic scattering with the primary beam. SE have very low energy so that they can escape from the sample to be detected only if they have been produced very close to the sample surface. This gives SE images high spatial resolution and topographic contrast. Secondary electrons are deviated in the direction of a photomultiplier going through a grid biased at 400 V, in order to accelerate them.

Furthermore, characteristic X-rays emitted by the atoms present on the surface are widely used for a semi-quantitative chemical microanalysis (EDX). For light elements the approach is only qualitative, because many factors affect the signal, such as window absorption, peak overlapping and surface roughness. Instead, the analysis can be considered as semi-quantitative for heavier elements, starting from sodium.

3.6.4   Raman spectroscopy

When a photon impinges on a material sample it can be scattered elastically (Rayleigh scattering) or inelastically (Raman, Brillouin scattering), gaining (anti-Stokes) or losing (Stokes) part of its initial energy. One can view the energy lost (or gained) by the photon when interacting with the crystal as being due to the emission (or absorption) of phonons, quasi-particles representing collective vibrations occurring in crystals. The process is referred to as *Brillouin scattering* when the phonon emitted or absorbed is acoustic, and *Raman scattering* when the phonon is optical[5] [33].

If the ejected photon has more energy than the incident one, then a phonon has been annihilated, leading to the so-called anti-Stokes scattering. The de-excitation of a vibration mode (anti-Stokes) requires the vibrational state to be initially populated by phonons. The population of vibrational states follows Boltzmann distribution and thus the higher the temperature, the more populated the higher levels are. Therefore, in standard conditions (300 K), Stokes scattering is more probable as it does not require a phonon on an excited state.

If the incident and scattered photons have in the free space a momentum equal to $\vec{q}$ and $\vec{q}'$, respectively, and their corresponding angular frequencies are ω and ω', then the conservation law for energy and crystal momentum for a process involving one phonon requires:

---

[5]Acoustic phonons are related to in-phase vibrations of atoms in the crystal lattice, whereas optical phonons refer to out-of-phase vibrations.

$$\hbar\omega^{'} = \hbar\omega \pm \hbar\omega_s(\vec{k}) \tag{3.24}$$

$$\hbar n\vec{q'} = \hbar n\vec{q} \pm \hbar\vec{k} \tag{3.25}$$

where $\vec{k}$ is the phonon wave vector, $\omega_s(\vec{k})$ is the phonon angular frequency, and n is the refractive index of the material in which the photon propagates.

For photons in the visible spectrum, the associated wavelength is in the range $10^{-5} - 10^{-4}$ cm that implies a wave vector in the range $10^4 - 10^5$ cm^{-1} [6]. According to eqs. (3.24) and (3.25), the maximum value of the wave vector of the phonon involved in the scattering process occurs in case of backscattering, when it is equal to two times the value of the wave vector of the incident photon. Nevertheless, compared to the Brillouin zone dimension (of order 10^8 cm^{-1}), this value is very small, thus only phonons at the centre of the first Brillouin zone ($\vec{k} \cong 0$) can be seen by Raman spectroscopy.

Nevertheless, this selection rule is no longer valid if nanoparticles are considered [34]. As a consequence of the indetermination principle, the uncertainty of particle momentum is inversely proportional to the uncertainty in the determination of particle position [35], as expressed by:

$$\Delta q \geq \frac{\hbar}{2\Delta x} \tag{3.26}$$

The indetermination Δx of phonon position can not exceed the size of the grain. The consequence is an appreciable increased indetermination of phonon momentum in nanoscopic crystallites. This implies that not only phonons at the centre of the Brillouin zone contributes to the Raman spectrum, but also phonons with a non-zero momentum. The uncertainty in the momentum is related to a broadening of the wavenumbers of the phonons involved in Raman scattering through phonon dispersion relations. Thus, the resulting Raman peak is the convolution of signals coming from different phonons with different wavenumbers, not only from phonons with $\vec{q} \approx 0$. A shift and a broadening of the peaks of Raman spectra are seen as a consequence [34, 36–38].

Both width at half maximum (FWHM) and peak position can be correlated to inverse of grain dimension [39]. Raman spectroscopy can therefore become a probe to access information of local particle dimension range in nanocrystalline materials. Further analytical details can be found in Appendix C.

From an experimental point of view, the Raman signal is measured through a Raman spectrometer which is a device able to measure the intensity of the scattered radiation as a function of its frequency. A light source, usually a laser, is used to illuminate the sample and "excite" or "annihilate" molecular vibrations.

Raman spectra were measured at ITU with a JobinYvon® T64000 spectrometer (Fig. 3.12) used in the single spectrograph configuration[7]. The excitation source can be either

---

[6]In spectroscopy, the energy of the outcoming photons is normally expressed in terms of wavenumber $\omega = \nu/2\pi c$, which is expressed in cm^{-1}.

[7]Tests performed with the triple-additive configuration gave no significant results.

an Ar^+ Coherent® cw laser radiating at 514 nm and 488 nm, or a Kr^+ Coherent® cw laser radiating at 647 nm and 752 nm. Both lasers have a controllable nominal power between 10 mW and 1 W at the exit of the cavity. In this work, all spectra were recorded using a laser nominal power between 50 mW and 70mW. The power impinging on the sample surface is lower by a factor 10, approximately. Spectra were measured in a confocal microscope with a 50x magnification and long focal distance (≈ 1 cm). This feature allows obtaining a good signal noise ratio independent of the surface shape, with a spatial resolution of 2 μm x 2 μm on the sample surface. The spectrograph angle is calibrated with the T_{2g} excitation of a silicon single crystal, set at 520.5 cm^{-1} [40].

**Figure 3.12: Jobin-Yvon® T64000 spectrometer.**

3.6.5 Thermogravimetry (TG)

A thermogravimetric (TG) analysis consists in heating the sample under fixed atmosphere conditions and simultaneously measuring its mass. The measurements were performed by using a NETZSCH Simultaneous Thermal Analysis Apparatus STA 409. A small amount of material, usually about 50 mg, is put in the thermobalance allumina crucible. The crucible is mounted in an oven, where a certain gas flow (in this case air or Ar/H_2) and a raising ramp of temperature are set, and it is connected to a high-sensitivity analytical balance that allows *in-situ* weighing of the sample during the oxidation/reduction process. From the weight difference between initial and final powder one can calculate the initial composition, assuming that all the weight change is only due to a variation in the oxygen moles contained in the sample.

In this particular study, thermogravimetry analyses were carried out on UO_2 samples to determine oxidation state before or, when possible, after melting.
Uranium dioxide was treated in air to obtain the stable oxide U_3O_8 according to the reaction:

$$6UO_{2+x} + (2 - 3x)\,O_2 \rightleftharpoons 6UO_{2.666} \tag{3.27}$$
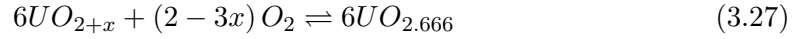
Thus, the variation of weight can be expressed as follows:

$$\frac{\Delta W}{W_i} = \frac{W_f - W_i}{W_i} = \frac{MW_{UO_{2.666}} - MW_{UO_{2+x}}}{MW_{UO_{2+x}}} \tag{3.28}$$

where W_f and W_i are final and initial weight, respectively. MW is the molar weight. From eq. (3.27) one can get the expression for x:

$$x = \frac{10.6556 - 270.0277\frac{\Delta W}{W_i}}{15.9994\frac{\Delta W}{W_i} + 15.9994} \tag{3.29}$$

A similar approach can be used also in case of reduction of the sample from hyperstoichiometric state to stoichiometric one. In this case, sample was heat treated up to 1200 K under Ar/H_2 flow. The reduction was performed to find at which temperature nanoparticles reduce, data that were then used to perform heat treatment before melting experiments. In this case, the reaction is the following:

$$UO_{2+x} \rightleftharpoons UO_{2.00} + \frac{x}{2}O_2 \tag{3.30}$$

Using the same approach as before, the expression for the variation of weight is:

$$\frac{\Delta W}{W_i} = \frac{W_f - W_i}{W_i} = \frac{MW_{UO_{2.00}} - MW_{UO_{2+x}}}{MW_{UO_{2+x}}} \tag{3.31}$$

References

[1] M.J. Takagi. *J. Phys. Soc. Jpn.*, 9:359, (1954).

[2] C.R.M. Wronski. *British J. Appl. Phys.*, 18:1731, (1967).

[3] B.T. Boiko, A.T. Pugachev, and V.M. Bratsyhin. *Sov. Phys. Solid State*, 10:2382, (1969).

[4] C.J. Coombes. *J. Phys. F*, 2:441, (1972).

[5] P. Buffat and J-P. Borel. *Phys. Rev. A*, 13:2287, (1976).

[6] M. Blackman and J.R. Sambles. *Nature (London)*, 226:938, (1970).

[7] R. P. Berman and A. E. Curzon. *Canadian Journal of Physics*, 52:923, (1974).

[8] K.F. Peter, Y.W. Chung, and J.B. Cohen. *Appl. Phys. Lett.*, 71:2391, (1997).

[9] K.F. Peter, Y.W. Chung, and J.B. Cohen. *Phys. Rev. B*, 57:13430, (1998).

[10] S.L. Lai, J.Y. Guo, V. Petrova, G. Ramanath, and L.H. Allen. *Phys. Rev. Lett.*, 77:99, (1996).

[11] G. Schierning, R. Theissmann, H. Wiggers, D. Sudfeld, A. Ebbers, D. Franke, V.T. Witusiewicz, and M. Apel. *J. Appl. Phys.*, 103:084305, (2008).

[12] D. Manara, M. Sheindlin, W. Heinz, and C. Ronchi. *Rev. Sci. Instrum.*, 79:113, (2008).

[13] D. Manara, C. Ronchi, M. Sheindlin, M. Lewis, and M. Brykin. *J. Nucl. Mater.*, 342:148, (2005).

[14] F. De Bruycker, K. Boboridis, D. Manara, P. Pöml, M. Rini, and R.J.M. Konings. *J. Nucl. Mater.*, 419:186, (2011).

[15] D. Manara, R. Böhler, K. Boboridis, L. Capriotti, A. Quaini, L. Luzzi, De Bruycker, C. Guéneau, N. Dupin, and R. Konings. *Procedia Chemistry*, 7:505, (2012).

[16] R. Böhler, M. J. Welland, F. De Bruycker, K. Boboridis, A. Janssen, R. Eloirdi, R.J.M. Konings, and D. Manara. *J. Appl. Phys.*, 111:113501, (2012).

[17] C.A. Utton, F. De Bruycker, K. Boboridis, R. Jardin, H. Noel, C. Guéneau, and D. Manara. *J. Nucl. Mater.*, 385:443, (2009).

[18] H. F. Jackson, D. D. Jayaseelan, D. Manara, C. P. Casoni, and W. E. Lee. *J. Am. Cer. Soc.*, 94:3561, (2011).

[19] M.J. Welland, W.T. Thompson, B.J. Lewis, and D. Manara. *J. Nucl. Mater.*, 385:358, (2009).

[20] F. De Bruycker, K. Boboridis, P. Pöml, R. Eloirdi, R.J.M. Konings, and D. Manara. *J. Nucl. Mater.*, 416:166, (2011).

[21] L. Capriotti and A. Quaini. *High temperature behaviour of nuclear materials by laser heating and fast pyrometry.* Master's thesis, Politecnico di Milano, (2011).

[22] D. Manara. *Melting transition measurements in uranium dioxide.* PhD thesis, University of Warwick, (2004). Technical Note JRC-ITU-TN-2004/05.

[23] O. Svelto. *Principles of lasers.* Plenum Press, third edition, (1989).

[24] F.P. Chiang, J. Adachi, R. Anastasi, and J. Beatty. *Optical Engineering*, 21:379, (1982).

[25] R 48 tungsten ribbon lamps for the calibration of radiation. Technical report, OIML, 2004 (E).

[26] Physicalische Technische Institut Berlin (PTB) calibration sheet, (2010).

[27] R.E. Dinnebier and S.J.L. Billinge. *Powder diffraction. Theory and Practice.* RSC Publishing, (2009).

[28] P. Scherrer. Bestimmung der grösse und der inneren struktur von kolloidteilchen mittels röntgenstrahlen. *Nachr. Ges. Wiss. Göttingen*, 26:98, (1918).

[29] E. Roduner. *Nanoscopic Materials: Size-dependent Phenomena.* RSC Publishing, (2006).

[30] Q. Jiang, L.H. Liang, and D.S. Zhao. *J. Phys. Chem. B*, 105:6275, (2001).

[31] P. Perio. *Contribution to the Crystallography of the Uranium - Oxygen System.* PhD thesis, University of Paris CEA-363, (1955).

[32] F. Grønvold. *J. Inorg. Nucl. Chem.*, 1:657, (1955).

[33] N.W. Ashcroft and N.D. Mermin. *Solid State Physics.* Harcourt College Publisher, (1976).

[34] R.J. Nemanich and S.A. Solin. *Phys. Rev. B*, 20:392, (1979).

[35] W. Heisenberg. *Zeitschrift für Physik*, 43:172, (1927).

[36] A. Li Bassi, D. Cattaneo, V. Russo, C.E. Bottani, E. Barborini, T. Mazza, P. Piseri, P. Milani, F.O. Ernst, K. Wegner, and S.E. Pratsinis. *J. Appl. Phys.*, 98:074305, (2005).

[37] Z.V. Popović, Z. Dohčević-Mitrović, M.J. Konstantinović, and M. Šćepanović. *J. Raman Spectrosc.*, 38:750, (2007).

[38] A.K. Arora, M. Rajalakshmi, T.R. Ravindran, and V. Sivasubramanian. *J. Raman Spectrosc.*, 38:604, (2007).

[39] J.E. Spanier, R.D. Robinson, F. Zhang, S.-W. Chan, and I.P. Herman. *Phys. Rev. B*, 64:245407, (2001).

[40] J.H. Parker Jr., D.W. Feldman, and M. Ashkin. *Phys. Rev.*, 155:712, (1967).

Chapter 4

Experimental results

This chapter presents the main results of the current study on the melting behaviour as well as of the pre- and post-melting characterisation of the refractory nanostructured oxides introduced in sections 2.2 and 2.3 in Chapter 2. Furthermore, some experiments on bulk material have been carried out as well, to compare to the results obtained from nanoparticles.

During this experimental campaign a number of challenges and difficulties had to be faced, also in relation to the fact that investigation of high-temperature (1500-4000 K) behaviour of nanostructured refractory oxides is a pioneering work, because in this temperature range such materials have not been studied yet.

The enhanced surface-to-volume ratio leads to higher instability and chemical reactivity of such compounds. In particular, urania nanoparticles had the tendency to be oxidised in contact with oxygen traces already at room temperature. Since melting temperature is largely affected by stoichiometry (see Chapter 2 and Ref. [1]), it was not possible to determine the contribution of the sole size effect on melting temperature depression.

A possible way to overcome the problem was the study of size-dependent melting temperature on nanostructured ThO_2 samples, whose oxidation state (+4) can be considered to be stable up to temperatures close to melting.
From literature, it is well known that the effect is striking (the melting transition can occur several hundreds K below the melting temperature of the corresponding bulk material) for metal particles whose diameter is below 10-5 nm, depending on the material [2–5]. The first question to be answered was if such effect could be seen also for refractory oxides. Hence, the investigation was firstly done on particles whose size was below 5 nm. For the second step that had been foreseen, nanostructured ThO_2 with grain size between 30-50 nm should have been studied, in order to compare the results with the ones obtained for nanostructured urania samples, whose size before melting was estimated in that range (see subsection 4.1.1).

However, as already mentioned, small amount of material was available, because of difficulties in synthesis process via organic approach[1]. The pellets made from pressed

---

[1]When the study begun, conditions to obtain ThO_2 nanoparticles via aqueous synthesis were not

powder were mechanically unstable at high temperature, due to high heating rates that caused thermal stresses inside both the sample and the sample holder, which often broke. Moreover, the presence of organic ligand was often a source of uncertainty in determining the melting temperature.

Melting experiments could be performed only once for each sample surface (only on some pellets it was sometimes possible to perform two shots, one for each side): upon freezing, in fact, the material solidifies into the μm-sized structure, preventing the sample from being used again for further investigation of size effect. The current results are often affected by large uncertainties, and can therefore be considered as partly exploratory. Nonetheless, their importance lies in the fact that they open the way to a still unexplored field.

4.1 Uranium dioxide

As discussed in subsection 2.3.1 of Chapter 2, six pellets were prepared, named NCPn, $n = 1 - 6$. One of these (NCP3) was fully used to characterise the material before laser heating experiments, whereas the others were melted with the laser, and the molten and unmolten parts were analysed and compared.

4.1.1 Characterization before laser heating

Characterization before melting was performed through Scanning and Transmission Electronic Microscopy and XRD to determine grain size and estimate stoichiometry. When the small sample mass permitted so, also thermogravimetry analysis was used to corroborate XRD results.

TEM images show agglomeration of nanoparticles with large size dispersion. All software usually employed for particle size analysis work on a pixel contrast-based mode, by scanning the image until it finds the edge of the particle. This is not applicable to agglomerations, so a manual approach has been used yielding the result of a mean diameter of (30 ± 20) nm[2]. A summary of particle size distribution is reported in Fig. 4.1 for NCP3.

XRD diffraction pattern of sample NCP3 and NCP6 (for the unmolten part) is shifted towards higher angles compared to standard uranium dioxide, as shown in Fig. 4.2(b). The XRD peak shift is linked to a contraction of the lattice parameter, which in μm-sized material is due to oxidation as in eq. (3.23).

---

established yet.

[2]The uncertainty has been calculated in two ways: when the number of particles that could be counted was more than 30, a Gaussian distribution has been used, otherwise the Student's t-distribution has been employed.
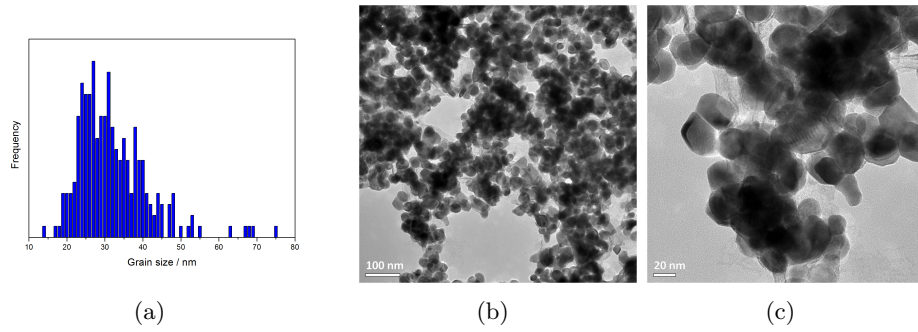
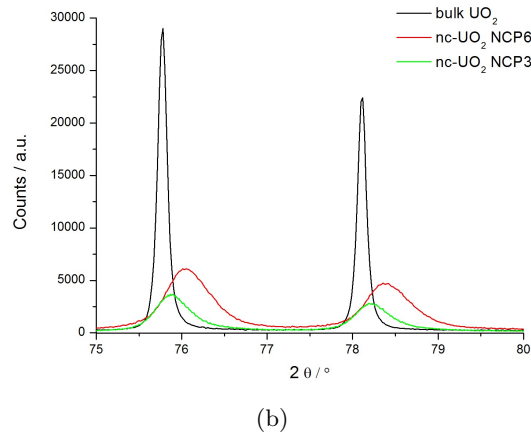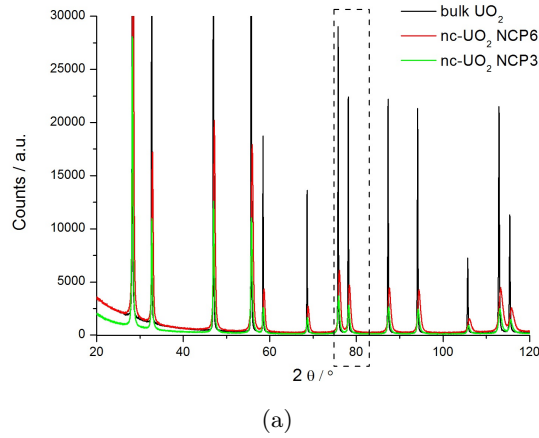**Figure 4.1:** (a) Grain size distribution and (b,c) TEM images of UO$_2$ nanoparticles for sample NCP3.


(a)

(b)

Figure 4.2: (a) Experimental XRD pattern for bulk UO$_2$ (black line), nanostructured urania (red and green lines). (b) Magnification of (a). The differences in the diffractograms of the two nanostructured samples are due to dishomogeneities in the oxidation state and in the grain size (cfr. 30 ± 20 nm).

However, as discussed before, in nanoparticles the lattice contraction can be also due to a size effect. The lattice parameter measured for UO_2 nanoparticles of different size produced at ITU is shown in Fig. 4.3. Fitting has been carried out supposing a linear dependency of lattice strain on the inverse of grain size, based on literature data (see for example Chapter 2 in [6]).
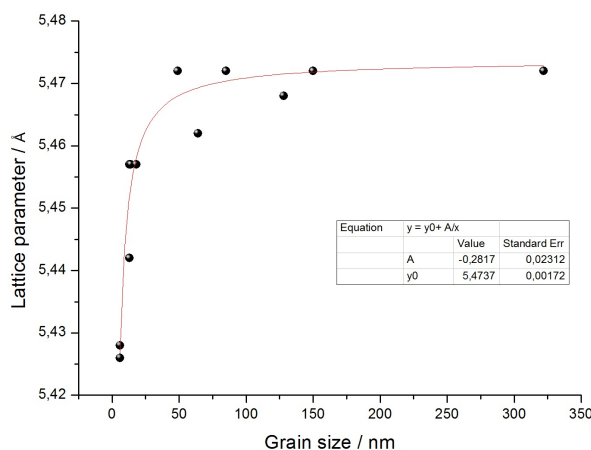
Figure 4.3: Black dots: measured lattice parameter for nc-UO_2. Red line: fitting of experimental data.

From the phase diagram of the µm-sized U-O system (recalled in Fig. 4.4), at room temperature, in the range between O/M = 2.00 and O/M = 2.25 a solid solution of stoichiometric UO_2 and U_4O_9 is expected. Usually, when another oxidised phase such as U_4O_9 is present, the main effect of oxidation on the XRD spectra at room temperature is the appearance of two distinguishable peaks belonging to the two phases (see for example Fig. 4.5).

As can be seen from Fig. 4.2(b) and Fig. 4.5, in the case of nanoparticles, the broadening due to size effect produces single, large peaks: they can be attributed either to a single phase of stoichiometric UO_2 with contracted lattice parameter, or to a convolution of peaks belonging to nanocristalline UO_2 and U_4O_9.

Calculations of lattice parameter have been done using two different software: FullProf and Jana2006. Both software use Rietveld refinement method: it uses a least squares approach to refine a theoretical line profile until it fits the measured profile. Fits have been performed either supposing a single phase (UO_2) or coexistence of two phases (UO_2 and U_4O_9)[3]. From the lattice parameter values of the UO_2 phase, the particle mean size has been calculated either using the calibration curve in Fig. 4.3 or directly through the software[4]. Results obtained for two representative nanostructured samples are reported

---

[3]It was not always possible to fit powder pattern with two-phases. Calculations did not always converge. It is possible, in fact, that the formation of U_4O_9 is hindered in nano-crystals. This point deserves further investigation in future research.
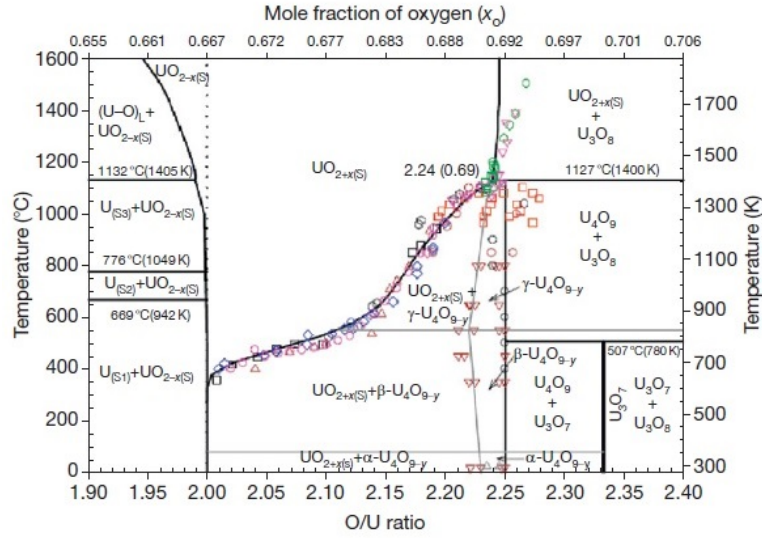
[4]This option was available only with Jana2006.

Figure 4.4: UO$_2$ phase diagram calculated from O/U=1.90 to 2.4 as in reference [7].

in Table 4.1.

**Table 4.1: Results of Rietveld refinement analysis of the nc-UO$_2$ pellets XRD experimental diffraction patterns. "/" symbol stands for not performed fit.**

Sample	FullProf				Jana2006			
	Single phase		Two Phases		Single phase		Two Phases	
	a [Å]	Size [nm]	a [Å]	Size [nm]	a [Å]	Size [nm]	a [Å]	Size [nm]
NCP3	5.4586	18.65[a]	/	/	5.4594	19.69[a] 36.47[b]	5.4598 (UO$_2$) 21.7679 (U$_4$O$_9$)	42.34[b] 38.42[b]
NCP6	5.4537	14.09[a]	/	/	5.4609	21.99[a] 43.03[b]	5.4583 (UO$_2$) 21.7648 (U$_4$O$_9$)	37.65[b] 33.18[b]

[a] Value obtained from fitting of data in Fig. 4.3
[b] Value obtained from software Jana2006

The hypothesis that the lattice contraction is due only to size effect leads to understimation of the mean grain size of the samples, hence it can not be right. Both effects are present: grain size is certainly a factor for shifting, but there is also a shift due to the deviation from stoichiometry. In fact, TG analysis showed that samples were oxidised. However, measurements were not stable enough to give a precise estimation of the O/M ratio, which was in the broad range 2.15 ± 0.067. In order to have another estimation of the O/M ratio of the samples before melting, Perio's formula (see eq. (3.23)) was applied to
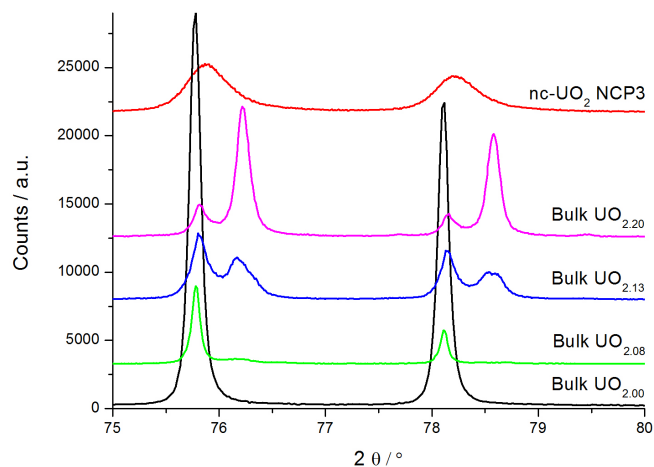
Figure 4.5: Magnification of the experimental XRD pattern for several bulk UO$_{2+x}$ samples and nanostructured urania pellet.

the lattice parameter calculated in Table 4.1 with Jana2006: an estimation for O/M of 2.10 ± 0.02[5] was obtained and considered the most significant.

Moreover, Raman spectroscopy was performed using the Kr$^+$ Coherent$^®$ cw laser radiating at 647 nm as an excitation source. Characterization of uranium oxides through Raman spectroscopy has been extensively used. UO$_2$ phase has two characteristic peaks at 445 cm^{-1} [8–11] and 1151 cm^{-1} [12–14].

U$_4$O$_9$ is a superstructure of UO$_2$ with β-phase stable above 323 K [15] and α-phase stable below 323 K [16]. Because of local heating under laser beam, peaks from both phases can be present. Main characteristic peaks of U$_4$O$_9$ are at 160 cm^{-1} and 630 cm^{-1}. The first one is attributed to the $M_2^{'}$ mode that in U$_4$O$_9$ is located at the centre of the Brillouin zone [17]. The other is explained as being a vibrating mode involving the atoms in the cluster of interstitial oxygen atoms [17].

Formation of U$_4$O$_9$ is the first step in UO$_2$ oxidation towards U$_3$O$_8$. Spectra of U$_3$O$_8$ are quite complex, due also to presence of UO$_3$ phase. Detailed explanation of spectra can be found in [18].

Measurements on urania samples were always affected by low signal/noise ratio, as can be seen from Fig. 4.6. Nevertheless, it was possible to distinguish some peaks characteristics of the three phases. UO$_2$ characteristic peaks are put in evidence in Fig. 4.6 through the two dotted black vertical lines. Beside the fluorite structure, also U$_4$O$_9$ and U$_3$O$_8$ peaks can be recognised, as can be seen from a comparison with the bulk UO$_{2.09}$/UO$_{2.13}$ and U$_3$O$_8$, respectively. Fluorescence has been substracted to put nc-UO$_2$ peaks into evidence in Fig. 4.7. Table 4.2 shows a summary of them, with possible

---

[5]The value of the lattice parameter obtained either with a single-phase fit or a two-phases fit were quite closed and gave very close values for the O/M ratio.

assignment based on literature. It was not possible to assign all the modes present, which goes beyond the scope of this thesis. Peak position values do not always coincide exactly with literature values: precise deconvolution was extremely difficult for the bad quality of the spectra, but an effect of phonon confinement might be also present.

Table 4.2: Raman modes found in the present work for nc-pellets. The symbol "/" states that no literature data exist for the marked modes, although they have been observed in the current spectra.

Raman shift / cm^{-1}	Assignment	References
240	U_3O_8 line of uncertain origin	[19, 20]
$\approx$276	U_4O_9 TO mode[a]	[17]
347	U_3O_8 A_{1g} U-O stretching	[21]
445	UO_2 T_{2g} U-O stretching	[8–11, 19]
564	UO_2 LO mode	[22]
630	U_4O_9 interstitial oxygen clusters vibration mode	[17]
$\approx$780	/	
$\approx$886	$A_{1g} + E_g$	[23]
1148	UO_2 2LO mode	[22]

[a] TO mode is Raman-forbidden in UO_2 but it becomes allowed in U_4O_9.

From all the analysis we could conclude that samples were clearly oxidised before melting experiments even if they were kept under inert atmosphere most of the time. This confirmed that urania nanoparticles suffer from higher chemical instability, having faster kinetics of oxidation compared to standard material, as expected.
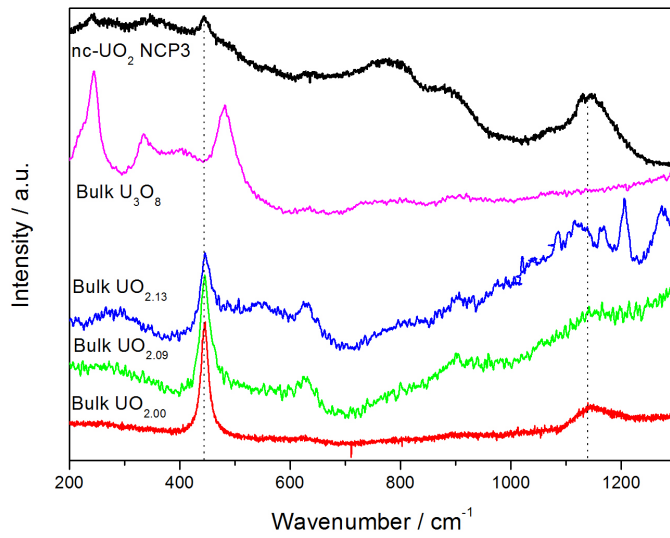
Figure 4.6: Raman spectrum of nanostructured UO₂ pellet compared with spectra recorded for bulk samples with different O/M ratio.
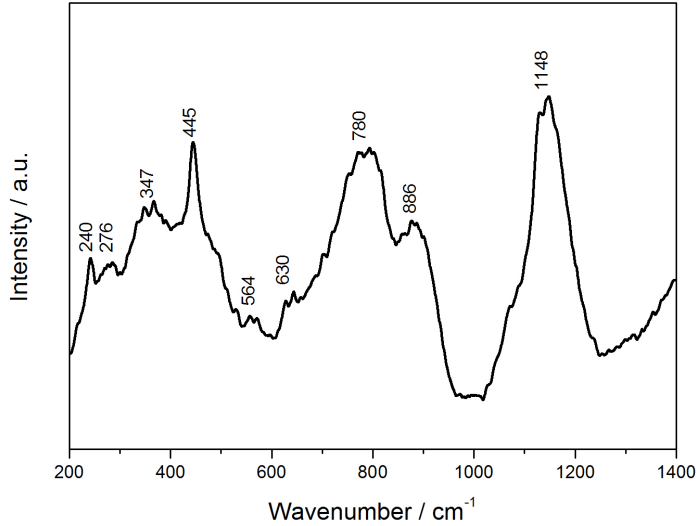

Figure 4.7: Raman spectrum of nanostructured UO₂ pellet. The fluorescence has been substracted and the spectrum smoothed.

4.1.2   Laser heating results

Firstly, tests on bulk stoichiometric uranium oxide were performed using the same power profile (ramp) employed for nanocrystalline samples, in order to validate the pyrometer calibration with the notch filter. As it can be seen from Table 4.4, results obtained are in optimal agreement with the ones reported in literature $((3120 \pm 30)\,\mathrm{K})$ [1, 24, 25].

Nc-samples were established to be hyperstoichiometric as discussed in subsection 4.1.1. The main issue was then the determination of the oxidation state during melting experiments, since the O/M ratio also causes melting point depression. Therefore, melting experiments were also performed on bulk UO_{2+x} with $x = 0.09$, $x = 0.13$, $x = 0.20$ in the same experimental conditions for comparison with what obtained for nanostructured materials. Table 4.3 reports the measured melting temperatures for such samples. The NSE for bulk urania samples was assumed equal to 0.83 as determined from previous work [26]. All the uncertainties reported in this Chapter are calculated using the formula introduced in section 3.5 and are equal to one standard deviation.

Table 4.3: **Melting temperatures measured in this work for bulk $UO_{2.00}$ and UO_{2+x}.**

Sample	$T_{melting}$ / K	δT / K
$UO_{2.00}$	3124	44
$UO_{2.09}$	2865	39
$UO_{2.13}$	2771	37
$UO_{2.20}$	2490	33

It is know that at low pressures and at very high temperatures hyperstoichiometric urania is very unstable. As a consequence, gas phase rich in oxygen evaporates [27], causing a reduction of the sample. The change in composition is mostly pronounced only in the last stage of heating and during cooling [27]. Thus, solidus and liquidus temperatures recorded during cooling are expected to be at higher values compared to the melting, corresponding to a less oxidised composition (see phase diagram in Fig. 2.1). The values measured for bulk stoichiometric samples have been compared with the solidus/liquidus temperatures in [27] to determine the new oxidation state of the samples after melting. This helps to estimate the oxidation state of nc-UO_2 pellets in the cooling stage of the melting experiments. The values are reported in Table 4.4.

Table 4.4: **Summary of liquidus/solidus temperatures measured in this work for UO_{2+x}. The new composition has been calculated comparing liquidus/solidus temperatures values with the ones in [27].**

Sample	$T_{liquidus}$ / K	δT / K	$T_{solidus}$ / K	δT / K	New composition [27]
$UO_{2.09}$	2963	28	2927	27	$UO_{2.07}$
$UO_{2.13}$	2948	28	2931	27	$UO_{2.07}$
$UO_{2.20}$	2939	27	2745	25	$UO_{2.12}$

Table 4.5 shows a summary of the temperatures at which onset of liquid state was detected in nanostructured pellets. Furthermore, liquidus and solidus temperature corresponding

to thermogram inflections on the cooling stage are given. All shots were performed in Ar/H$_2$. In case a second shot on the "fresh" side of the sample was performed, melting temperature increased: it is probable that a reduction of hyperstoichiometric state took place either during first melting or during the first stage of cooling. Also the NSE was measured by radiance spectroscopy, showing no different value from the one of the μm-sized material.

Table 4.5: Summary of laser heating results obtained for nc-UO$_2$. Symbol "/" means that it was not possible to determine thermogram inflection or the onset of RLS vibrations.

Sample	T$_{melting}$ / K	δT / K	T$_{liquidus}$ / K	δT / K	T$_{solidus}$ / K	δT / K
NCP1	2750	37	3160	44	3024	42
	2813^a	38	3124	44	/	/
NCP2	2736	37	2924	40	2794	38
	2845^a	39	/	/	/	/
NCP5^b	/	/	3080	43	3000	42
NCP6^c	2820	38	3098	43	3039	42

^{a} Second shot on other surface of the sample.
^{b} An *in-situ* preliminary heat treatment was done with the laser (power 45 W, 10 s) in order to try to remove the oxidised surface. Particle growth before melting is certain.
^{c} An *in-situ* preliminary heat treatment was done with the laser (power 45 W, 5 s) in order to try to remove the oxidised surface. Particle growth before melting is very likely.

Fig. 4.8 shows the thermogram of a laser shot performed on one pellet of nanostructured urania.

The shape of nc-UO$_2$ thermogram has some significant differences with the μm-sized UO$_2$ one (Fig. 4.8(a)) in the heating part. The final part of heating was always characterised by fast temperature fluctuations probably due to high thermodynamic instability of the material at temperatures above melting, that seems more pronounced in nanoparticles. A possible reason for such a behaviour might be the metastability of the formed liquid phase with respect to the μm-sized solid phase (see Fig. 1.1 in Chapter 1). In Fig. 4.8, the onset of vibrations in the RLS clearly starts at temperatures much lower than the expected solidus temperature for μm-sized UO$_2$. The value is lower compared to the one obtained for μm-sized UO$_{2.09}$ and UO$_{2.13}$, which have an oxidation state close to the mean one estimated for "fresh" nanostructured pellets.

Furthermore, in Fig. 4.9, the thermogram of nc-UO$_2$ is compared with thermogram of μm-sized UO$_{2.09}$ and UO$_{2.13}$. The shape of the cooling stage resembles the one of UO$_{2.13}$. The solidus and liquidus temperatures of the nc-UO$_2$ are slightly higher compared to the ones of the UO$_{2.13}$. Thus, the oxidation state of this nanostructured sample after melting can be estimated to be O/M < 2.07, according to the values given in Table 4.4. However, the starting O/M ratio of the nc-UO$_2$ samples was not always homogeneous, and in some cases a solidus temperature below 2800 K was also measured (an example is given in Fig. 4.10), revealing a higher O/M ratio of the sample. Moreover, instabilities and a large depression of temperature were observed in the cooling stage, due to massive

vaporisation (as confirmed by the black/orange plume which was deposited on upper part of graphite sample holder after the experiment (see Fig. 4.11(b)). The measured values of solidus and liquidus temperature would correspond to a ratio $O/M = 2.12$ [27]. Therefore, melting point depression due to non-stoichiometry effect seems to be comparable with the hypothetical size effect in some cases.
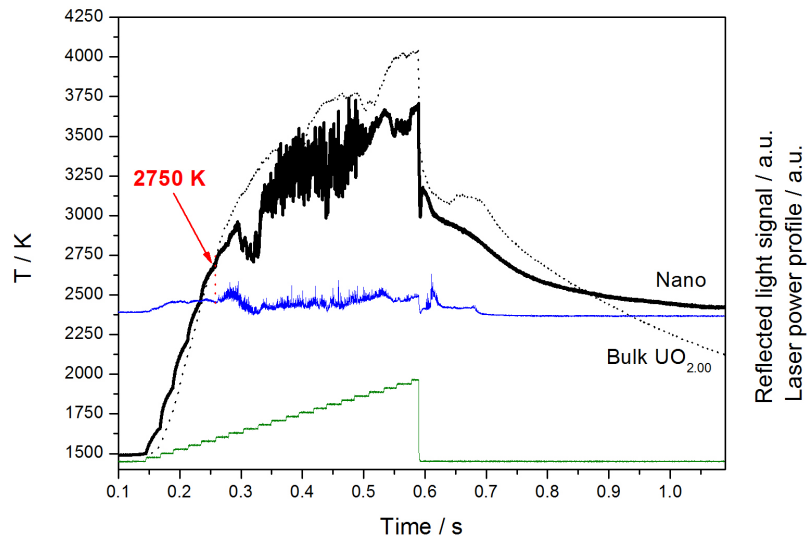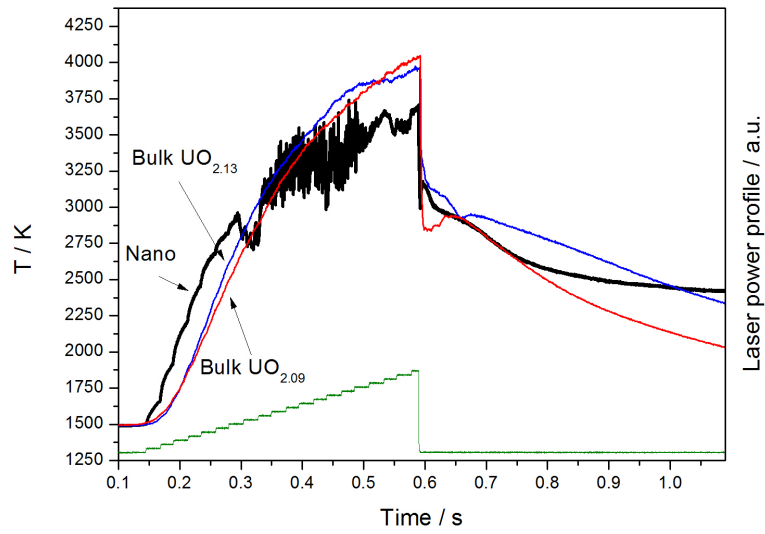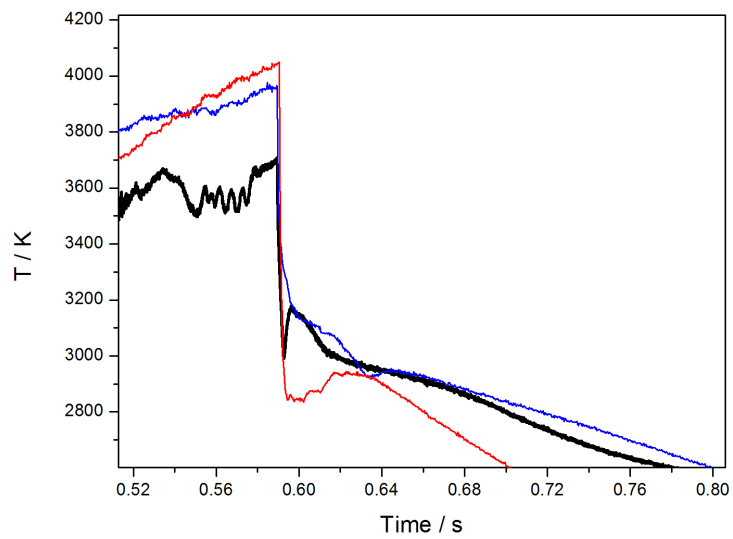
(a)
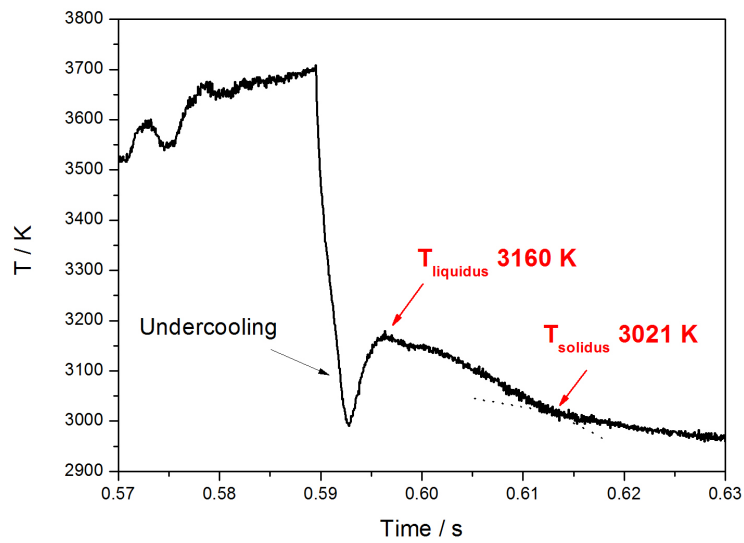
(b)

Figure 4.8: **Laser shot on UO_2 nanostructured pellet (NCP1). (a) Thermogram compared with the one of reference bulk $UO_{2.00}$ (solid and dotted black lines, respectively). Green line: power profile. Blue line: reflected probe laser signal. (b) Magnification of thermal arrest of sample. The slower cooling rate of the nc-UO_2 sample is due to misfunctioning of the laser in this experiment (parasite residual power).**
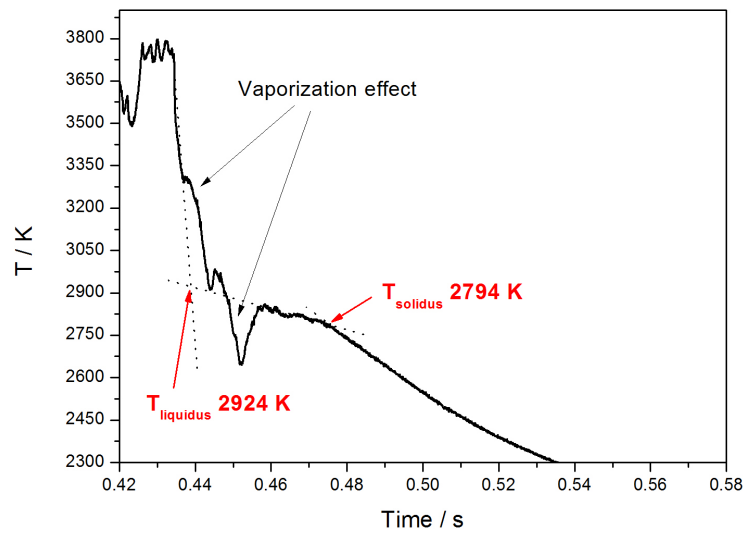
(a)

(b)

Figure 4.9: **Laser shot on UO$_2$ nanostructured pellet (NCP1-solid black line). (a) Thermogram compared with the one of reference bulk UO$_{2.09}$ (red line) and UO$_{2.13}$ (blue line) (b) Magnification of thermal arrest of the samples.**

70
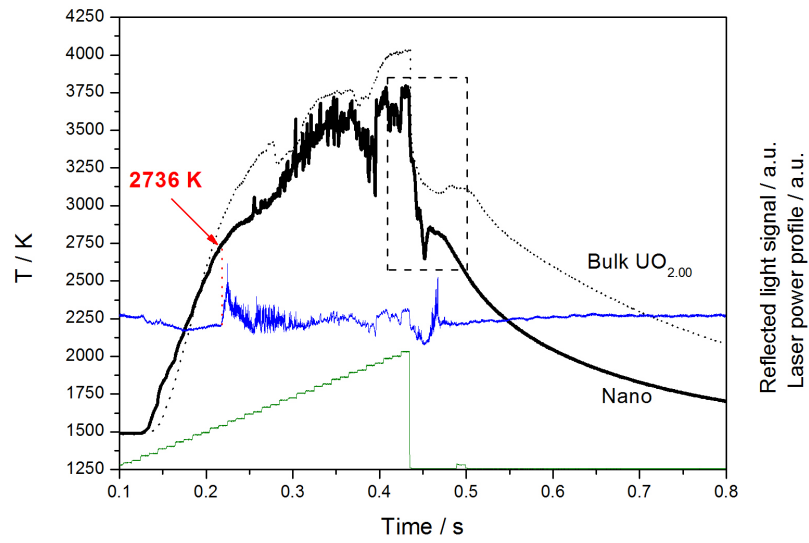
(a)

(b)

Figure 4.10: **Laser shot on nanostructured UO₂ pellet (NCP2). (a) Thermogram compared with the one of reference bulk UO$_{2.00}$ (solid and dotted black lines, respectively). Green line: power profile. Blue line: reflected probe laser signal. (b) Magnification of thermal arrest of sample.**

(a)   (b)
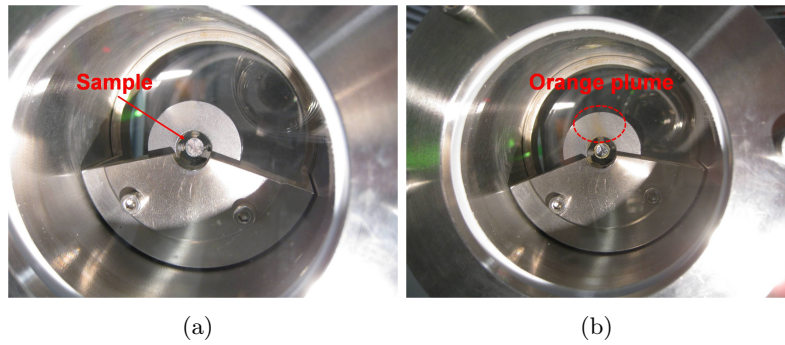
Figure 4.11: Pictures of nanostructured UO$_2$ pellet. (a) Before laser heating. (b) After laser heating.

4.1.3   Characterization after laser heating

Firstly, a study of surface and grain dimension change after melting was done with SEM. The molten zone was characterized by a homogeneous layer with several cracks due to the high temperature gradients during the heating/cooling processes. The unmolten zone, instead, showed a much more irregular surface, with several spherical particles deposited on it (Fig. 4.12). Most probably, they are aerosol particles vaporised during melting from surface which subsequently recondensed and were deposited on sample surface. An interesting qualitative comparison can be done with the conformation and shape of some aerosol structures produced with fast laser heating experiments as well, as in Fig. 4.13 [28].
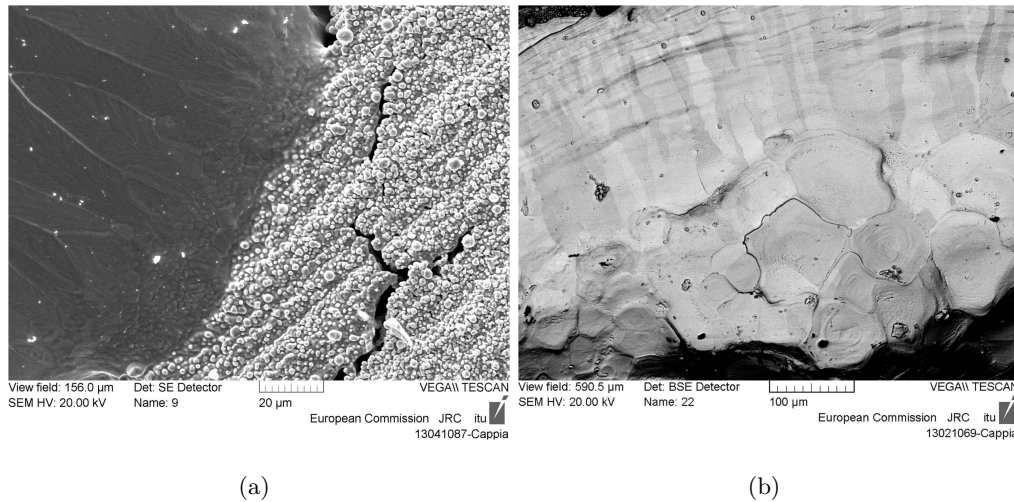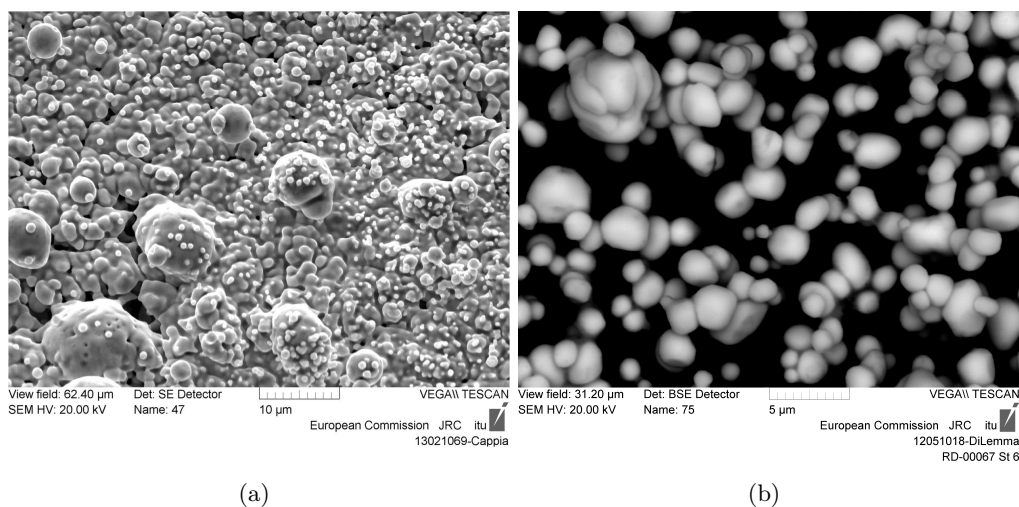

(a)   (b)

Figure 4.12: SEM images of nanostructured UO$_2$ sample: (a) SE image of interface between molten and unmolten zone (b) BSE image of the molten part.

(a)   (b)

Figure 4.13: (a) SE image of aerosol particles deposited on the unmolten zone of NCP6. (b) Example of aerosol particles collected on filter [28].

In Fig. 4.14, the molten layer can be recognised. Below that, a zone with columnar growth and another one with no columnar growth are present: the columnar growth comes from vertical solidification process from the bottom of the molten pool, whereas the other one is due to the solidification coming from the periphery towards the centre of the pool.
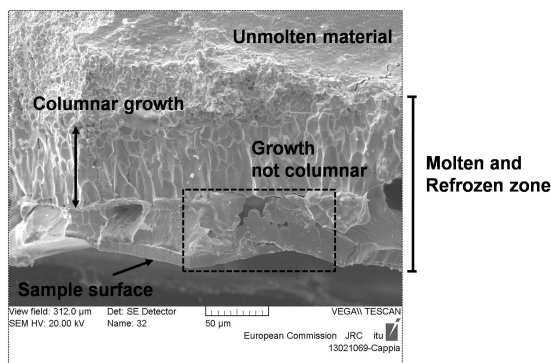

Figure 4.14: SE image of the molten zone in sample NCP2 (cross section).

Also XRD analyses were performed: after melting, peaks became narrower, due to particle growth, showing a shoulder obviously coming from the U_4O_9 phase, finally formed in the re-crystallised, macroscopic grains of the melted and re-frozen material.

However, this point still needs further and deeper research, to be developed in a future investigation. In fact, when Rietveld refinement was performed on XRD diffractograms of nc-samples[6] after melting with a two-phases approach (as described in subsection

---

[6]It is not completely correct to talk about nanoparticles after melting. Despite this, the name allows to distinguish quickly the samples under study from the µm-sized reference material.
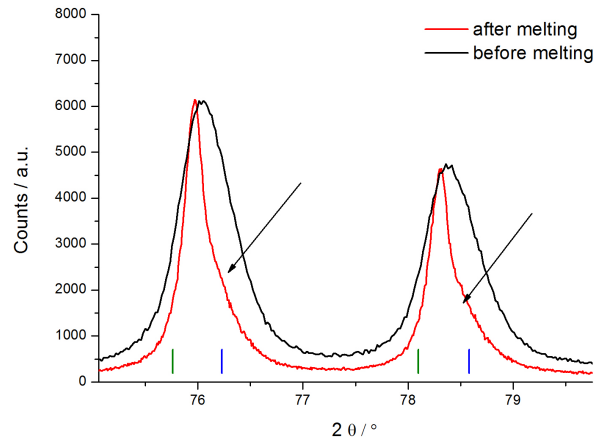
Figure 4.15: Magnification of experimental XRD pattern of nanostructured UO$_2$ sample NCP6 before melting (black line) and after melting (red line). Also position of U$_4$O$_9$ characteristic peaks (blue lines) and UO$_2$ characteristic peaks (green lines) are reported.

4.1.1) to make a comparison on grain size, results were not congruent, predicting a decrease of grain size for the U$_4$O$_9$ phase. As a consequence, XRD diffraction pattern could not be used for quantitative estimation of the grain dimension evolution after melting, but only for qualitative change. Analysis of the grain size after melting was performed through TEM. The agglomerations formed after melting were too thick to permit HRTEM analysis, hence, only STEM images were recorded from which the size of agglomerations was calculated in the range 200-600 nm (Fig. 4.16(b) and 4.16(c)).
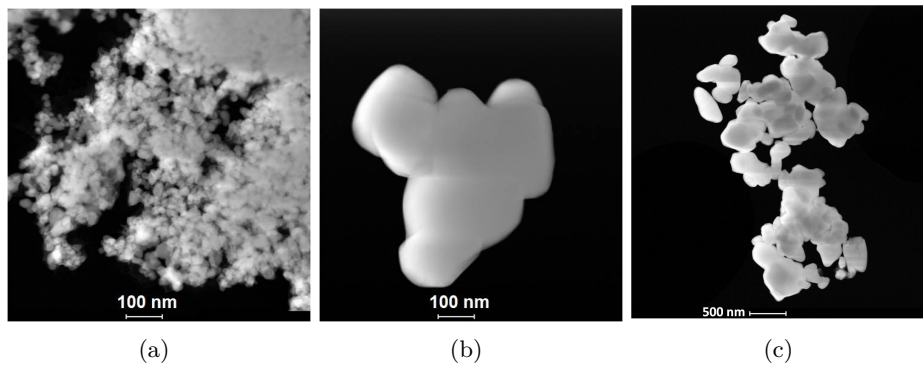
Figure 4.16: (a) STEM image of an unmolten nc-UO$_2$ pellet (NCP6) compared with (b)-(c) STEM images of a molten nc-UO$_2$ pellet (NCP6).

4.1.4 Discussion and Conclusions

Several techniques have been used to fully characterise samples before melting experiments, showing quite broad particle size distribution and oxygen hyperstoichiometry of the samples.

Concerning laser heating experiments, nanostructured UO_2 samples have been successfully melted using the described laser technique before massive agglomeration took place. A size effect is present, but it could not be clearly distinguished from the melting temperature depression coming from hyperstoichiometry. As a consequence, it can be concluded that for particles whose size is in the range (30 ± 20) nm the melting temperature is between 2730 K and 2850 K, for the combined effect of size and faster oxidation process.

Applying Pawlow's melting point depression model introduced in Chapter 1 and using in eq. (1.3) the values reported in [29] for UO_2, one can estimate a melting point of 3096 K for particles of mean size of 30 nm, only 24 K less than melting temperature of bulk material. The melting point depression predicted is much less than what measured. This would suggest that the observed melting point depression is due to oxidation more than a size effect. However, one should not forget that the applicability of Pawlow's model to refractory oxides is doubtful. Therefore, the corresponding results should be taken as a very roughly approximation only. Finally, molecular dynamics (MD) simulations ongoing at ITU seem to show a melting point depression of 350 K for nc-UO_2 with grains of 3-4nm [30]. Although this result cannot be directly compared with the current experimental data for 30 nm grain sized oxidised UO_2, it can still be kept as an approximate reference for very small actinide dioxide particles.

4.2   Thorium dioxide

Before the presentation of results obtained for nc-ThO$_2$, the first section focuses on the application of Raman spectroscopy to determine grain growth after heat-treatments and melting. The approach was empirical, with the set of a relationship between the FWHM of the T$_{2g}$ peak and the inverse of grain size that has then been used as "calibration curve".

4.2.1   Raman spectroscopy: "Grain size calibration curve"

As mentioned in subsection 3.6.4 of Chapter 3, nanomaterials show a broadening and a shift of the Raman peaks which, according to analytical models, can be correlated to grain dimension. ThO$_2$ has a very intense T$_{2g}$ peak, characteristic of the fluorite structure [11, 31] and suitable for this kind of empirical study[7].

Derivation of an empirical relation between peak characteristics and grain size could provide a powerful, fast and non-destructive analysis to determine local grain evolution within the sample after melting.

To obtain the "calibration" curve, a batch of thoria nanoparticles of 1-2 nm was divided into different amounts which were heated in a furnace at different temperatures (from 700 K to 1400 K with steps of 100 K plus another heat treatment at 1600 K for one hour under an air flux) to induce growth of the grains. The mean dimension of the grains was then estimated through TEM and XRD analysis[8]. For further details, see subsection 4.2.2.

In Fig. 4.17(a), full recorded spectra for some samples are presented, whereas in Fig. 4.17(b) the evolution of T$_{2g}$ peak is shown. All spectra were recorded using the Ar$^+$ Coherent® cw laser radiating at 488 nm.

In the spectrum recorded from original nanoparticles, peaks characteristic of organic ligand are present (they are indicated with an asterisk in Fig. 4.17(a)). Most of the ligand disappears after heat treatment. This was also detectable visually since original samples had yellow/orange colour, whereas after heat treatment they turned white, the characteristic colour of thoria.

---

[7]The same kind of study was not possible for nc-UO$_2$ because the spectra recorded for this material had a huge background as well as peaks coming from other phases (see subsection 4.1.1). This made difficult the deconvolution of the T$_{2g}$ peak to calculate with sufficient precision the FHWM.

[8]Particles were assumed to be spherical, based on phonon confinement model (see Appendix C). This was true for heat-treated particles, but not for starting sample, which was composed of nanorods. The spectra recorded are the result of average confinement of phonons in both dimensions. The diameter of "equivalent" sphere of same volume as the rod was assumed as characteristic dimension for comparison with the other samples.
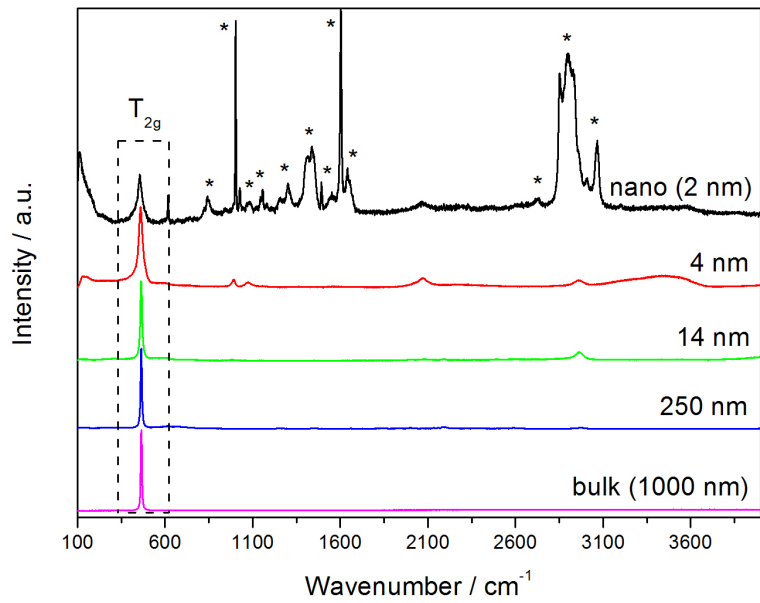
(a)
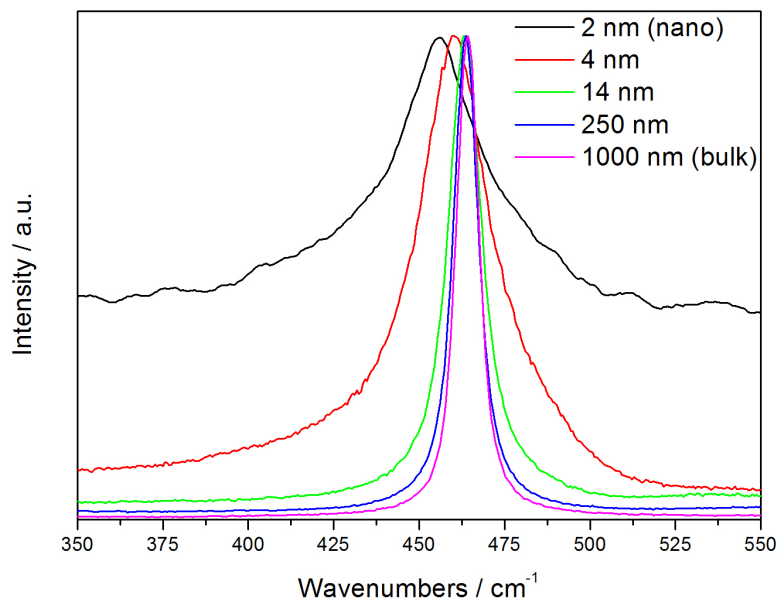
(b)

Figure 4.17: **(a) Raman spectra of nanostructured ThO$_2$ samples (b) Magnification of the** T_{2g} **peak evolution. Laser wavelength: 488 nm.**

For samples treated at higher temperatures, several peaks appear in the region 1000-3000 cm^{-1} which were not present in the bulk material (Fig. 4.18). Spectra were also recorded with other excitation sources (i.e., an Ar$^+$ Coherent$^®$ cw laser radiating at 514 nm and a Kr$^+$ Coherent$^®$ cw laser radiating at 647 nm): using the 647 nm those peaks did not appear, but using the 514 wavelength they were quite intense. The spectra recorded with the 488 nm laser were shifted by the difference between the laser wavelengths and the spectra compared: the modes did not perfectly correspond to the ones observed with the 488 nm laser source, therefore they are not electronic transitions. The origin of those peaks is still not clear, but their assignment goes beyond the scope of this thesis. Further investigations should be carried out to fully understand their origin.
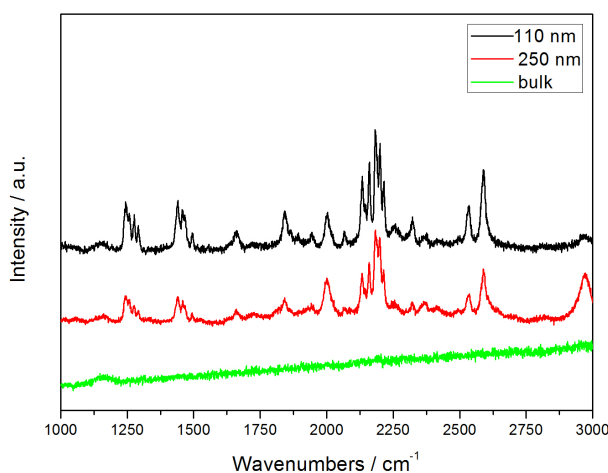
Figure 4.18: Magnification at high wavenumbers of spectra of nanostructured ThO$_2$ samples heat-treated at 1400 K (100 nm-black line) and 1600 K (300 nm-red line). The spectrum of μm-grain sized material (green line) is shown for comparison.

Both full width at half maximum (FWHM) and peak position are plotted vs. the inverse of grain dimension in Fig. 4.19(a) and Fig. 4.19(b), respectively. The first parameter was considered more reliable to set the calibration because it is less affected by the laser characteristics (i.e. polarization, laser power[9]) that were not controlled in the present approach. Moreover the shift was appreciable only for very small particles and for samples with higher grain dimension (mean grain size $d \geq 20$ nm) the difference in the peak position was often within machine calibration uncertainty (≈ 1 cm^{-1}).

A linear fit of data in Fig. 4.19(a) gave the following equation:

$$FWHM = 56.76\,x + 8.47 \tag{4.1}$$

---

[9]It was observed that the increase of laser nominal power affected peak position. Shift up to ≈ 10 cm^{-1} was observed at $P = 1$ W when power overcame hundreds of mW. All spectra presented were recorded at low power (54 mW < P < 70 mW) to avoid this effect.

where x is the inverse grain size. From eq. (4.2) a first estimation of grain size can be obtained as follows:

$$d = \frac{56.76}{FWHM - 8.47} \tag{4.2}$$

with d as nanocrystal diameter.

(a) (b)
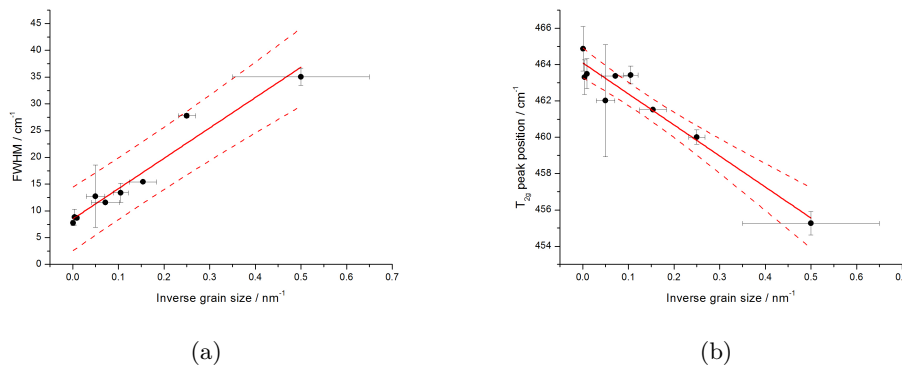
Figure 4.19: (a) FWHM vs. inverse of grain size. (b) T_{2g} peak position vs. inverse grain size. Dotted lines represent $\pm 95\%$ confidence bands. When the grain size$\to \infty$ uncertainty bands lose their physical meaning.

4.2.2 Characterization before melting

Full characterization (XRD and TEM) of as-produced nanoparticles has been published in [32] and [33].

In this work estimation of grain size and particle shape was done on particles annealed at different temperatures to set the Raman calibration curve. Either TEM images analysis or XRD diffraction pattern refinement has been carried out with the same approach described in subsection 4.1.1. Most of the analyses were done using TEM images. For some samples, also reciprocal lattice images (i.e., Fast Fourier Transform images FFT) were recorded. In Fig. 4.20, a comparison among samples annealed at different temperatures is shown: starting nanorods became spherical-like particles. The higher the heat treatment temperature, the bigger the agglomerations with better defined crystalline structure showing clear bright spots in the FFT corresponding to crystalline planes.

For the sample treated at 700 K, both XRD and TEM images were recorded. XRD refinement gave a mean size in good agreement with TEM estimation. In Fig. 4.21, the diffraction pattern of nanoparticles is compared with the one recorded from the μm-sized commercial ThO_2 powder used as reference material. It is clear that the broadening of the peaks due to size effect is occurring, but the peaks coming from the typical fluorite structure of ThO_2 can be recognised. Table 4.6 reports a summary of the grain size determination.

Once the calibration curve was established, samples were analysed using Raman spectroscopy to determine initial state of the material and to estimate grain agglomeration
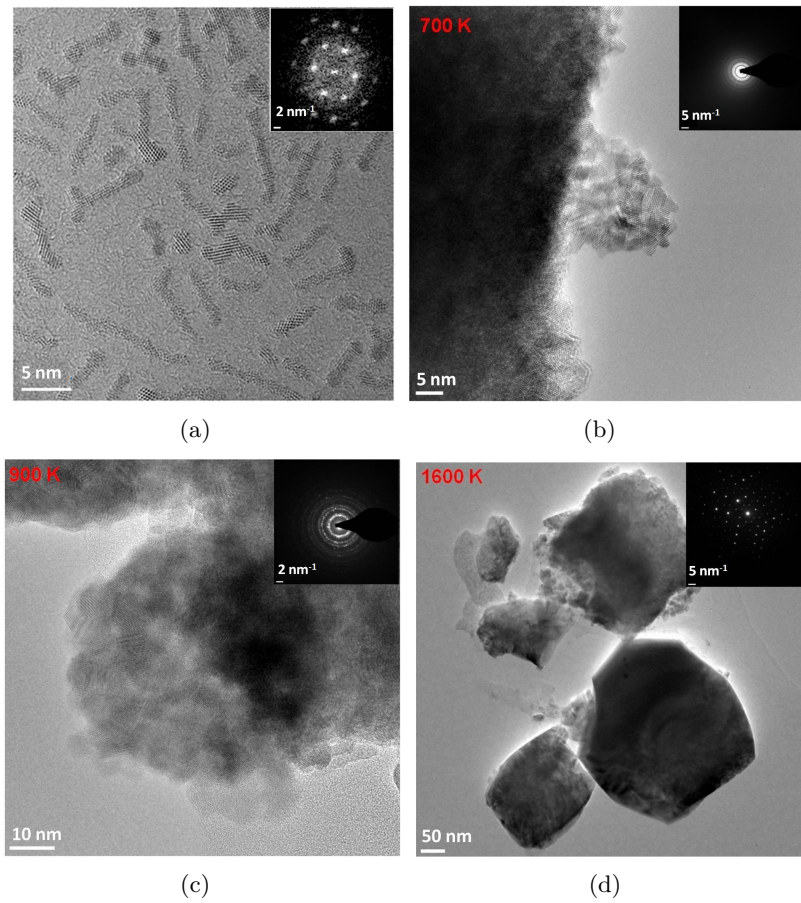
Figure 4.20: **TEM images and corresponding FFT of (a) ThO$_2$ nanorods, (b)-(d) nc-ThO$_2$ samples annealed at different temperatures as indicated in red in the top left corner. Insets are the corresponding FFT images.**

Table 4.6: **Summary of grain size determination to set the Raman calibration curve. The symbol "/" states that no measurements have been performed.**

Heat treatment temperature / K	TEM Mean grain size / nm	XRD Mean grain size / nm
700	4 ± 0.3	4.089
800	6.5 ± 1.25	/
900	9.5 ± 1.44	/
1000	14 ± 6.31	/
1100	20 ± 8.54	/
1400	110 ± 10	/
1600	250 ± 125	/
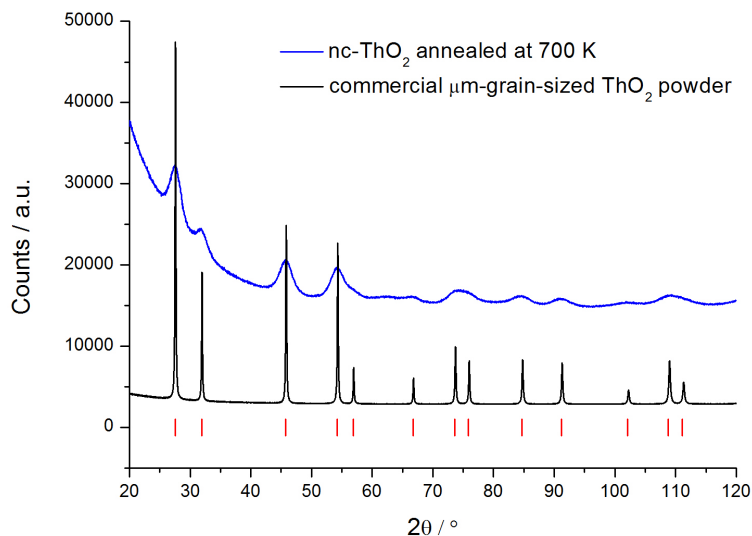
Figure 4.21: XRD diffraction pattern of thoria nanoparticles annealed at 700 K (blue line) compared with the one of μm-sized commercial ThO₂ powder (black line). Also theoretical calculated peaks are indicated with red lines.

after heat treatment. For starting nanoparticles, some more difficulties were encountered. In particular, the T_{2g} peak was often covered by huge fluorescence coming from traces of the ligand, and became detectable only after rising the laser power up to several mW. However, this increasing of laser power affected the peak position and slightly also the FWHM, inducing an error in evaluating grain size with such approach. Instead, Raman spectroscopy performed after heat treatments (when most of the ligand was burnt) showed results in agreement with what was expected.

4.2.3   Laser heating results

A couple of tests were performed on as-synthesised powder samples, but the big amount of ligand burning at high temperature under air hindered the measurements, so that no thermogram could be recorded. Therefore, other samples were heat-treated and the powder was then pressed to obtain pellets as explained in subsection 2.3.2. Table 4.7 shows a summary of the nc-ThO₂ samples analysed in this work.

It is extremely difficult to melt thoria, due to the high melting temperature and its initial transparency to the laser wavelength [26]. Initial experiments were performed with maximum laser power 1000 W, trying to avoid excessive thermal shock on samples, but maximum temperatures were only in the range 3000-3200 K. As a consequence, the laser power was increased up to 1500 W, exceeding the bulk material melting temperature. However, due to high thermal stresses caused in the samples during the laser shot, they often crumbled. The thermogram signal was quite unstable, making it difficult

**Table 4.7: Summary of nc-ThO$_2$ samples analysed in this work.**

Sample	Heat treatment temperature / K
S05	600
S07	700
S08	700
S10	700

to determine a precise value for the melting temperature. All the experiments were performed under air, with a pressure in the autoclave of 3.5 bar. This atmosphere was chosen to avoid reduction of the samples [26]. The calculated NSE value was in good agreement with the one determined in [26], therefore, the value of 0.87 was used in the calculation of sample temperature.

An example of a first thermogram is given in Fig. 4.22. The sample was previously treated in a furnace under air for 1 hour at 600 K. In Fig. 4.22(a), also the thermogram of a μm-grain-sized sample is shown. For this size, freezing occurs at the "bulk" temperature and in this particular case a freezing at 3643 K was measured. The thermogram of nc-ThO$_2$ reveals a lot of differences compared to the μm-sized ThO$_2$ one: first of all, no clear freezing arrest is visible, so melting had to be proved *a posteriori* through SEM images (see next subsection). The irregular shape of the thermogram is due to poor mechanical stability of the pressed powder under the laser power. The pellet had a hole in the middle after the laser shot, thus it was probably melted through the whole thickness. Traces of organic material were still found using Raman spectroscopy and EDX (see next subsection).

Nonetheless, some features can be derived (see Fig. 4.22(b)): at the beginning of the heating stage, a steep change in temperature profile can be ascribed to the overcome of semitransparency already observed for thoria in other research [26]. The signal of the probe laser (RLS) was of a poor quality, still vibrations are present at temperatures much below the melting temperature of bulk material, around 3000-3200 K, as highlighted by the rectangle. The first derivative of the signal is also plotted at the top of Fig. 4.22(b) to better understand the time onset of vibrations linked to the surface tension in the liquid and to the coexistence of solid and liquid phases under the laser spot. Probable formation of liquid material comes at (2833 ± 38) K.

It was not possible to establish in the following experiments the melting onset temperature due to partial destruction of the samples during first stages of heating ramp (see, for example, Fig. 4.23). The destruction of the heated surface affects the thermogram shape which shows artificial variations of the temperature (spikes, see Fig. 4.23). The spikes affect the probe laser signal as well, making the identification of the appearance of the liquid phase impossible. However, even if the onset of vibrations was not clearly detectable, such vibrations were present in the temperature range (2800-3200 K). They did not correspond to surface crumbling, but were formed from vibrating liquid layer.
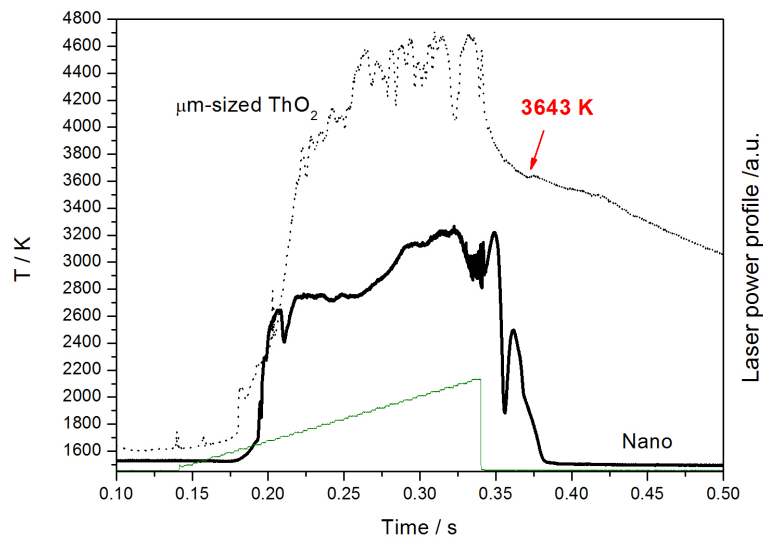
(a)
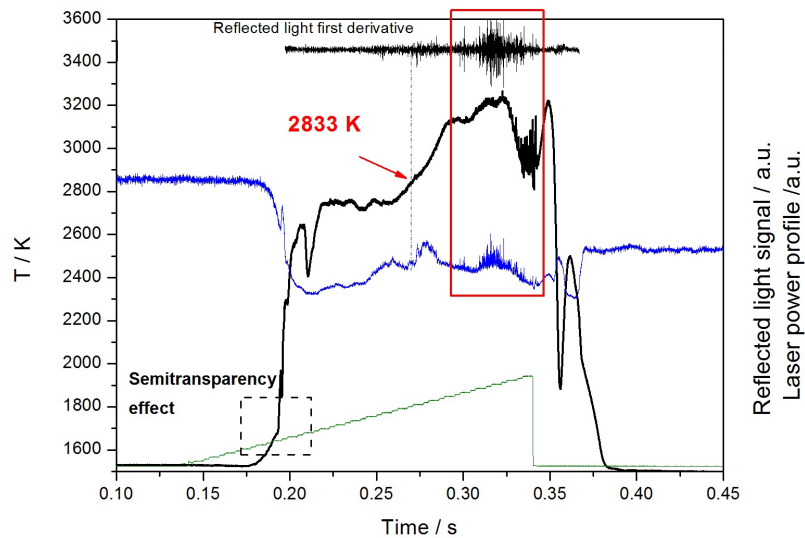
(b)

Figure 4.22: **Laser shot on nanostructured ThO$_2$ pellet heat-treated at 600 K for 1 h under air (S05). (a) Thermogram compared with the one of reference µm-sized pressed thoria powder (solid and dotted black lines, respectively). (b) Thermogram of one sample of nano-thoria. Green line: power profile. Blue line: reflected probe laser signal. Also the first derivative of this signal is plotted at the top of figure.**
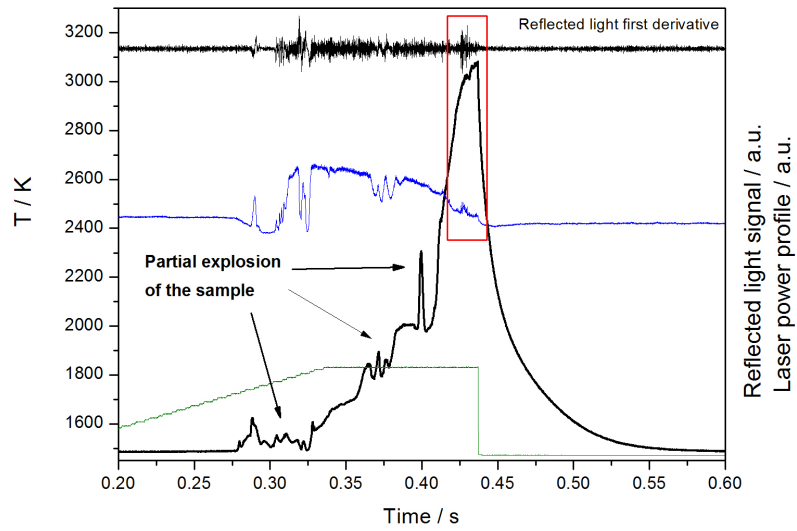
(a)
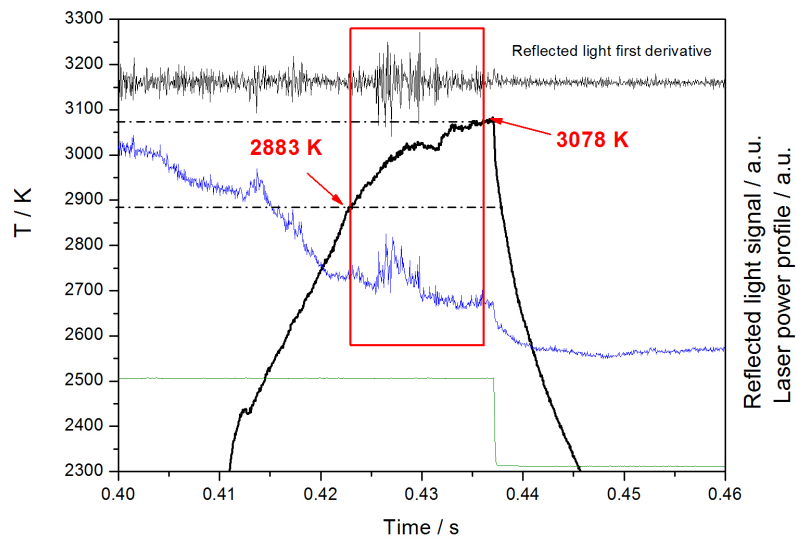
(b)

Figure 4.23: **Laser shot on nanostructured ThO$_2$ pellet heat-treated at 700 K for 1 h under air (S07). (a) Full thermogram recorded. Thermogram shape reflects partial destruction of the sample. Green line: power profile. Blue line: reflected probe laser signal. (b) Magnification of Fig. 4.23(a): these vibrations come from the presence of molten layer in the laser spot.**

4.2.4 Characterization after melting

Characterization after melting experiments was firstly done by Raman spectroscopy and by SEM/EDX and TEM.

The micro-structure of thoria pellets after laser heating experiments was studied by SEM. In Fig. 4.24(a) and Fig. 4.24(b), a general overview and a magnification of the sample heat-treated at 600 K are given. Two main features are present: a base, homogeneous layer characterized by several cracks, probably due to the high temperature gradients during the heating/cooling processes and several agglomerations with mean size of 8.5 µm composed of smaller particles. The base layer displays well defined large grains characteristic of a molten layer, proving that melting was reached. The agglomerated structures on the surface were composed of spherical particles with size ≈ 2 µm surrounded by smaller polyhedral particles. EDX analysis was performed (Table 4.8) to exclude the presence of contamination elements: apart from small traces of impurities in some locations, only oxygen, thorium and carbon were found, the latter due to residual organic ligand. As discussed for UO_2, aerosol particles can vaporise during the experiment and re-deposit on the surface. The spherical particles can be ascribed to quenching of liquid drops, whereas the polyhedral ones to solid particles exploded during the shot and partially agglomerated before recondensing.

(a)   (b)
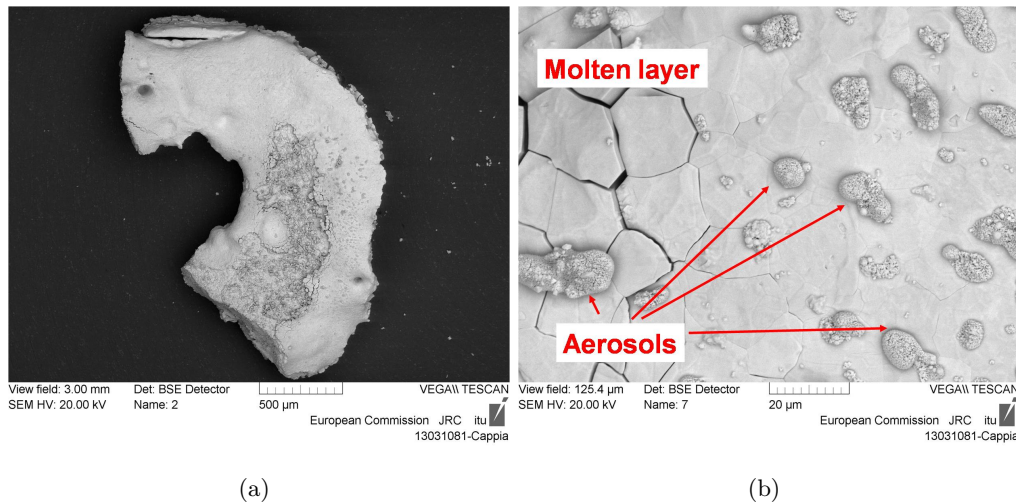
Figure 4.24: (a) BSE image of the molten sample S05. The corresponding thermogram is shown in Fig. 4.22. (b) Magnification of Fig. 4.24(a).
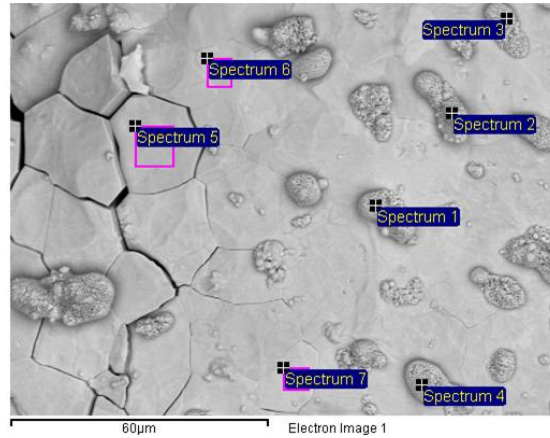
Figure 4.25: EDX spectra of sample S05.

Table 4.8: EDX results of spectra recorded on nc-ThO$_2$ sample (S05).

Spectrum	C	O	Mg[a]	Al[a]	Th	Total[b]
Spectrum 1	10.02	16.48			73.50	100.00
Spectrum 2		15.41			84.59	100.00
Spectrum 3		14.68	0.71		84.60	100.00
Spectrum 4	7.99	9.72		0.75	81.53	100.00
Spectrum 5	9.25	15.61			75.15	100.00
Spectrum 6	10.29	16.35			73.35	100.00
Spectrum 7	9.23	14.87		0.61	75.29	100.00
Max	10.29	16.48	0.71	0.75	84.60	
Min	7.99	9.72	0.71	0.61	73.35	

[a] Contaminations
[b] All results in weight %

In Fig. 4.26, another example is shown: the same molten homogeneous layer is present, with many more aerosol spherical particles deposited at the interface between the molten and unmolten zone (mean size 1.7 µm). This sample was shot using higher power (1500 W instead of 1000 W), reaching 4000 K as maximum temperature, therefore, it is highly probable that more amount of liquid was formed.
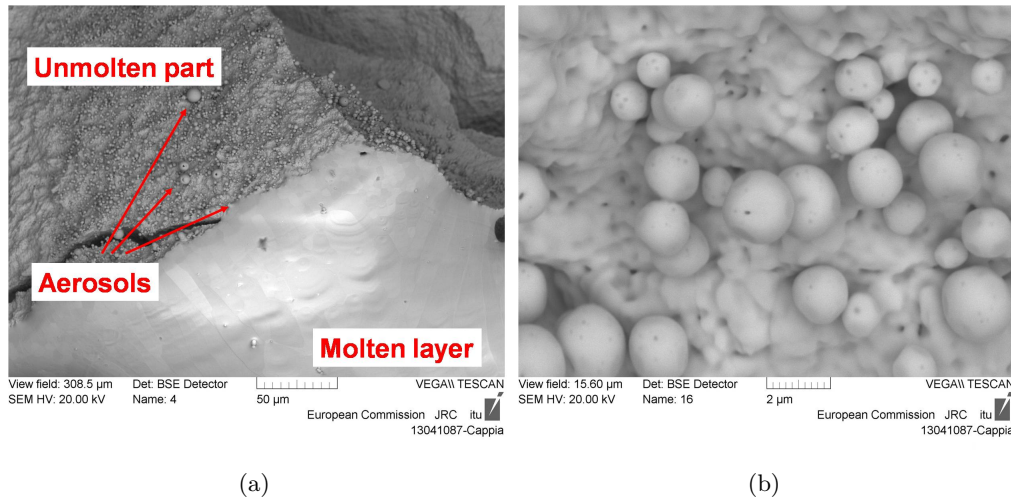
(a)   (b)

Figure 4.26: **(a) BSE image of the molten sample S10 (b) Magnification of aerosols in Fig. 4.26(a).**

Spectra were recorded both after preliminary heat treatments and after laser heating experiments. Estimation of grain size evolution was done using eq. (4.2). An example of the analysis performed on the nc-pellet S05 is reported in Fig. 4.27. As it can be seen, there was a clear variation of grain size after laser heating and melting, where the material was subjected to the highest temperature, although for a fraction of a second only. The current analysis shows that there was a thermal gradient from the periphery to the center of the pellet under the laser shot and only in the melted material a significant grain agglomeration is observed.
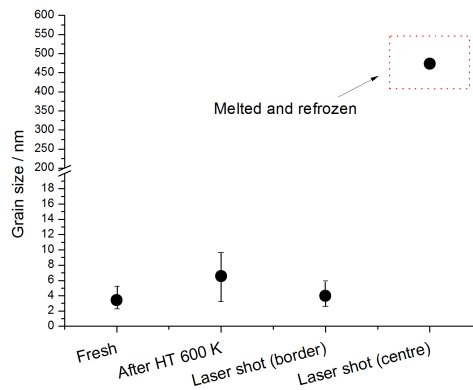

Figure 4.27: **Application of Raman spectroscopy to determine grain size. Fresh = spectrum recorded on material as-synthesised; HT = heat treatment; border and centre = spectra recorded on the periphery and central part of the pellet, respectively. No uncertainty bands could be associated to the melted and refrozen grain size.**

87

Also TEM analysis was performed when possible and in Fig. 4.28 and 4.29 TEM images recorded for the sample S05 are reported. As expected, crystalline domains in the sample were not homogeneous. For example, big agglomerations of hundreds of nanometer (300-500 nm) were observed, with coherent crystalline domains. The corresponding reciprocal lattice image obtained by electron diffraction, in fact, showed bright spots corresponding to ordered structure (Fig. 4.28). Despite this, still smaller domains were observed (Fig.4.29), with size (20 ± 8) nm, as was qualitatively predicted using the empirical approach of Raman spectroscopy (Fig. 4.27).
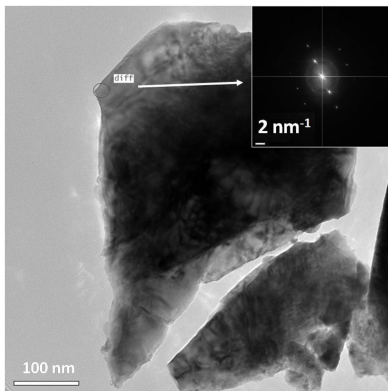

Figure 4.28: TEM image of the sample S05 after melting. The insert picture is the Fast Fourier Transform image of the region indicated in the picture.
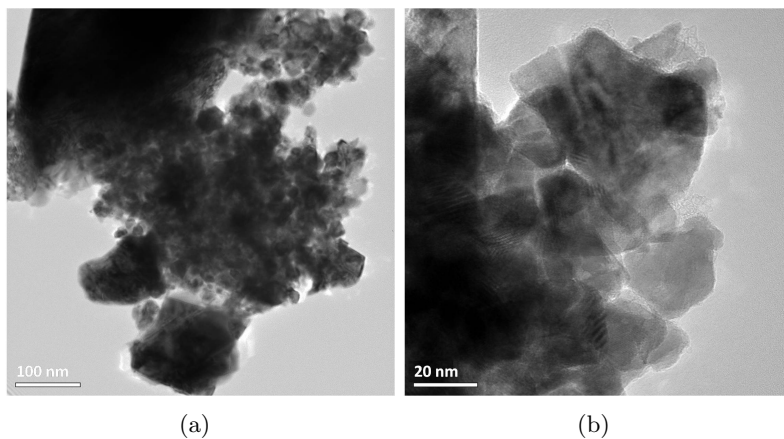

(a)   (b)

Figure 4.29: (a) HRTEM image of sample S05 after melting. (b) Magnification of (a).

4.2.5 Discussion and Conclusions

Although the exact value of the melting temperature for 3-5 nm-sized thoria particles could not be accurately determined, due to experimental challenges already pointed out, it is possible that the melting started around 2830 K. In any case, the presence of liquid was detected using RLS technique in the temperature range 3000-3200 K, much below the melting temperature of µm-sized ThO_2. Melting of samples was confirmed *a posteriori* by analysing SEM images of the sample microstructure. In the case of ThO_2, calculations using Pawlow's model to estimate melting point depression could not be implemented since not all the experimental data needed to use this model are available.

In parallel to this investigation, Raman spectroscopy has been successfully applied as non-destructive, local characterization technique to determine grain particle dimension evolution after laser heating experiments, supported by TEM images.

References

[1] D. Manara, C. Ronchi, M. Sheindlin, M. Lewis, and M. Brykin. *J. Nucl. Mater.*, 342:148, (2005).

[2] P. Buffat and J-P. Borel. *Phys. Rev. A*, 13:2287, (1976).

[3] S.L. Lai, J.Y. Guo, V. Petrova, G. Ramanath, and L.H. Allen. *Phys. Rev. Lett.*, 77:99, (1996).

[4] S.L. Lai, J.R.A. Carlsson, and L.H. Allen. *Appl. Phys. Lett.*, 72:1098, (1998).

[5] M. Zhang, M.Yu. Efremov, F. Schiettekatte, E.A. Olson, A.T. Kwan, S.L. Lai, T. Wisleder, J.E. Greene, and L.H. Allen. *Phys. Rev. B*, 62:10548, (2000).

[6] E. Roduner. *Nanoscopic Materials: Size-dependent Phenomena*. RSC Publishing, (2006).

[7] C. Guéneau, A. Chartier, and L. Van Brutzel. *Comprehensive Nuclear Materials*, volume Volume 2. Elsevier, (2012).

[8] M. Amme, B. Renker, B. Schmid, M.P. Feth, H. Bertagnolli, and W. Döbelin. *J. Nucl. Mat.*, 306:202, (2002).

[9] P.G. Marlow, J.P. Russel, and J.R. Hardy. *Philos. Mag.*, 14:409, (1966).

[10] G. Dolling, R.A. Cowley, and A.D.B. Woods. *Can. J. Phys.*, 43:1397, (1965).

[11] V. G. Keramidas and W. B. White. *J. Chem. Phys.*, 59:1561, (1973).

[12] J. Schoenes. *J. Chem Soc., Faraday Trans.*, 2 (83):1205, (1987).

[13] S. Blumenroeder, H. Brenten, E. Zirngiebl, R. Mock, G. Guentherodt, J.D. Thompson, Z. Fisk, and J. Naegele. *J. Magn. Magn. Mater.*, 76 & 77:331, (1988).

[14] G. Amoretti, A. Blaise, R. Caciuffo, J.M. Fournier, M.T. Hutchings, R. Osborn, and A.D. Taylor. *Phys. Rev. B*, 40:1856, (1989).

[15] R.I. Cooper and B.T.M. Willis. *Acta Cryst. A*, 60:322, (2004).

[16] L. Desgranges, G. Baldinozzi, D. Simeone, and H. E. Fischer. *Inorg. Chem.*, 50:6146, (2011).

[17] L. Desgranges, G. Baldinozzi, P. Simon, G. Guimbretiére, and A. Canizares. *J. Raman Spectrosc.*, 43:455, (2012).

[18] M.L. Palacios and S.H. Taylor. *Appl. Spectrosc.*, 54:1372, (2000).

[19] D. Manara and B. Renker. *J. Nucl. Mat.*, 321:233, (2003).

[20] I.S. Butler, G.C. Allen, and N.A. Tuan. *Appl. Spectrosc.*, 42:901, (1988).

[21] H. He, P. Wang, D.D. Allred, J. Majewski, M.P. Wilkerson, and K.D. Rector. *Anal. Chem.*, 84:10380, (2012).

[22] T. Livneh and E. Sterer. *Phys. Rev. B*, 73:085118, (2006).

[23] S.D. Senanayake, R. Rousseau, D. Colegrave, and H. Idriss. *J. Nucl. Mater.*, 342:179, (2005).

[24] J.L. Bates. *J. Am. Ceram. Soc.*, 49:395, (1966).

[25] J.A. Christensen. Stoichiometry effects in oxide nuclear fuels. Technical report, Battelle Northwest (USA) Laboratory Report 536, 1967.

[26] L. Capriotti and A. Quaini. *High temperature behaviour of nuclear materials by laser heating and fast pyrometry.* Master's thesis, Politecnico di Milano, (2011).

[27] D. Manara. *Melting transition measurements in uranium dioxide.* PhD thesis, University of Warwick, (2004). Technical Note JRC-ITU-TN-2004/05.

[28] F.G. Di Lemma, J.Y. Colle, M. Ernstberger, H. Thiele, and R.J.M. Konings. Internal communication.

[29] J.K. Fink. *J. Nucl. Mater.*, 279:1, (2000).

[30] S. Nichenko. Private communication.

[31] M. Ishigame and M. Kojima. *J. Phys. Soc. Japan*, 41[1]:202, (1976).

[32] D. Hudry, C. Apostolidis, O. Walter, T. Gouder, E. Courtois, C. Kübel, and D. Meyer. *Chem. Eur. J.*, 18:8283, (2012).

[33] D. Hudry, C. Apostolidis, O. Walter, T. Gouder, E. Courtois, C. Kübel, and D. Meyer. *Chem. Eur. J.*, 19:5297, (2013).

Chapter 5

Conclusions and perspectives

The main goal of this thesis has been the investigation of the melting behaviour in nanostructured UO_2 and ThO_2. The interest in these materials is twofold: on one hand, their properties give a deeper insight in the basic thermophysical and thermodynamic properties of nanostructured and, for comparison, bulk actinide oxides. On the other hand, they might be employed in the future as advanced nuclear fuels artificially reproducing in a non-irradiated material the advantageous properties of the high burn-up fuel structure (e.g., high fission gas retention, high resistance to pellet-cladding interaction, without jeopardizing the fuel thermal conductivity).

The synthesis of nanostructured actinide oxides is very recent, so the study of their properties is at its very beginning. No other studies about their melting behaviour have been performed until now. In fact, all conventional techniques usually employed for the study of melting point depression in nano-sized materials are not applicable for refractory oxides, due to their high melting temperatures. In this work, a fast laser heating technique developed at ITU coupled with a fast two-channel optical pyrometer and the RLS method has been applied for the first time to this research domain, for the study of nanocrystalline (nc) UO_2 and ThO_2 pellets. Many difficulties and experimental challenges arose while handling nanostructured actinide oxides, especially under the extreme conditions produced in the current experiments at very high temperatures. The chemical reactivity of actinide oxides was enhanced by the high surface-to-volume ratio typical of nanomaterials. Nonetheless, nanostructured UO_2 and ThO_2 pellets were successfully melted through sub-second laser heating avoiding excessive growth of the grains before melting.

The next sections summarise the main outcomes and the still open questions of the present work. Perspectives and future developments of the study are also given.

Conclusions

In Table 5.1, a summary of the samples analysed in this work is presented.

Concerning nc-UO_2 samples, the accurate initial characterization showed that nano-sized grains are chemically very reactive toward oxygen, even at grain sizes of several

Table 5.1: Summary of the main experimental results.

UO$_2$ [(30± 20) nm]		
Sample	T$_{melting}$ / K	Comments
NCP1	2750 ± 37	
	2813 ± 38	
NCP2	2736 ± 37	
	2845 ± 39	
NCP5	/	
NCP6	2820 ± 38	
ThO$_2$ [3-5 nm]		
Sample	T$_{melting}$ / K	Comments
S05	2833 ± 38	Liquid at 3000-3200 K
S07	/	Liquid at 2880-3100 K
S08	/	RLS vibrations from 3150 K
S10	/	No RLS signal recorded

tens nanometres. The measured melting temperature was between 2730 K and 2850 K as a result of both the size and O/M effects, compared to the melting point of 3120 K established for bulk UO$_2$. However, the present research seems to show that significant deviations from the exact 2.00 stoichiometry play the main role in determining melting point depression of this kind of material for grain sizes of the order of 20 to 50 nm. The enhanced reactivity of the studied material might cause problems in view of their use as potential nuclear fuels. Their chemical stability constitutes therefore a crucial aspect to be taken into account. For example, it might be advisable to increase the grain size up to a level where excessively fast departure from stoichiometry would be avoided. In this case, also the additional melting point depression originating from the small grain size would be reduced. Alternatively, the oxygen potential of a hypothetical nanostructured uranium dioxide-based fuel should be carefully kept under control during operation.

A study of the melting behaviour of nanocrystalline ThO$_2$ was started with the objective of investigating another refractory nuclear oxide with very small grains, but, at the same time, with an increased chemical stability. ThO$_2$ is in fact known to be one of the most stable oxides in nature. This permitted to overcome the issues encountered in handling UO$_2$. The first step in this research was the study of possible maximum melting point depression, so the size of the grains was 3-5 nm in the thorium dioxide samples investigated here. However, because of many experimental difficulties encountered (little amount of material available, fragility of the samples, etc.) it was not possible to determine exact temperature at which this material melted. Nevertheless, a liquid phase was detected at temperatures between 400 K and 600 K below the melting temperature well established for bulk thoria (3651 K), confirming that melting point depression due to grain size effect can be huge also for actinide oxides.

Perspectives

The results obtained in this work open the way to further investigations, the ultimate goal of which can be seen as the assessment of a relationship between the melting temperature and the grain size of nanostructured UO_2 and ThO_2.

Future work on nanostructured UO_2 can be continued in two ways: the first one is the study of new samples with the same grain size of those used in this work (30 nm in average) but not oxidised above O/M = 2.00, in order to compare the results with the ones obtained in this work. On the other hand, the study of nanostructured UO_2 with smaller grain sizes would be fundamental to establish the mentioned relationship between grain size and melting temperature. These new objectives would maybe require to develop a dedicated experimental apparatus fully under inert atmosphere in order to minimise contact with air.

Concerning nanocrystalline ThO_2, instead, much effort should be put in increasing the yield of material production in the synthesis. In this way, it could be possible to obtain more resistant samples to complete the results here obtained for the material with very small grains (3-5 nm). The second step of the study is the production of material with bigger grain size. The possibility to compare the results of ThO_2 and UO_2 with grain size of approximately 30 nm would actually lead to a better understanding of the results obtained here for nanostructured UO_2.

Appendix A

Experimental methods for phase transition temperature measurements

In the first section of this Appendix, a brief explanation of phase rule is given, as it is the fundamental basis behind the experimental method employed for phase transition temperature measurements, which is described after.

A.1   The phase rule

A phase is a homogeneous, physically distinct and mechanically separable portion in a heterogeneous system [1]. The relationship between phases and components of a system, in equilibrium condition, was enunciated by Willard Gibbs (1839 - 1903), and it is known as the Phase Rule. He used the laws of thermodynamics and considered only three independent variables: temperature, pressure and concentration of the components.
The peculiarity of a component is that its concentration can undergo independent variations in the different phases. For example, in the system liquid water-ice, there are two phases (liquid and solid) and only one component, which is water. Oxygen and hydrogen, for example, the chemical elements which form water, are not components, because they are present in the system in a given amount and definite proportion to form water, therefore their concentration cannot be varied independently.

According to Gibbs' phase rule the number of independent variables necessary to fully define the state of the system, called the variance of the system, is given by:

$$\text{F} = \text{C} + 2 - \text{P} \tag{A.1}$$

being C the number of components and P the number of phases inside the system. If one of the intensive variables is fixed (e.g., the pressure), eq. (A.1) becomes

$$\text{F} = \text{C} + 1 - \text{P} \tag{A.2}$$

Generally, systems possessing the same variance will exhibit a similar behavior during phase transitions, no matter how dissimilar the systems may appear. According to the Phase Rule, therefore, it may possible to classify different systems as invariant (F = 0), univariant (F = 1), bivariant (F = 2) and multivariant (F > 2).

A.2   Methods for melting temperature investigation

Both an accurate temperature determination and a thorough characterisation of the sample at the moment of the phase transition are fundamental issues in the experimental determination of a phase diagram.

When the transition is detected with "static" methods, the sample is kept under certain temperature and pressure conditions, then the number of components and phases is measured. This can be done by measurements at temperature (e.g., high temperature X-ray diffraction) or by cooling the system so rapidly as to maintain the phase produced during the transition even at room temperature (quenching).

When the sample temperature is changed and scanned in order to detect the transition, the method is called "dynamic".

A.2.1   Thermal analysis

During the transition two phases coexist, thus P = 2. If a single-component system is considered, then C = 1. Considering a constant pressure situation, from the Phase Rule, an invariant system is obtained, that is F = 0. This means that the temperature must be constant during all the melting/freezing process. Fig. A.1(a) represents a typical solidification arrest of congruent melting materials.

(a)   (b)
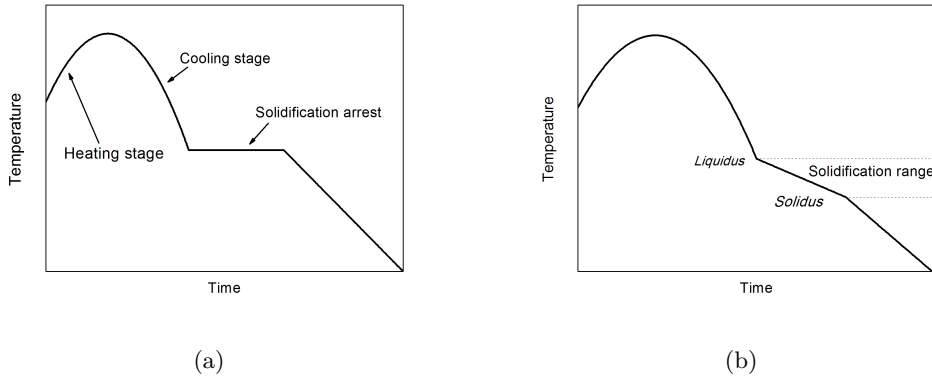
Figure A.1: a) Freezing transition of congruent melting materials. b) Freezing transition of non-congruently melting sample

More complicated is the situation in which more than one component is present inside the system. If C = 2 then F = 1, thus the temperature does not remain constant during the phase transition. In this situation, liquid and solid phases coexist in general with

different compositions, and the phase transition occurs in a temperature range instead of a single temperature (Fig. A.1(b)). During a heating process, the temperature at which the first drop of liquid is formed is called solidus, whereas the temperature at which all the sample is liquid is called liquidus. On a cooling stage the temperature at which the first solid nucleus appears is the liquidus, whilst the solidus is the temperature of complete solidification of the specimen.

One particular category of thermal analysis consists of thermal arrest methods, which are "dynamic" investigation techniques. These experimental methods are based on the detection of the temperature of the phase transition by looking at the change in the cooling/heating rate of the sample due to the release/absorption respectively of the latent heat of transition. Reviews of experimental methods for determining the melting/freezing point of materials are given in [2] and [3].

References

[1] A. Findlay, A.N. Campbell, and N.O. Smith. *The Phase Rule.* Dover Publication INc., 9 edition, (1961).

[2] W.D. Kingery. *Property Measurements at High Temperatures.* John Wiley and Sons Inc. New York Chapman Hall Limited London, (1959).

[3] R.W. Cahn and P. Haasen. *Physical Metallurgy.* Chapman & Hall, (1953).

Appendix B

Nanocalorimetry

The ideal experimental technique for studying the thermodynamics of material systems is *calorimetry* since it allows measurement of heat capacity, phase transition temperature and, therefore, both melting temperature T_m and melting enthalpy ΔH_m. In fact, also the latter has been predicted to be size-dependent in small systems [1].
This Appendix gives a short overview on the differential scanning calorimetry (DSC) technique as well as on the issues concerning its application to the study of thermodynamics of nanoparticles. Finally, a brief description of the new device implemented by Lai et al. [2] and its principle of operation is given.

B.1   Differential scanning calorimetry

Differential Scanning Calorimetry (DSC) is a common technique based on the detection of temperature changes between the sample and a reference crucible upon heating.

The sample and the reference crucible are both heated at a pre-set rate. During a thermal event in the sample, such as a phase transition, the temperature difference between the sample and the reference increases as the reference crucible continues to heat, whereas the sample one is delayed until its full transformation. Hence, a heat flow between the two crucibles is observed and recorded as a peak. The area under the peak is directly proportional to the enthalpy of the transition and its sign indicates if the thermal event is endothermic or exothermic.

Conventional instruments used in DSC cannot be employed for determination of melting points and of latent heats of nanoparticles. In fact, reactions of particles of nanometer dimensions correspond to a few tens of meV (for instance the bulk melting enthalpy of tin amounts to 73 meV per atom [3]) so resolution up to nano-Joule is required.

Resolution depends on the relative heat capacity of the entire calorimetry system. Therefore, by reducing the thermal mass of the system, the resolution can be increased.

Another fundamental problem in calorimetry is related to heat losses during the measurement [4]. To approach near-adiabatic conditions, heating rates faster than cooling rates are required.

The two issues were overcome by Lai et al. through the development of an advanced microcalorimeter [2].

B.2   High-speed microcalorimeter

Lai et al. [2] report a special device where the four components of a calorimetry system (the sample, the sample holder, the heater and the thermometer) were combined into a single multilayer thin film configuration. In Fig. B.1, is reproduced a scheme of the device.
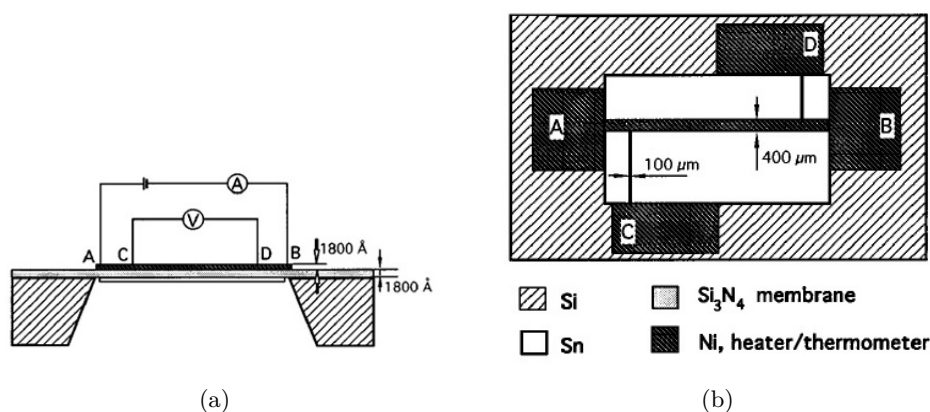

(a)   (b)

Figure B.1: Cross sectional (a) and planar (b) view of microcalorimeter.

The sample holder is a 180 nm Si-N membrane that is supported at the perimeter by a Si substrate. On the support a thin stripe of Ni of the same thickness is deposited and it works both as a resistance heater and a thermometer. The sample (in Fig. B.1 it is a Sn sample) is deposited on the opposite side of the membrane and has approximately the same width as the heater.

Ni heater temperature is raised through Joule effect with a dc current pulse and both voltage and current are monitored in real time. The temperature heating rate reaches 30000 K/s against a cooling rate of about 1000 K/s, so the adiabatic condition is approached. In previous work, the relationship between the resistance $\left(R(t) = \frac{V(t)}{I(t)}\right)$ and the temperature of the heater was determined [5].

The heat capacity of the system is obtained as follows:

$$C_p = \frac{dQ/dt}{dT/dt} = \frac{V(t)\,I(t)}{dT/dt} \tag{B.1}$$

The integral of C_p as a function of temperature gives the enthalpy of fusion.
Using this device a size-dependent drop of ΔH_m in tin nanoparticles was first measured, as in Fig. B.2.
Data were fitted using the LSN model (see eq. (1.4) in Chapter 1) and assuming that the latent heat of fusion per volume of the bulk core is independent of temperature and that

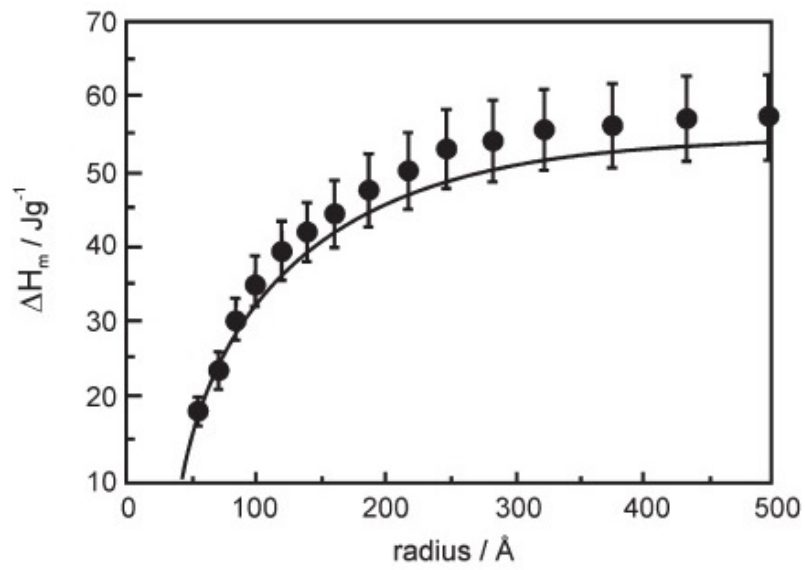solid-liquid interfacial energy and the liquid layer thickness are independent of particle size.

Figure B.2: Size dependence of heat of fusion of Sn atom [6]. The solid line is calculated from the model adopted in [6].

References

[1] F Ercolessi, W. Andreoni, and E. Tosatti. *Phys. Rev. Lett.*, 66:(911), 1991.

[2] S.L. Lai, G. Ramanath, L.H. Allen, P. Infante, and Z. Ma. *Appl. Phys. Lett.*, 67:1229, (1995).

[3] E. Roduner. *Nanoscopic Materials: Size-dependent Phenomena.* RSC Publishing, (2006).

[4] J.M.E. Harper. PhD thesis, Stanford University, (1975).

[5] L.H. Allen, G. Ramanath, S.L. Lai, Z. Ma, S. Lee, D.D.J. Allman, , and K.P. Fuchs. *Appl. Phys. Lett.*, 64:417, (1994).

[6] S.L. Lai, J.Y. Guo, V. Petrova, G. Ramanath, and L.H. Allen. *Phys. Rev. Lett.*, 77:99, (1996).

Appendix C

Phonon confinement model

The Phonon Confinement Model (PCM) was derived by Richter et al. [1] in order to explain the red shift and the broadening of the Raman signal from microcrystalline silicon films.

They start by considering that in an infinite, perfect crystal, the wave function of a phonon with wavevector $\vec{k_0}$ is a plane wave expressed as:

$$\phi(\vec{k_0}, \vec{r}) = u(\vec{k_0}, \vec{r}) \, \exp\left(-i\,\vec{k_0} \cdot \vec{r}\right) \tag{C.1}$$

where $u(\vec{k_0}, \vec{r})$ has the same periodicity of the crystal lattice.

The classical electromagnetic theory of radiations from an oscillating dipole demonstrates that Raman peaks have a Lorentzian shape:

$$I(\omega) = I_0 \times \int_{BZ} \frac{d^3\vec{k}}{\left[\omega - \omega(\vec{k})\right]^2 + \left(\frac{\Gamma_0}{2}\right)^2} \tag{C.2}$$

In eq. (C.2), $\omega(\vec{k})$ represents the dispersion branch which the mode belongs to and Γ_0 is the half-width for the ordered reference structure.

If the particle is assumed to be spherical with diameter D, the propagation of the phonon is restricted to the sphere volume. As a consequence, a localisation of the vibration mode is imposed, through the use of a simple "confinement function".
Thus one can multiply the plane wave by a Gaussian function:

$$\psi(\vec{k_0}, \vec{r}) = \exp\left[-\alpha\left(\frac{r}{D}\right)^2\right] \times u(\vec{k_0}, \vec{r}) \, \exp\left(-i\,\vec{k_0} \cdot \vec{r}\right) \tag{C.3}$$

The new wave function ψ can be expanded in Fourier series [1]:

$$\psi(\vec{k_0}, \vec{r}) = \int C(\vec{k_0}, \vec{k}) \, e^{i\vec{k} \cdot \vec{r}} \, d^3\vec{k} \tag{C.4}$$

where $C(\vec{k_0}, \vec{k})$ are the Fourier coefficients of the series.

Thus, the wave associated with a phonon confined in an imperfect crystal is a superposition of plane waves with $\left|C(\vec{k_0}, \vec{k})\right|^2$ weight.

It can be demonstrated [1, 2] that the power spectral density is affected by the introduction of the terms $\left|C(\vec{k_0}, \vec{k})\right|^2$. The expression of power spectral density in eq. (C.2) becomes [2]:

$$I(\omega) \propto \int_{BZ} e^{-\frac{(\vec{k}-\vec{k_0})^2 D^2}{2\alpha}} \times \frac{d^3\vec{k}}{\left[\omega - \omega(\vec{k})\right]^2 + \left(\frac{\Gamma_0}{2}\right)^2} \tag{C.5}$$

This expresses mathematically the Raman selection rule breaking due to the small size of grains. It is almost exclusively applied to the LO modes [2]. Constant α is set as free confining parameter to fit experimental spectra, once the particle dimension is known. Several authors proposed different values for α: Richter chose $\alpha = 2$ [1], Campbell used $\alpha = 8\pi^2$ [3] as first proposed by Tiong [4].

It should be taken into account that PCM has some limitations: D should not be systematically identified with the grain size. Phonons can indeed be confined by any "spatially limiting" feature in the grain (twins, stacking faults, inclusions, vacancies, boundaries, pores, impurities, etc.). Eq. (C.5) does not take into account particle dishomogenities, therefore, for a more precise evaluation, it should be integrated on particle size distribution. The model relies on a very strong assumption (i.e., material isotropy) and the confining function has no real physical meaning.
Moreover, as it is based on bulky vibrational properties (note that in eq. (C.5) the expression of dispersion curves of bulk material is present), it cannot be applied to particles whose dimension is below 5 nm, limit at which dispersion curves lose their significance according to [5, 6].

Nonetheless, the PCM model is broadly used to explain peaks broadening and shift in experimental spectra [7–9], correlating them to particle dimension [1, 9–12].

References

[1] H. Richter, Z.P. Wang, and L. Ley. *Solid State Comm.*, 39:7625, (1981).

[2] G. Gouadec and P. Colomban. *Progress in Crystal Growth and Characterization of Materials*, 53:1, (2007).

[3] I.H. Campbell and P.M. Fauchet. *Solid State Comm.*, 58:739, (1986).

[4] K.K. Tiong, P.M. Amirtharaj, F.H. Pollak, and D.E. Aspnes. *Appl. Phys. Lett.*, 44:122, (1984).

[5] J. Zuo, C. Xu, Y. Liu, and Y. Quian. *Nanostruct. Mater.*, 10:1331, (1998).

[6] X. Hu and J. Zi. *J. Phys. Cond. Matter*, 14:671, (2002).

[7] Z.V. Popović, Z. Dohčević-Mitrović, M.J. Konstantinović, and M. Šćepanović. *J. Raman Spectrosc.*, 38:750, (2007).

[8] Z.V. Popović, Z. Dohčević-Mitrović, A. Cros, and A. Cantarero. *J. Phys.: Condens. Matter*, 19:496209, (2007).

[9] M. Rajalakshmi, A.K. Arora, S. Dash, and A.K. Tyagi. *J. Nanosci. Nanotech.*, 3:420, (2003).

[10] B. Li, D. Yu, and S.-L. Zhang. *Phys. Rev. B*, 19:1645, (1999).

[11] G.D. Mahan, R. Gupta, Q. Xiong, C.K. Adu, and P.C. Eklund. *Phys. Rev. B*, 68:073402, (2003).

[12] A. Tanaka, S. Onari, and T. Arai. *Phys. Rev. B*, 45:6587, (1992).

Acknowledgments